

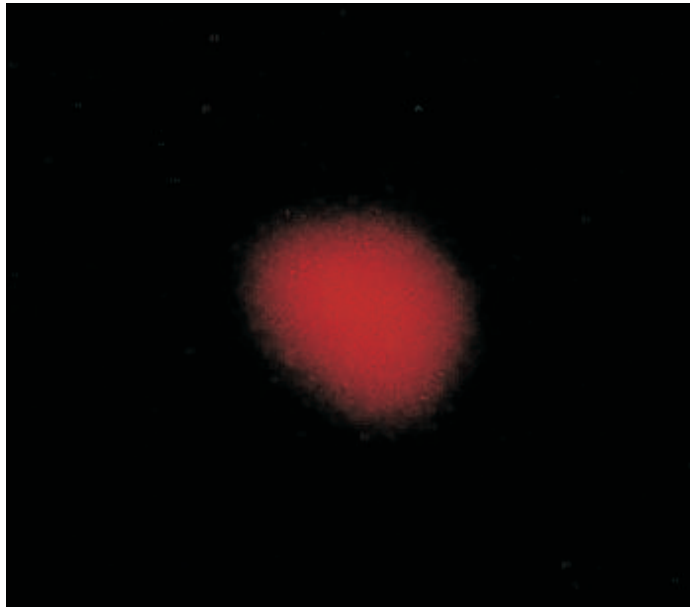
INCREASING THE ATOMIC DENSITY IN A
NEAR RESONANT DARK OPTICAL LATTICE

DISSERTATION
zur Erlangung des Doktorgrades
des Fachbereichs Physik
der Universität Hamburg

vorgelegt von
Vladimir Elman
aus Novosibirsk

Hamburg
2004

Gutachter der Dissertation	Prof. Dr. Andreas Hemmerich Prof. Dr. Werner Neuhauser
Gutachter der Disputation	Prof. Dr. Andreas Hemmerich Prof. Dr. Günter Huber
Datum der Disputation	6. Dezember 2004
Vorsitzender des Prüfungsausschusses	Dr. Klaus Petermann
Dekan des Fachbereichs Physik und	
Vorsitzender des Promotionsausschusses	Prof. Dr. Günter Huber



to my father

Contents

List of Figures	6
List of Tables	9
Summary, Zusammenfassung	11
Introduction	12
1 Laser Cooling Mechanisms	16
1.1 Action of Light on Atoms	16
1.2 Doppler Cooling	17
1.3 Sub-Doppler Cooling	20
1.3.1 Polarization Gradient Cooling: $lin \perp lin$	21
1.3.2 Limits of Sisyphus Cooling	22
1.3.3 Polarization Gradient Cooling: $\sigma_+ - \sigma_-$	24
1.3.4 Sub-Recoil Cooling	25
2 Experimental Apparatus	27
2.1 Vacuum System	27
2.1.1 Oven Chamber	29
2.1.2 Experimental Chamber	30
2.1.3 Liquid Nitrogen Traps	32
2.1.4 Baking Procedure and Leak Tests	33
2.2 Compensation of Stray Magnetic Fields	33
2.3 DAQ System	38
2.3.1 Control System Hardware	38
2.3.2 Control and DAQ Software	39
2.3.3 CCD Camera System	40
3 Laser System	41
3.1 Master Laser	41
3.1.1 Grating Stabilized Diode Laser	42
3.1.2 Pound-Drever-Hall Stabilization	43
3.2 Amplifier (Slave Laser)	47
3.2.1 MOPA Laser Construction	48
3.2.2 MOPA Laser System	49

4	Source of Cold Atoms	52
4.1	Magneto Optical Trap	52
4.2	Capture Range of the MOT	54
4.3	Loading Schemes for MOTs	56
4.4	Our Magneto-Optical Trap	57
4.4.1	Atomic Beam and Beam Deceleration	57
4.4.2	Magnetic Coils	59
4.4.3	Optical Setup for MOT	60
4.4.4	Parameters of the MOT	63
5	2D and 3D Dark Optical Lattices	65
5.1	Conventional (Bright) Optical Lattices	65
5.1.1	One-Dimensional Optical Lattices	65
5.1.2	Multi-Dimensional Optical Lattices	69
5.2	Bichromatic Dark Optical Lattice	70
5.2.1	1D Dark Optical Lattice	70
5.2.2	2D Dark Optical Lattice	75
5.2.3	Light Field Configuration	75
5.2.4	Repumping Laser Field	77
5.2.5	Phase Stabilization	78
5.2.6	Experimental Setup for a 2D Dark Optical Lattice	80
5.2.7	Experimental Time Sequence	82
5.2.8	Spectroscopic Monitoring of OL-Vibrational Spectra	83
5.2.9	Temperature Measurements	88
5.2.10	Evolution of the Atomic Cloud	89
5.3	Extension to the 3D DOL	92
5.3.1	3D DOL Configuration	92
5.3.2	Properties of 3D DOL	93
5.3.3	Temperature Dependence on Lattice Parameters	94
5.3.4	Adiabatic Cooling	97
6	Density Enhancement	99
6.1	Optical Dipole Potential	99
6.2	Standing Wave Red Detuned FORT	102
6.3	Characterization of the FORL	103
6.3.1	Experimental Realization	103
6.3.2	Lifetime Measurements	105
6.3.3	Measurement of the Radial Vibrational Frequency of the FORL	108
6.4	Parametric Density Enhancement	109
A	Notation and Definitions	114
B	Rb Atom Data	115
B.1	Landè factors	117

C Nonlinear Trap Losses	118
D Calculation of the peak-density in the FORL	120
E Materials and Devices	123
E.1 Materials	123
E.2 Devices	124
F Technical Data and Schemes	129
Bibliography	130
Acknowledgement	136

List of Figures

1	A simplified view of an optical lattice	12
2	Vibrational levels in an optical lattice	13
3	Density enhancement procedure in a dark optical lattice	14
1.1	Two-level atom in a laser field	18
1.2	Laser cooling scheme	18
1.3	Principle of Doppler cooling	19
1.4	Level scheme for the $J_g = 1/2 \rightarrow J_e = 3/2$ transition	21
1.5	$lin \perp lin$ configuration	21
1.6	Sisyphus cooling in $lin \perp lin$ configuration.	22
1.7	$\sigma^+ - \sigma^-$ light field configuration.	24
1.8	Level scheme for the $J_g = 1 \rightarrow J_e = 2$ transition	25
2.1	Overview drawing of the vacuum apparatus	28
2.2	Photograph of the UHV system	28
2.3	Photograph of the oven chamber	29
2.4	Photograph of the experimental chamber	31
2.5	A view on the experimental apparatus	34
2.6	Interaction scheme of the $ F_g = 1\rangle \rightarrow F_e = 0\rangle$ transition resonant with two σ_+, σ_- laser fields	35
2.7	Experimental scheme for compensation of stray magnetic fields	37
2.8	Signal from the calibration measurement	37
2.9	Sample of the test measurement of the stray magnetic fields compensation	37
2.10	Scheme of the experimental control system	39
3.1	Principle of grating stabilization	42
3.2	Picture of the diode laser setup	44
3.3	Schema of the mechanical setup of the grating stabilized diode laser system	44
3.4	Schema of the laser frequency stabilization to the atomic resonance	45
3.5	Spectrum of the Rb D2 line	46
3.6	Saturation spectroscopy and error signals used for the laser stabilization	47
3.7	Oscillating behavior of the SDL chip	49
3.8	Experimental setup of our MOPA system	50
3.9	A photography of the slave laser	51
4.1	MOT operation scheme	54

4.2	Energy Levels of ^{85}Rb	55
4.3	Shut-down measurement of the MOT magnetic field	59
4.4	Comparison of linear decaying and Zeeman tailored magnetic fields	60
4.5	Optical scheme of our MOT setup	61
4.6	Detuning scheme for the MOT	62
4.7	Atomic fluorescence in the MOT	63
4.8	Decay measurement of the MOT	64
5.1	Level scheme for the $F = 1/2 \rightarrow F' = 3/2$ transition	66
5.2	$lin \perp lin$ configuration	66
5.3	Harmonic-oscillator model for an optical lattice	68
5.4	Light field topography of 2D optical lattice	69
5.5	Three beams lattice configuration	70
5.6	Sisyphus cooling mechanism in a dark optical molasses	71
5.7	Probe transmission spectrum in a ^{87}Rb 3D dark optical molasses	71
5.8	Raman coupling in the spectroscopy signal from dark optical molasses	72
5.10	Level scheme for the $J = 1 \rightarrow J' = 1$ transition	72
5.9	Ground state energies for different \vec{B}	73
5.11	$lin \perp lin$ standing wave	74
5.12	Light Field Configuration of 2D DOL	75
5.13	Light Field of 2D DOL	76
5.14	Energy levels and transitions in ^{85}Rb	77
5.15	Scheme of the experimental set-up for a 2D dark optical lattice	79
5.16	Scheme for frequency stabilization for DOL lasers	81
5.17	Detuning scheme for the DOL	82
5.18	Experimental sequence of the dark optical lattice	83
5.19	Scheme of the Raman spectroscopy in dark optical molasses	84
5.20	Probe transmission spectra of a 2D dark optical lattice	85
5.21	Vibrational frequency of atoms in the lattice potential as a function of detuning	87
5.22	Evolution of the atomic sample in the 2D dark optical lattice	90
5.23	Size of the atomic cloud trapped in the 2D dark optical lattice as a function of time	90
5.24	Light Field Configuration of 3D DOL	92
5.25	Probe transmission spectra of 2D and 3D DOL	94
5.26	Example of a temperature measurement of the 3D dark optical lattice	95
5.27	Temperature dependence in the 3D dark optical lattice on the magnetic field	96
5.28	Temperature vs. light shift.	97
5.29	Reduction of the lattice light intensity	98
6.1	Level scheme of ^{85}Rb	101
6.2	Three-dimensional view of the standing-wave dipole potential	102
6.3	Scheme of the optical setup for our FORL	104
6.4	Experimental sequence for measurement of the FORL lifetime	105
6.5	Decay of the dipole trap	106
6.6	Fluorescence of the atoms trapped in the FORL	107

6.7	Modulation of the trapping laser intensity for the measurement of the vibrational frequency in the dipole trap	107
6.8	Measuring scheme for the observation of the radial vibration frequency of atoms in the FORL	108
6.9	Results of the measurement of the radial vibrational frequency in the FORL	109
6.10	Configuration of the light fields for the experiment on density enhancement	110
6.11	Scheme for the density enhancement in the FORL	111
6.12	Harmonic oscillation of an atom in the FORL potential	111
6.13	Light modulation of the dark optical lattice for the density enhancement procedure	111
6.14	Measuring scheme for the density enhancement	112
6.15	Experimental results of the density enhancement	113

List of Tables

A.1	Definitions	114
B.1	Physical properties of Rb	115
B.2	Rb isotopes data	116
B.3	Essential laser cooling parameters of ^{85}Rb	116
B.4	Atomic vapor pressure of Rb vs. temperature	117
B.5	Landè g- factors of ^{85}Rb	117
D.1	Essential parameters of standing wave far-off-resonance dipole trap for ^{85}Rb	122
F.1	Thermoelectric voltages for Cu-Konst. thermocoupler	129

Summary

This thesis explores ensembles of ultracold atoms, trapped and cooled in dark optical lattices. In this type of optical lattice, atoms are trapped in quantum states which are decoupled from the trapping light field. Therefore, elastic scattering - the main process limiting the density of atoms in optical lattices - is significantly reduced. This entails the chance to overcome the density limit of 10^{11} at/cm^3 existing in conventional optical lattices. We explore a novel scheme for density enhancement which allows for a four-fold density increase over the initial density of the magneto-optical trap (MOT). We load 10^9 atoms at $70 \mu\text{K}$ from the MOT into a modified optical lattice consisting of a three-dimensional dark optical lattice and a far-detuned optical dipole trap. Atoms are now cooled down to $10 \mu\text{K}$ in the potentials of dark optical lattice at typical densities of $3 \cdot 10^{11} \text{ at/cm}^3$. The enhancement procedure is based on a time sequence composed of cooling and trapping cycles inside the dark optical lattice and cycles of free evolution in an array of microscopic potentials formed by the dipole trap. Applying this sequence to the atomic ensemble, we can reach densities of up to $1.2 \cdot 10^{12} \text{ at/cm}^3$ while maintaining a temperature of $10 \mu\text{K}$.

Zusammenfassung

Im Rahmen dieser Arbeit werden kalte Atome in einem dunklen optischen Gitter untersucht. In diesem Typ von optischem Gitter sind die Atome in Zuständen gefangen, die nur schwach mit dem Lichtfeld wechselwirken. Dadurch ist die elastische Komponente der Photonenstreuung, die in konventionellen optischen Gittern für die Begrenzung der atomaren Dichte verantwortlich ist, erheblich reduziert. Deswegen wird es möglich in dunklen optischen Gittern die Dichtebegrenzung konventioneller optischer Gitter von 10^{11} at/cm^3 zu übertreffen. Wir untersuchen eine neue Methode der Dichteerhöhung, mit der wir einen vierfachen Anstieg der atomaren Dichte gegenüber der Anfangsdichte in der MOT erreichen. Die Atome werden aus einer magneto-optischen Falle, welche einige 10^9 Atome bei einer Temperatur von ca. $70 \mu\text{K}$ fängt, in eine Überlagerung von zwei optischen Fallen geladen. Diese ist durch ein drei-dimensionales dunkles optisches Gitter und eine fernverstimmte optische Stehwellen-Dipolfalle gebildet. Dort werden die Atome auf die Temperatur von $10 \mu\text{K}$ bei einer Dichte von $3 \cdot 10^{11} \text{ at/cm}^3$ gekühlt. Das Verfahren der Dichteerhöhung basiert auf abwechselnden Zyklen der Kühlung und Lokalisierung in dem dunklen optischen Gitter und Zyklen der freier Expansion in den Mikropotentialen der optischen Stehwellen-Dipolfalle. Mit dieser Methode konnte eine Dichte von $1.2 \cdot 10^{12} \text{ at/cm}^3$ bei Aufrechterhaltung der Temperatur von $10 \mu\text{K}$ erreicht werden.

Introduction

The interference pattern of a set of intersecting laser beams creates a stable periodic potential for neutral atoms through the AC Stark shift, which can trap atoms in an ordered, crystal-like structure. A simplified semiclassical view of a one-dimensional (1D) optical lattice formed by a standing wave is shown in Fig 1: atoms are oscillating in the potential minima formed by a light field.

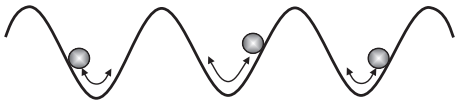


Figure 1: *A simplified view of an optical lattice.*

The idea of light-induced atomic lattices dates back to the late sixties when Vladimir Letokhov proposed the trapping of neutral atoms inside the nodes or antinodes of optical standing waves by means of dipole forces [76]. The experimental realization of such light-induced periodic structures of trapped atoms only became promising after the proposal of Doppler cooling by Hänsch and Schawlow [37] in the late seventies. This proposal raised hopes that atoms could be slowed efficiently and remain captured in the shallow microscopic trapping potentials of optical lattices. However, calculations [30] showed that two-level atoms inside 1D optical standing wave would thermalize at a mean kinetic energy larger than the depth of the trapping potential. The first experimental realization of Doppler cooling in three dimensions was reported in 1985 by the group of Chu [15]. Further investigations [48] showed that temperatures, achieved in such optical molasses, were well below the limit predicted by the theory of Doppler cooling [48]. The explanation of the sub-Doppler temperatures came from the groups of Chu and Cohen-Tannoudji, who proposed one-dimensional semi-classical theoretic models [20, 80] of additional cooling mechanisms arising for multilevel atoms in light fields with spatially varying polarization. The cooling effect arises via spatial correlation between the periodically varying light shift and the optical pumping rate. According to this model, the atomic temperature is directly proportional to the potential depth ($T \sim U$), so that shallow potentials can lead to temperatures two orders of magnitude below the Doppler limit. A refined, fully quantum-mechanical model [12], shows the temperature limit, the so-called recoil-limit (for alkali atoms typically some hundreds of nano Kelvin). At this temperature, the deBroglie wavelength of an atom equals the optical wavelength. As a consequence, the center-of-mass motion needs to be described quantum mechanically, giving rise to quantized vibrational states. At the typical temperatures obtained in optical lattices only the first few of these vibrational levels are populated, see Fig. 2.

An interesting phenomenon arising in optical lattices is the Lamb-Dicke effect [23]. Atoms, that are localized in the optical potential to better than an optical wavelength,

preferentially scatter photons elastically. Therefore, most of the absorption-emission cycles do not transfer momentum to the trapped atoms and thus, leave their motion unchanged. As a consequence, the lifetime of the vibrational levels is much longer than one might expect from the photon scattering rate. This fact allows to spectroscopically resolve the quantized vibrational structure in optical lattices [39, 34]. First and second order sidebands, attributed to Raman transitions between vibrational levels, were demonstrated in transmission [39, 75] and fluorescence [43, 28] spectra.

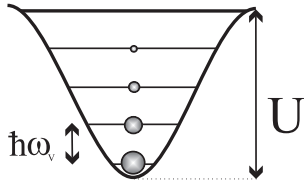


Figure 2: *Position and population of vibrational levels in an optical lattice.*

Atoms in an optical lattice scatter photons at a high rate because they are located around the antinodes of the standing wave, i.e., locations where their interaction with the light field is maximized. These scattered photons act to distort the lattice field and may, thus, degrade the cooling and trapping mechanisms. Therefore, reabsorption of such scattered photons lead to heating and losses. As a consequence, the maximum filling rate obtained with optical lattices is only about 5% of the available potential wells.

A particularly interesting situation in optical lattices is the regime of high densities, when the number of trapped atoms exceeds the number of lattice sites. In this regime, the lattice should acquire some solid-state aspects and quantum statistics should play an important role for the dynamics. One way to prevent extensive spontaneous photon scattering is to detune the laser beams far from atomic resonance. In this case the light field does not provide inherent cooling, i.e., additional cooling is needed [22]. An interesting alternative to significantly reduce the spontaneous scattering, while maintaining a built-in cooling mechanism, is the use of so-called "dark optical lattices" [69, 17]. In contrast to conventional optical lattices, the elastic scattering contribution is entirely suppressed in dark optical lattices. In this new type of optical lattice, the total light field can be decomposed into two polarization components such that the maximum of one component coincides with the minimum of the other. One polarization traps the atoms in its nodes where photon scattering is minimal. The other polarization component although maximal at these locations, only couples to the trapped atoms in the wings of their wavefunctions, i.e., photon scattering by this component is also limited. In this way the overall photon scattering is reduced to those photons needed to maintain a Sisyphus cooling process. Experimentally, dark optical lattices are formed by the interplay between a near-resonant blue-detuned light field and an external homogeneous magnetic field [32, 41]. The reduced fluorescence level in dark optical lattices promises the possibility of higher filling factors as compared to conventional, or bright, optical lattices. Unfortunately, conventional loading of dark optical lattices by a magneto-optical trap (MOT) [59, 1] will only produce densities limited by the MOT physics (on the 10^{11} atoms/cm³ level). Thus, additional schemes are needed which can yield a further density increase.

In this thesis, I explore a dark optical lattice in a novel 3D configuration, providing potential minima, which are singular points in three dimensions in contrast to the earlier implementations of a 3D DOL, where the potential minima formed lines [55, 72], thereby providing efficient escape channels for the trapped atoms. This novel 3D DOL is used to demonstrate a scheme for density enhancement, that has allowed to obtain a four-fold

density increase over the initial MOT-density. This scheme uses a time sequence composed of cooling and trapping cycles in the DOL and cycles of free evolution in an array of quasi-2D microscopic potentials formed by a far-detuned 1D optical standing wave (1D FORT). The low spontaneous scattering rate in a FORT allows to trap atomic samples for seconds and does not limit the atomic density.

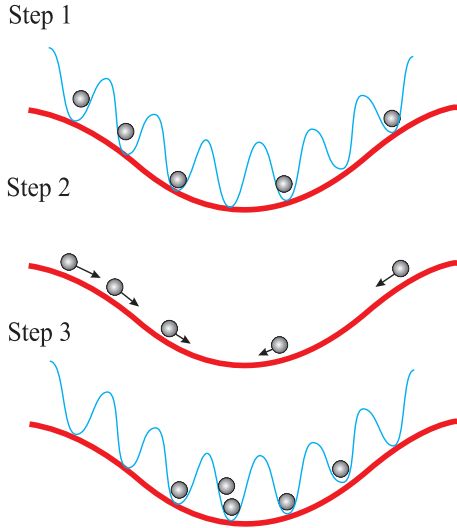


Figure 3: *Density enhancement procedure in a dark optical lattice.*

After repeating the steps 1-3 for 10 ms, we typically achieved a density of $1.2 \cdot 10^{12} \text{ atoms/cm}^3$.

This thesis has the following structure:

Chapter 1 gives a short overview on the cooling mechanisms, which are involved in the production of cold atomic samples inside a magneto-optical trap and optical lattices. Doppler cooling and Sisyphus cooling are briefly described. **Chapter 2** provides a detailed description of the vacuum part of our experimental setup, its technical details and procedures of obtaining proper vacuum conditions. The method of stray magnetic field compensation is described and analyzed. The data acquisition system is explained in detail as well. In **Chapter 3**, the diode laser systems, developed for performing the experiments with Rb-atoms, are introduced. The Pound-Drever-Hall stabilization scheme used to obtain the necessary frequency stabilization of the laser output is described. **Chapter 4** describes the configuration of our magneto-optical trap (MOT), which serves as a prime source of cold atoms for all our experimental investigations. I discuss the loading procedure and specifications of our modified MOT, designed to maximize the density and number of trapped atoms. **Chapter 5** is dedicated to near resonant optical lattices. I give a brief introduction to the physics of "bright" and "dark" optical lattices and explain the novel configuration

The density enhancement procedure, that is explored in this work, can be divided into three steps (see Fig. 3):

Step 1. Atoms are confined in a superposition of the vertically oriented FORT and the 3D dark optical lattice, which cools the trapped atoms to a temperature on the order of $10 \mu K$ (see Fig. 3, Step 1).

Step 2. The dark optical lattice is switched off adiabatically, therefore providing additional cooling of atoms released into the FORT potential. In the horizontal direction the trapping potential of the standing wave is relatively shallow with a corresponding vibrational frequency of $\sim 150 \text{ Hz}$. Thus, atoms are now rolling towards the potential minimum of the FORT and collect there after 1.6 ms for a short time interval (see Fig. 3, Step 2)

Step 3. When the atoms arrive at the potential minimum, the 3D DOL is reactivated in order to freeze

used in our experiments. I present our experimental observations with regard to temperature, density, and spatial diffusion of the trapped atoms. **Chapter 6** begins with a brief summary of physics of far-off resonant optical lattices, concentrating on the parameters: lifetime, temperature, and vibrational frequency of atoms, which are important for our investigations. Finally, the density enhancement scheme is introduced and its efficiency is experimentally demonstrated. We increase the density in dark optical lattice by a factor of four keeping the temperature of trapped atoms on the level of several micro Kelvin, which leads to a four-fold phase-space density enhancement. In conclusion we discuss the limiting factors in our current experimental set-up and possible improvements of our density enhancement scheme. A number of **Appendices** provide a collection of important parameters and their definitions (Appendix A), information on Rb, the atomic species of interest (Appendix B), derivations of important formulas (Appendix C and D), a list of material and devices used to perform the experiments (Appendix E), and a collection of technical data (Appendix F).

Chapter 1

Laser Cooling Mechanisms

1.1 Action of Light on Atoms

The interaction between atoms and light fields relies on the interaction of the induced dipole moment $\vec{\mu}$ and the electric field \vec{E} . Two type of forces arise from this interaction: the dipole force (also called dispersive force, or gradient force) and radiation pressure force (spontaneous force, or dissipative force).

The force due to the radiation pressure can be understood as absorbtion of photons followed by spontaneous emission from the atom. In the case of two-level atom, the theory is simplified. The atom absorbs a photon with momentum $\vec{p} = \hbar\vec{k}$, where \vec{k} is the wavevector ($k = 2\pi/\lambda$) and gets a kick in the direction of the incoming photon (recoil effect). The atom is now excited and next step is the spontaneous emission, which occurs in a random direction by the resonance frequency of the atomic transition. Due to the fact that spontaneous emission is isotropic, the net force acting on an atom in the direction of incoming photons is $\vec{F} = \dot{N}\hbar\vec{k}$, where \dot{N} is the number of scattered photons per time. The number of scattered photons depends on the intensity and detuning of the laser light from resonance and on the natural width of atomic resonance. The radiation force is given by [51]:

$$\vec{F} = -\hbar\vec{k}\frac{\Gamma}{2} \frac{S_o}{1 + S_o + (2(\delta - \vec{k}\vec{v})/\Gamma)^2} \quad (1.1)$$

where Γ is the natural linewidth of the cooling transition, $S_o = I/I_o$ is the resonant saturation parameter (I - laser intensity, I_o - saturation intensity for the transition) and v velocity of the atom. Laser detuning from resonant is $\delta = \omega_L - \omega_A$ with ω_L being laser frequency and ω_A the resonance frequency for atomic transition.

The magnitude of the maximal radiation force , which can act on the atom is given by:

$$|\vec{F}| = -\hbar|\vec{k}|\Gamma/2 \quad (1.2)$$

This force can be used to decelerate an atomic beam. In the case of rubidium (^{85}Rb) at room temperature (T=300K), the average velocity of atoms in the atomic beam is $|\vec{v}| = 296.69$ m/s. The atomic mass of ^{85}Rb is 85 a.m.u., the wavelength of D2 line is $\lambda = 780.027$ nm and the linewidth of transition is $\Gamma/2\pi = 5.98$ MHz. With these parameters, the maximum deceleration of the atom will be $a = \hbar|\vec{k}|\Gamma/2m \approx 1.13 \cdot 10^5$ m/s². As one can see,

this deceleration is approximately ten thousand times bigger than the earth gravitational acceleration. After scattering of $\sim 5 \cdot 10^5$ photons in $t = |\vec{v}|/a = 1.3$ ms, atoms will come to rest passing the distance $L_{min} = |\vec{v}|^2/2a = 78$ cm.

The dipole force is more difficult to understand from the intuitive point of view. One can explain it classically: every atom is polarisable. The electromagnetic field induced the electrical dipole inside the atom, this dipole interact with the electric field. In the homogeneous electric field this will cause the rotation of the dipole, if electric field is inhomogeneous than a force will act on the dipole - dipole force. As the radiation trapping force, the dipole force has resonance behavior, but the dipole force change its sign depending on the detuning: if the field frequency is smaller than the resonance frequency of transition (red detuning) than the force is *attractive*. In the opposite case when the frequency of the light field is larger than resonance frequency (blue detuning), the dipole force is *repulsive*.

One can also understand the dipole force in the analogy to a harmonic oscillator : harmonically bound charge driven by oscillating electrical field oscillate in phase with this field if the exciting frequency is red detuned ($\delta < 0$), or out of phase , shifted 180° , if the exciting frequency is blue detuned ($\delta > 0$). The interaction energy between induced dipole $p = \alpha \cdot E$ and field E is $U = -p \cdot E = \alpha \cdot E^2$, where α is polarizability. Under the resonance this energy is negative and the oscillator will be attracted to the strong field, above the resonance is it positive, so the oscillator will be repulsed and accelerated to the weak field.

In the light field not only a force acts on atoms, but they also subject to light shifts ¹. For a two-level atom in a laser field the light shift is:

$$\Delta = \frac{\hbar\omega_1^2}{4\delta} \quad (1.3)$$

where ω_1 is Rabi frequency:

$$\omega_1 = \Gamma \sqrt{\frac{I}{2I_0}} \quad (1.4)$$

The potential depth experienced, for example, by ^{85}Rb atoms in the laser field of a beam with $220 \mu\text{m}$ and 150 mW power, tuned $\delta = -200$ GHz away from resonance, would be $U_{dip}/k_B = T \approx 129\mu\text{K}$.

1.2 Doppler Cooling

The principle of Doppler cooling mechanism can be nicely illustrated for a two-level atom (see Fig. 1.1) in a weak standing wave with a frequency ω_L , which is slightly red-detuned from the atomic resonance frequency ω_A , $\delta = \omega_L - \omega_A < 0$, see Fig. 1.2.

Each of the two counterpropagating laser beam forming the standing wave exerts an average pressure in the direction of its propagation as the atom absorbs the photons in its propagation direction but emits photons isotropically. When the atom is at rest, the radiation pressure produced by the two counterpropagating waves is exactly balanced, and the total force experienced by the atom, averaged over a wavelength, vanishes. If the atom is

¹also known as AC-Stark shift

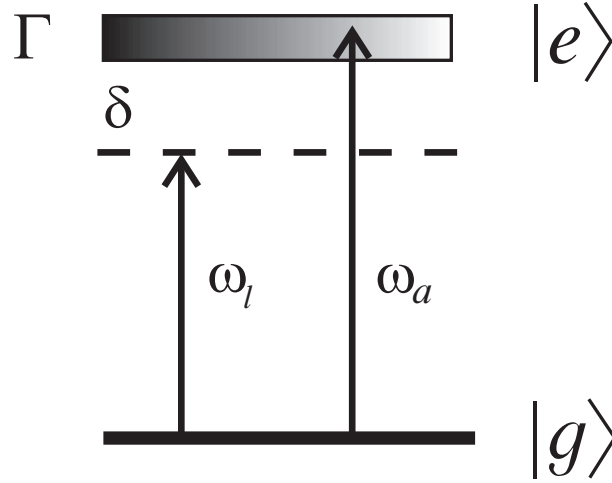


Figure 1.1: Level scheme of two-level atom in a laser field. Laser frequency is detuned from atomic resonance at $\delta = \omega_L - \omega_A < 0$.

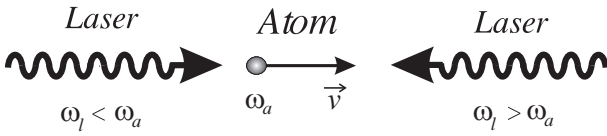


Figure 1.2: An atom moves along the standing wave made of two counterpropagating laser beams, each with the frequency tuned below the atomic resonance frequency by a small amount of $\delta = \omega_L - \omega_A$.

moving along the standing wave at velocity v , the counterpropagating waves have opposite Doppler shifts $\pm\omega_L \cdot v/c = \pm kv$. The frequency of the wave propagating opposite to the atom is tuned into resonance and thus exerts stronger radiation pressure on the atom as compared to the wave copropagating with the atom, which is detuned from resonance. This imbalance between the two radiation pressures gives rise to a net friction force:

$$\vec{F} = \vec{F}_+ + \vec{F}_- = \hbar k \frac{\Gamma}{2} \frac{S_o}{1 + S_o + (2(\delta - \vec{k}\vec{v})/\Gamma)^2} - \hbar k \frac{\Gamma}{2} \frac{S_o}{1 + S_o + (2(\delta + \vec{k}\vec{v})/\Gamma)^2} \quad (1.5)$$

which decelerates the atoms and for small velocities ($kv \ll \Gamma$) and low saturation ($I/I_o \ll 1$) can be written as:

$$F(\vec{v}) = -\alpha \cdot v, \quad \alpha = 4\hbar k^2 S_o \frac{\vec{k}(2\delta/\Gamma)}{(1 + (2\delta/\Gamma)^2)^2} \quad (1.6)$$

where α is the friction coefficient.

Figure 1.3 shows, for low laser intensity, $S_o = 0.625$, the damping force as the sum of two opposing forces that vary with v as Lorentzians, each curve having a width Γ/k . The curves are centered at $\pm kv = \delta$, where $\delta = \omega_L - \omega_A$ is equal to the detuning of the laser from resonance. The slope of the total force at $v = 0$, i.e., the friction coefficient α , is maximum when $\delta \approx -\Gamma/2$: $\alpha = \hbar k^2 S_o$. The total force is then proportional to the laser intensity, always opposes the velocity and is nearly linear in the range $-\Gamma/2 < kv < \Gamma/2$.

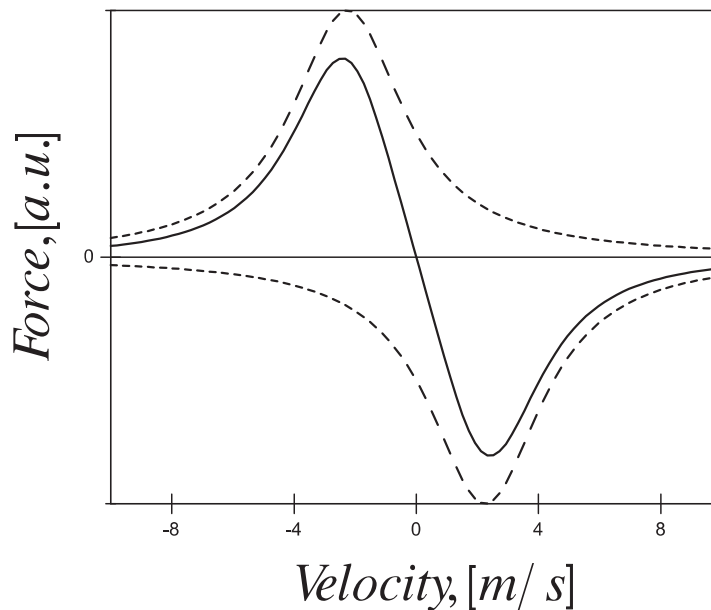


Figure 1.3: *Principle of Doppler cooling: At low intensities, the atom feels average forces in opposite directions from the two beams (dashed curves), with the peaks offset because of the laser detuning. The net force (black curve) is the friction that cools the atom. The slope at $v = 0$ is the friction coefficient. For the curve shown, the detuning is exactly the half of the natural linewidth ($\delta = \Gamma/2$).*

This defines the range of velocities (called the velocity capture range), over which the atomic motion is most efficiently damped by the Doppler force.

The friction force considered above is the mean force, averaged over several fluorescence cycles. The random nature of radiation processes produces fluctuations of the atomic motion, i.e., the force is fluctuating around its average value. These fluctuations heat the atoms via two processes: 1) the number of fluorescence cycles occurring during a given time interval is random (quantum noise) 2) each individual fluorescence photon is emitted in a random direction, giving a random recoil to the atom. Each time an absorption/spontaneous emission cycle occurs, the atom makes two random steps in momentum space. The increase of the mean square momentum is:

$$\frac{d}{dt} \langle p^2 \rangle = 2\Gamma_{scatt} \hbar^2 k^2 = 2D_{spont} \quad (1.7)$$

where Γ_{scatt} is the total photon scattering rate and D_{spont} is the momentum diffusion constant. The diffusion coefficient is defined as the rate of mean square momentum $\langle p^2 \rangle$ increase, which is dependent on the total scattering rate from two laser beams, each of them with intensity I . Assuming $I \ll I_o$ we get

$$2D_{spont} = 2\Gamma \hbar^2 k^2 \frac{S_o}{1 + (2\delta/\Gamma)} \quad (1.8)$$

The factor 2 on the right side of the equation accounts for the two beams. In these considerations we completely neglect interference between the two beams. The mean kinetic

energy increases with the rate:

$$\left\langle \frac{d}{dt} E_{heat} \right\rangle = \frac{d \langle p^2 \rangle}{dt} \frac{1}{2M} = \frac{\hbar^2 k^2}{M} \Gamma \frac{S_o}{1 + (2\delta/\Gamma)} \quad (1.9)$$

where M is the atomic mass. The cooling rate can be expressed through the friction force $F = -\alpha v$ as:

$$\left\langle \frac{d}{dt} E_{cool} \right\rangle = \langle Fv \rangle = -\alpha \langle v^2 \rangle \quad (1.10)$$

For the equilibrium between cooling and heating rate we get:

$$\left\langle \frac{d}{dt} E_{cool} \right\rangle + \left\langle \frac{d}{dt} E_{heat} \right\rangle = -\alpha \langle v^2 \rangle + D_{spont}/M = 0 \quad (1.11)$$

In the one-dimensional case we have only one degree of freedom, so:

$$\frac{1}{2} M \langle v^2 \rangle = \frac{1}{2} k_B T \quad (1.12)$$

And for the steady-state temperature we obtain:

$$k_B T = -\frac{\hbar\Gamma}{4} \cdot \frac{1 + (\delta/\Gamma)^2}{2\delta/\Gamma} = -\frac{\hbar\Gamma}{4} \left(\frac{\Gamma}{2\delta} + \frac{\delta}{2\Gamma} \right) \quad (1.13)$$

This temperature has a minimum at $\delta = \Gamma/2$. This is the minimum temperature (T_D) that can be reached with Doppler cooling:

$$T_D = -\frac{\hbar\Gamma}{2k_B} \quad (1.14)$$

For rubidium, the minimum temperature in this one-dimensional model is approximately $143\mu K$.

A generalization of this 1D example into 3D is accomplished by adding two pairs of beams in the other spatial directions. This configuration has been called "optical molasses"[15]. The configuration of "optical molasses" is not a trap since the damping force is not position depending.

1.3 Sub-Doppler Cooling

Soon after the first demonstration of optical molasses it was observed [48] that the temperature of the atoms was much lower than the temperature predicted by Doppler cooling theory². Obviously, other cooling mechanisms are responsible for the low temperatures observed in "optical molasses". The explanation of sub-Doppler temperatures [20, 80] involves additional features as: optical pumping, light shifts and laser polarization gradients.

In the next two sections we will give a short summary of two basic mechanisms of sub-Doppler cooling, associated with two different types of polarization gradients: $lin \perp lin$ and $\sigma_+ - \sigma_-$ configurations of light field.

²In these experiments [48],[67] was found that the temperatures were around the recoil limit $k_B T_R = \frac{\hbar^2 k^2}{2M}$, two orders of magnitude lower than the Doppler limit $k_B T_D = \hbar\Gamma/2$

1.3.1 Polarization Gradient Cooling: $lin \perp lin$

In this section we consider atomic motion in the field of two counterpropagating plane waves modes with equal amplitudes and orthogonal linear polarizations (see Fig. 1.5) - this light field is called $lin \perp lin$ standing wave

$$\begin{aligned}\vec{E} &= E_0(\vec{e}_x \cos(kz + \omega t) + \vec{e}_y \cos(-kz + \omega t)) \\ &= E_0 \cos(\omega t)((\vec{e}_x + \vec{e}_y) \cos kz + i(\vec{e}_x - \vec{e}_y) \sin kz)\end{aligned}\quad (1.15)$$

The $lin \perp lin$ configuration can be decomposed into two circularly polarized standing waves with opposite helicity shifted with respect to each other by $\lambda/4$. The total polarization of the light field changes when one moves along the z -axis: In $z = 0$ it is clockwise circular (σ_+), in $z = \lambda/8$ it is linear along $\vec{e}_x + \vec{e}_y$, in $z = \lambda/4$ anti-clockwise circular (σ_-), in $z = 3\lambda/8$ linear along $\vec{e}_x - \vec{e}_y$, in $z = \lambda/2$ again clockwise circular (σ_+) (see Fig. 1.5).

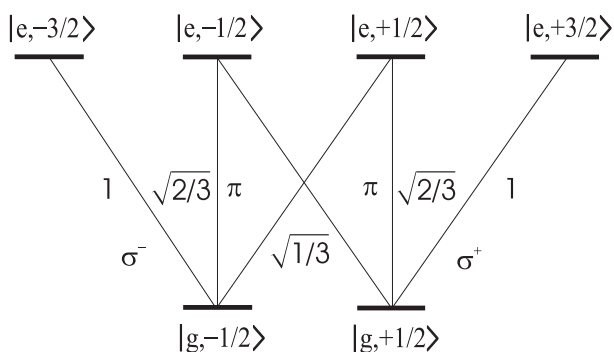


Figure 1.4: Level scheme and Clebsch-Gordan coefficients for the $J_g = 1/2 \rightarrow J_e = 3/2$ transition.

For negative ("red") detuning δ of the light frequency with respect to an atomic resonance, the ground-state energies are decreased by the light shift.

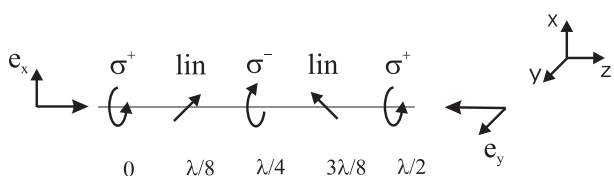


Figure 1.5: $lin \perp lin$ configuration.

Atom at rest. Let us consider the atom placed at a point with pure σ_+ polarization. If the atom is originally in the $g = -1/2$ ground state, excitation and subsequent spontaneous emission can lead back either to $g = +1/2$ or back to $g = -1/2$ state. Once the atom has been transferred to the $g = +1/2$ ground state, further excitation can only reach the $g = +3/2$ excited state from where spontaneous decay always lead back to $g = +1/2$. Thus after a few cycles of excitation and spontaneous decay the entire population is optically pumped to $g = +1/2$. Since the Clebsch-Gordan coefficient for the $g = +1/2 \rightarrow e = +3/2$ transition is by factor $\sqrt{3}$ larger than for $g = -1/2 \rightarrow e = +1/2$ transition, the ground state $g = +1/2$ will experience a larger light shift than the ground state $g = -1/2$. The same happens if the atom is at a location of σ_- polarization. In this case, the atomic population will be transferred to the $g = -1/2$ ground state and the state with $g = -1/2$ experience larger light shift than the state $g = +1/2$.

Moving atom. As the atom moves along the axis of standing wave it will experience a varying polarization, i.e. the two magnetic sublevels $g = -1/2$ and $g = +1/2$ will be shifted in sinusoidal manner along the propagation axes. As the atom moves from a place with pure σ_+ polarization to the one with pure σ_- , the probability of being optically pumped to the $g = -1/2$ increases, and reaches a maximum at the point of pure σ_- polarization. This means that when the atom in the $g = +1/2$ state climbs the potential hill it will be optically pumped into the state $g = -1/2$ close to the top of the potential curve. In the $g = -1/2$ state it will climb a new potential hill and then will be optically pumped into the state $g = +1/2$. The spontaneous photons emitted in this process carries away the potential energy. Such cooling cycles repeatedly occur until the kinetic energy of the atom is not sufficient any longer to climb the potential well and the atom remains trapped. This cooling process has been named Sisyphus cooling because of the similarity of its cyclic mechanism to job of one of the heroes of the ancient Greek mythology.

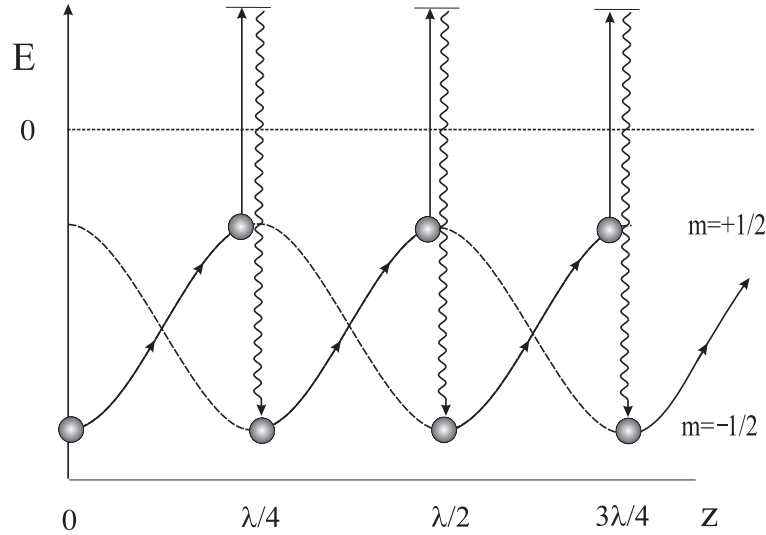


Figure 1.6: The spatial dependence of the light shifts of the ground-state sublevels of the $g = -1/2 \rightarrow e = +1/2$ transition, for the case of the $\text{lin} \perp \text{lin}$ polarization configuration. The arrows show the path followed by atoms being cooled in this arrangement. Atoms starting at $z = 0$ in the $m_g = +1/2$ sublevel must climb the potential hill as they approach the $z = \lambda/4$ point where the light becomes σ^- polarized, and there they are optically pumped to the $m_g = -1/2$ sublevel. They must begin climbing another hill toward the $z = \lambda/2$ point where the light is σ^+ polarized and they are optically pumped back to the $m_g = +1/2$ sublevel. This process repeats until the atomic kinetic energy is too small to climb the next hill. Each optical pumping event results in absorption of light at a lower frequency than emission, thus dissipating energy to the radiation field.

1.3.2 Limits of Sisyphus Cooling

Under assumption of $I \ll I_o$ and $\delta \gg \Gamma$ we can calculate the order of magnitude of the cooling force and the equilibrium temperature in the Sisyphus model. We can examine the decelerating force as a friction force $\vec{F} = -\alpha_{sis}\vec{v}$, which has a maximum when the distance

that an atom moves during a time τ_p is of the order of $\lambda/4$

$$|\vec{v}|\tau_p \approx \lambda/4 \quad (1.16)$$

where τ_p is the optical pumping time. That is fulfilled when

$$k \cdot v \approx \Gamma_p = 1/\tau_p \quad (1.17)$$

For this velocity the energy dissipated during the time τ_z is of the order of $\Delta E = -\hbar \cdot \Delta$ (the maximum energy difference between $g = -1/2$ and $g = +1/2$ states, which is negative because of the detuning $\delta < 0$). The dissipated energy during a time unit is:

$$\frac{dW}{dt} = \frac{\Delta E}{\tau_p} = -\hbar \cdot \Delta \cdot \Gamma_p \quad (1.18)$$

The cooling rate can be also calculated from F , which yields

$$\frac{dW}{dt} = -F \cdot v = \alpha_{sis} \cdot v^2 \quad (1.19)$$

From the above equations we get the expression for friction coefficient α_{sis} :

$$\alpha_{sis} \approx \hbar \cdot k^2 \frac{\Delta}{\Gamma_p} \quad (1.20)$$

The friction coefficient α_{sis} is independent on laser intensity, because the light shift Δ and optical pumping rate Γ_p are both proportional to laser intensity. On the contrary to this the friction coefficient of doppler cooling is proportional to laser intensity (see Eq. 1.6).

For low laser intensities ($\omega_1 \ll \Gamma$) and big laser detuning ($|\delta| \gg \Gamma$) optical pumping time and light shift can be expressed as:

$$\Gamma_p \approx \omega_1^2 \Gamma / 4\delta^2, \Delta \approx \omega_1^2 / 4\delta^2 \quad (1.21)$$

inserting this into Eq. 1.20 we get

$$\alpha_{sis} \approx \hbar k^2 \cdot \delta / \Gamma \quad (1.22)$$

Comparing the Eq. 1.20 with the Eq. 1.6 one can see that the friction coefficient for Sisyphus cooling is larger than the optimum value for the friction coefficient in Doppler cooling achieved at $\delta = \Gamma/2$,

$$\alpha_D \approx \hbar \cdot k^2. \quad (1.23)$$

Note that the velocity range in which this cooling mechanism is working ($kv \approx \Gamma_p$) is much smaller than in the case of Doppler cooling ($kv \approx \Gamma$). In experiments both mechanisms are simultaneously present, so one starts with Doppler cooling and when the atoms are cold enough continues with the sub-Doppler cooling.

Similarly as for Doppler cooling we can calculate a temperature for Sisyphus cooling, assuming that the steady-state can be defined as the equilibrium between diffusion and friction forces,

$$k_B T = \frac{D_{sis}}{\alpha_{sis}} \quad (1.24)$$

where D_{sis} is the momentum diffusion constant. For Sisyphus cooling [20],

$$D_{sis} = \frac{3}{4} \hbar^2 k^2 \frac{\delta^2}{\Gamma} s_o \quad (1.25)$$

with $S_o = \omega_1^2 / 2(\delta^2 + \Gamma^2/4)$ the saturation parameter. Thus we get

$$k_B T \simeq \frac{\hbar \omega_1^2}{8|\delta|} \propto \frac{I}{\delta} \quad (1.26)$$

From this expression one could conclude that since decreasing the intensity and increasing the detuning decreases the temperature, an arbitrarily low temperature value can be obtained. However, there exists a lower limit for the cooling process: if we lower the intensity, at some point the energy lost in each cooling cycle ΔE will be of the same order as the recoil energy gained from spontaneous emission. Thus, further lowering of the intensity degrades the cooling efficiency and the steady-state temperature will rise again.

1.3.3 Polarization Gradient Cooling: $\sigma_+ - \sigma_-$

Consider an atom on a $J = 1 \rightarrow J = 2$ transition³ (see Fig. 1.8) interacting with a stationary waves obtained from two plane waves counterpropagating along the axis z . These waves have the same frequency ω_L , the same intensity and opposite circular polarizations: σ^+ and σ^-

$$\begin{aligned} \vec{E} &= E_0(\vec{e}_+ \cos(kz + \omega t) + \vec{e}_- \cos(-kz + \omega t)) \\ &= -i\sqrt{2}E_0 \cos(\omega t)(\vec{e}_x \sin kz + \vec{e}_y \cos kz) \\ &\equiv -i\sqrt{2}E_0 \cos(\omega t)\vec{e}_Y(z) \end{aligned} \quad (1.27)$$

where $\vec{e}_\pm = \mp 1/\sqrt{2}(\vec{e}_x \mp i\vec{e}_y)$. The two orthogonally polarized waves cannot interfere (in the usual meaning), so the intensity does not depend on the position. The polarization of the laser field is always linear along \vec{e}_Y and rotating in the $x-y$ plane as one moves along the z -axis. In this case, the light shifts of the ground state sublevels remain constant when the

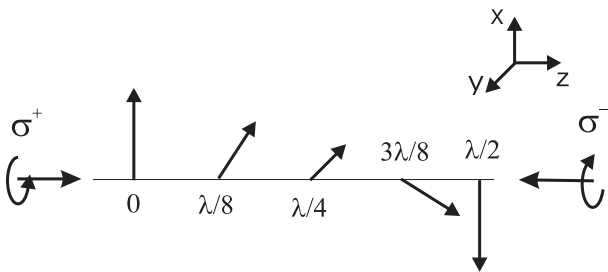


Figure 1.7: $\sigma^+ - \sigma^-$ light field configuration.

atom moves along the z -axis and there is no possibility of a Sisyphus effect. Only the orientation phenomena are important for the cooling mechanism in this polarization configuration.

Consider an atom at rest, in the case of red-detuned laser ($\delta < 0$), the three ground state Zeeman sublevels have different populations and are differently light shifted: $|g, +1\rangle$ and $|g, -1\rangle$ have each a steady-state population of $4/17$ and a light shift $\Delta'_{\pm 1}$ while $|g, 0\rangle$ has a population of $9/17$ and a

³This cooling mechanism works on every $J \rightarrow J + 1$ transition

light shift of $\Delta'_0 = 4/3 \Delta'_{\pm 1}$. An atom moving along the z -axis with velocity v sees a linear polarization along \vec{e}_Y rotating around the z -axis in the $x - y$ -plane with a frequency $-kv$. In a co-moving and rotating coordinate system, the atom is at rest and the polarization direction is fixed. This frame change introduces in the Hamiltonian an internal term $H_{rot} = kvJ_z$ described by a fictitious homogeneous magnetic field in the z direction. If the atomic velocity is small, the effect of this magnetic field can be treated as a perturbation: the new eigenstates are linear superpositions of the three Zeeman sublevels. For an atom moving toward $z > 0$, a population difference between the $|g, -1\rangle$ and $|g, +1\rangle$ states arises:

$$\Pi_{+1} - \Pi_{-1} \propto kv/\Delta'_{\pm 1} \quad (1.28)$$

Since there is a six times greater probability that an atom in $|g, -1\rangle$ will absorb a σ^- photon propagating toward $z < 0$ than that it will absorb a σ^+ photon propagating toward $z > 0$, it follows that the radiation pressures exerted by the σ^+ and σ^- waves will be unbalanced. The atom will scatter more counterpropagating σ^+ photons and its velocity will decrease. For slowly moving atom the friction coefficient can be calculated to give [20]

$$\alpha_\sigma = \hbar k^2 \frac{\Gamma}{\delta} \quad (1.29)$$

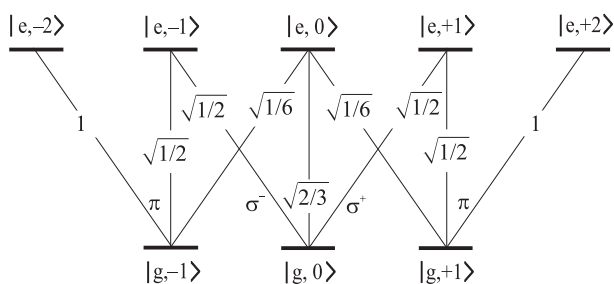


Figure 1.8: Level scheme and Clebsch-Gordan coefficients for the $J_g = 1 \rightarrow J_e = 2$ transition.

as in the $lin \perp lin$ set-up, it does not depend on the laser intensity I . Comparing α_σ with 1.20, we see that α_σ is much smaller as we assume $\Gamma \ll |\Delta|$. A detailed calculation [20] taking into account heating processes shows however, that a steady-state temperature of the same order and below the Doppler limit can be reached in both cooling schemes, since the diffusion coefficient for the $\sigma^+ - \sigma^-$ set-up is much smaller than the corresponding one for $lin \perp lin$.

1.3.4 Sub-Recoil Cooling

In the standard Sisyphus cooling mechanisms the atoms are cooled down and localized at sites where their interaction with the laser field is maximum. This situation affects the minimum steady-state temperature because the momentum distribution width is determined by a dynamical equilibrium between the dissipation mechanism and the heating induced by photon scattering [20]. In order to overcome this limitation, some extensions of the Sisyphus mechanism have been proposed [10] that work on a $J \rightarrow J' = J$ or $J \rightarrow J' = J - 1$ transition with blue detuning ($\delta > 0$). In these situations the atoms are accumulated in states that have a minimum photon-scattering rate (dark optical molasses). Polarization-gradient cooling is based on spontaneous processes: a friction force is always associated with inelastic photon scattering. Therefore, the steady-state momentum distribution cannot become narrower than the recoil momentum $\hbar k$. A completely different laser-cooling mechanism is able to break down this limitation: velocity-selective coherent population

trapping (VSCPT) [6]. This cooling method is based on a quantum interference mechanism that creates an atomic state not coupled to the laser field. The atoms are trapped in this state which has a zero average momentum and can therefore be cooled down to very low temperatures ($T_{rec}/8$ for He atoms [81]). This mechanism cannot be interpreted in terms of a friction force: the cooling is obtained through a diffusion process in momentum space combined with selectively pumping slow atoms into an internal state which no longer interacts with the light field.

Chapter 2

Experimental Apparatus

The lifetime of an atom in a certain state of internal and kinetic energy strongly depends on the collision rate with other atoms of the same sort and on the collision rate with atoms of all other elements present in the experimental apparatus (background collisions). The main goal of the vacuum system is to provide a suitable gas environment, where the background collisions do not limit the observation time of the physical effects of interest. At a typical background pressure (mostly due to N_2) of $p=10^{-9}$ mbar in the vacuum chamber at room temperature, the mean free path of an N_2 molecule will be

$$\lambda = \frac{1}{n\sigma\sqrt{2}} = \frac{k_B T}{p\sigma\sqrt{2}} = 2173,19 \text{ m} , \quad (2.1)$$

where k_B is the Boltzmann constant, T is the temperature, n is the atomic density, and $\sigma \approx 10^{-17} \text{ m}^2$ is the collisional cross section. The average velocity of an atom is given by [60]

$$\bar{v} = 1,13 \sqrt{\frac{2kT}{M}} , \quad (2.2)$$

with M being the atomic mass. For nitrogen, the time between collisions is $\approx 3 \text{ s}$, which is long enough to perform the measurements. In the following section the vacuum system of our experimental apparatus is described in detail.

This chapter describes the vacuum system, the control and acquisition systems, and the procedure for compensation of stray magnetic fields.

2.1 Vacuum System

The ultrahigh vacuum (UHV) system consists of two parts: The oven chamber and the experimental chamber, see Fig. 2.1.

The atomic beam is formed inside the oven chamber. Rubidium is heated in the oven to a sufficiently high temperature in order to evaporate the atoms. The increased partial pressure of Rb drives the atoms through small channels of the collimator towards the experimental chamber. After the collimator, atoms can be divided into two groups. The first one consists of the atoms that passed the collimator channels ballistically, i.e., without collisions with the collimator walls. These atoms provide a collimated atomic beam. The

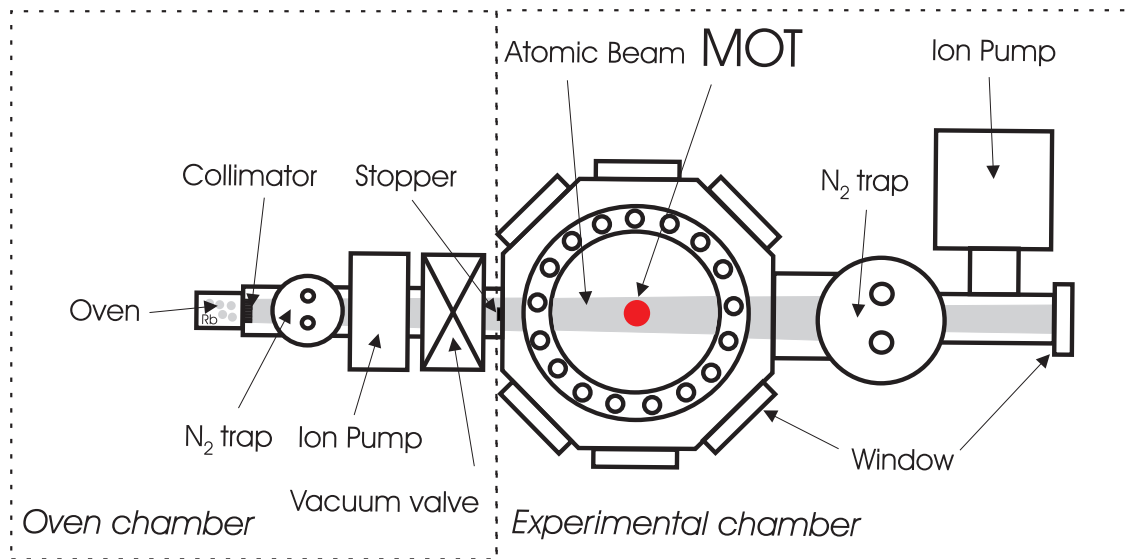


Figure 2.1: An overview drawing of the vacuum apparatus. All important elements are schematically shown. For more details see photo in Fig. 2.2.

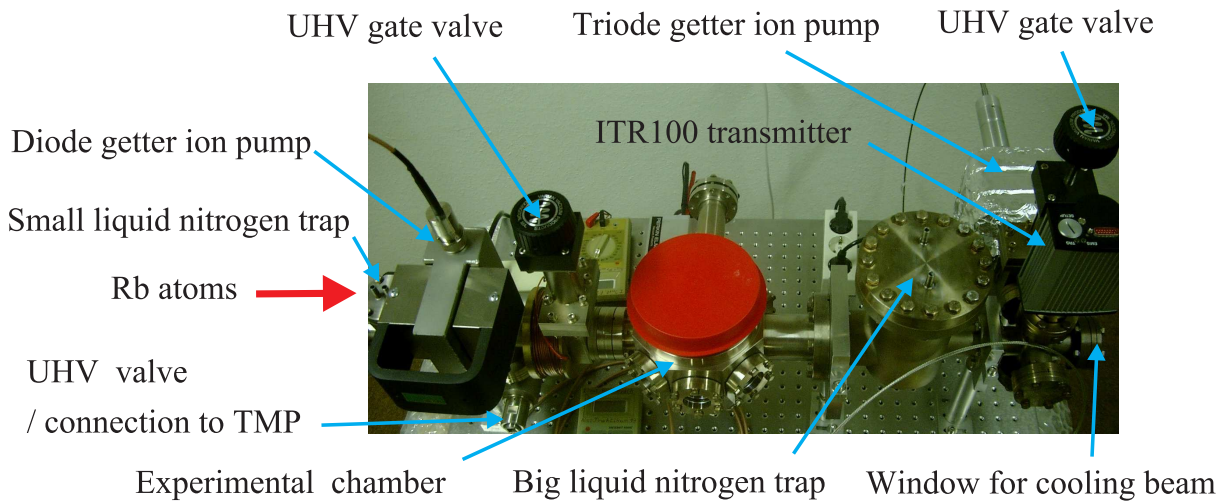


Figure 2.2: Photograph of the UHV system. The oven chamber is not shown, for details of this part of the apparatus see Fig. 2.3. The red plastic cap on the upper window of the experimental chamber is for protection during transportation.

second group is formed from the atoms that collided with the collimator walls and, thus, pass the collimator diffusively. These atoms produce a background vapor, that increases the vacuum pressure inside the experimental chamber and, therefore, has to be separated from the atomic beam.

Leaving the collimator, atoms pass through a liquid nitrogen trap, which separates the background vapor from the collimated atomic beam. Then the collimated atomic beam enters the experimental chamber, where the measurements are performed. Finally, the atomic beam is directed into an ion pump, which maintains a constant pressure in the chamber. To avoid the production of Rb vapor in the experimental chamber when the experiment is not active and to maintain UHV vacuum conditions in the experimental chamber during replacement of the Rb ampoule, a UHV valve is placed between the oven and the experimental chamber of the vacuum system. All important parts of our vacuum system are shown in Fig. 2.2.

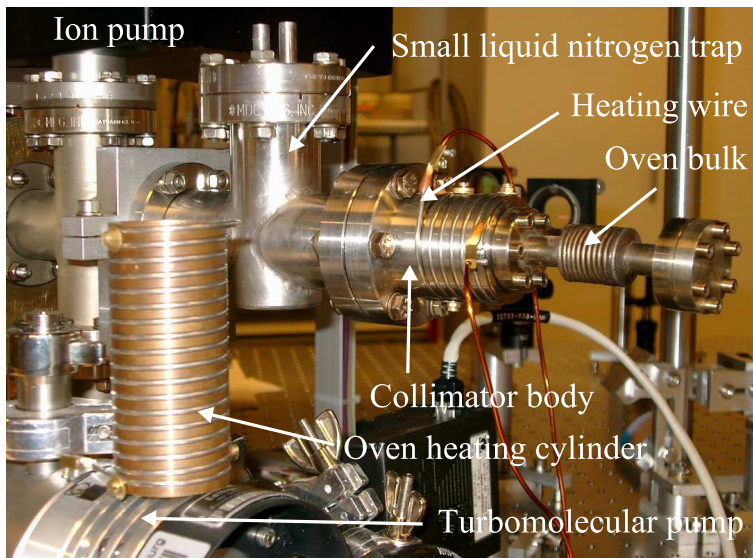


Figure 2.3: Photograph of the oven chamber. The heating cylinder for the oven bulk is removed in order to obtain a view on the heating bulk. The Rb ampoule is loaded into the oven bulk after removing the blank flange. An UHV valve for the connection with turbo molecular pump is shown in Fig. 2.2. The collimator stack is mounted inside the collimator body next to the connection with the oven.

The pressure is measured with an ITR100 vacuum gauge (Bayard-Alpert ionization vacuum gauge, for technical details see AppendixE.2).

Two getter ion pumps maintain the UHV conditions inside the vacuum system. The first one is a diode ion pump (Perkin Elmer PE 11 STD with 11 l/s pumping speed, see Appendix E.2) and is connected to the oven chamber. The second pump is a triode ion pump, which pumps rare gases and has better pumping characteristic for nitrogen. This pump (Varian Star Cell VacIon Plus 20 with 20 l/s, see Appendix E.2) is directly connected to the main experimental chamber. These vacuum pumps maintain a pressure down to 10^{-10} mbar without atomic beam. When the atomic beam is switched on, the pressure in the vacuum system grows up to 10^{-8} mbar. The pressure is measured with an ITR100 vacuum gauge (Bayard-Alpert ionization vacuum gauge, for technical details see AppendixE.2).

2.1.1 Oven Chamber

In this paragraph the construction of our Rb oven and the beam collimation are explained. A view of the relevant section of the apparatus is given in Fig. 2.3. The source of rubidium

is a commercial glass ampoule containing 1g of Rb in its natural isotopes mixture¹. This ampoule is located in a bellow tube welded on both sides to DN 16CF flanges. One side of the bellow is connected to the vacuum chamber, the other one is sealed with a blank DN 16CF flange. The collimator consists of a stack of 4 stainless steel plates, which is fixed inside the vacuum chamber through aluminium ring gasket with 4 screws. Each of the collimator plates is 6mm thick and has 324 holes of 0.8 mm diameter. Four such plates are combined to a stack and arranged such that all collimation channels are open all over the stack length. This position is fixed with tacks to avoid misalignment. The total length of the stack is 24 mm, thus, providing the atomic beam with a collimation ratio of 30. Originally, instead of this stack, we installed a microchannel plate (MCP), see E.1, but after a while, this MCP was destroyed by Rb, presumably because the ceramics of this MCP reacts with Rb. To avoid this unwanted chemical reaction one could protect the MCP with a Cr coating, which is stable in a Rb environment.

Heating of the collimator is provided by 5 turns of a special heating² wire, which is wound inside grooves cut into the walls of the vacuum chamber in the vicinity of the collimator. For heating, the oven is covered by a copper cylinder. In the cylinder, a groove with 12 turns is cut to receive the heating wire. The special heating wire we use, consists of a central nickel-chromium wire embedded in isolating mineral powder, surrounded by a flexible and weldable cladding. Therefore, the heater is electrically isolated from the chamber. Temperatures of the oven and the collimator are observed with thermocouples³ that are attached to the oven heating cylinder and the collimator body. The temperature of the collimator stack should always be higher than that of the Rb oven, otherwise, condensed rubidium could collect in the collimator channels and would disturb the atomic beam production. Typical temperatures in our experiment are: 150°C for the collimator and 130°C for the oven. Because of the high vapor pressure of Rb (see table B.4) these moderate temperatures are sufficient to produce an atomic beam with a density of $3 \cdot 10^9 \text{ atoms/s}$ in the MOT region.

Rubidium is loaded in the oven through an open flange on the bellow tube. The Rb ampoule was cut on the air with a glass-cutter and pushed into the bellow tube. After pumping out the oven part (to about 10^{-6} mbar) with mechanical backing and turbomolecular pumps, the ampoule was broken by bending the bellow tube. After baking the oven chamber for a couple of hours, the experiment can be run. During the baking procedure, both UHV (ion and turbomolecular) pumps are turned on. By heating a new Rb charge, a typical atomic beam is established with a time delay of ≈ 15 min in comparison to the usual situation (with an old, used Rb charge). This time is required for the Rb atoms to get out of the ampoule and spread all over the oven reservoir.

2.1.2 Experimental Chamber

The experimental chamber is the main part of our vacuum system and is shown in Fig. 2.4. It is shaped as an octagon with two DN 100CF flanges placed on the upper and bottom

¹Rubidium ampoule 99,5% (*m.b.*), for detail see E.1

²Thermocoax 1NcAc20, for detail see E.1

³Copper-Konstantan contacts. The temperature range is -100 to +500°C with the tolerance of 2.5°C, the calibration table is shown in the F.1

sides. On vertical sides it has five specially prepared "flanges" to mount the windows. Two DN 40CF and one DN 63CF rotating flange on extending tubes serve for connection to the oven chamber, the liquid N_2 trap, and to mount the tilted window.

The vacuum chamber material was chosen to minimize stray magnetic fields. For the experimental chamber we use AISI 316LN (DIN 1.4429) stainless steel with the magnetizability $\mu = 1.001$, for the other parts of our vacuum chamber we take AISI 304 (DIN 1.4401) or AISI 304L (DIN 1.4301) stainless steel with $\mu = 1.03$. To reduce the influence of stray magnetic fields on the experimental conditions we use the optical table made of non-magnetic stainless steel E.2.

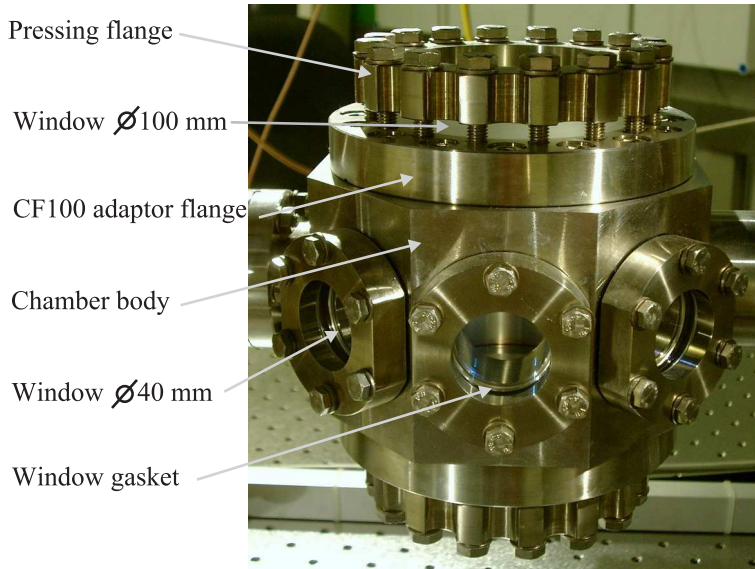


Figure 2.4: View of the experimental chamber.

Commercially available viewports are easy to mount to a vacuum chamber (usually through a CF flange), but optical quality of these viewports is not sufficient for the experiments with high requirements on the light beams. The uneven surfaces and bulk material impurities of these viewports distort the wavefronts of the laser beams and cause interference patterns, making them unsuitable for experiments with optical lattices. That is the reason why we decide to built our chamber using quartz substrates with high optical quality⁴. The price we have to pay for it are the difficulties in construction for connecting the windows to the UHV chamber. All windows are connected to the experimental chamber through special gaskets⁵. These gaskets are toroidal aluminium rings cut on the outer surface and have an inner Nimonic spring that presses the softer shell of the aluminium toroid onto two contacting surfaces (the quartz window on the one side, the stainless steel vacuum chamber on the other), therefore, establishing the vacuum seal. Special preparation of contacting surfaces is required to maintain UHV conditions in the chamber. The metal surface of the vacuum chamber must be machined on a lathe to avoid microgrooves crossing the gasket's contact line which could be created by polishing the contact surface with a polishing wheel. The AR-coatings on the windows must be smaller than the area of the inner circle of the gasket - we have observed that if a coating is made on the contact area of a gasket it can be damaged due to the high local pressure under the gasket, and vacuum leaks might occur. To avoid damage of the windows by applying pressure to seal

⁴All windows attached to the experimental chamber are made of fused silica. Two windows with $\varnothing = 100\text{ mm}$, $\delta = 15\text{ mm}$, five windows with $\varnothing = 40\text{ mm}$, $\delta = 10\text{ mm}$, one window with $\varnothing = 60\text{ mm}$, $\delta = 10\text{ mm}$. All windows are polished to $\lambda/10$, $S/D : 20/10$ quality and AR-coated for $\lambda = 780\text{ nm}$ on both sides.

⁵Helicoflex[®], type HN100, aluminium/Nimonic 90

the connection, we placed Helicoflex[©] gaskets on both sides of a window. By mounting this construction one must use gaskets of equal diameter and make sure that they are positioned exactly coaxial to each other. Moreover, it turns out that this type of gaskets is useful only with windows whose diameter is larger than 60 mm⁶, since at smaller viewport dimensions, a standard number of compressing screws cannot provide enough pressure to avoid leaks after the bake-out procedure.

Five windows of 40 mm diameter are directly connected to the vacuum chamber through Helicoflex[©] gaskets, two 100 mm windows on the upper and lower sides of the chamber are first connected to the adaptor flange (DN 100CF to Helicoflex[©]) and then mounted through DN 100CF flange to the experimental chamber as shown in Fig. 2.4. This allows one to change the design of experimental chamber easily, if necessary.

2.1.3 Liquid Nitrogen Traps

We equipped our apparatus with two liquid nitrogen traps (N_2 traps). The first one is positioned just after the oven. The purpose of this trap is to collect the vapor part of the atomic beam leaving the collimator. We choose a compact design for this trap in order to keep the distance between the oven and the MOT region as short as possible (the shorter this distance, the bigger the brightness of the atomic beam). The trap consists of a trap body and a container for liquid nitrogen. The trap body is designed as a tube closed on one end and having a DN 40CF flange for connection with the container on the other. Two oppositely positioned DN 40CF flanges for connection with other vacuum chamber elements are welded to the trap body not far from the closed end of the tube perpendicular to its axis. The container for liquid nitrogen is made also in tube geometry. It is closed on both ends and is welded with two small tubes to the blank DN 40CF flange. The two tubes allow to fill the tank with liquid nitrogen (one tube for filling, the second one for ventilation). The atomic beam passes through the trap container in a tube of 25 mm diameter, which is welded to the trap container on the axis of the atomic beam. To increase the trapping surface of the construction we added two thin wall tubes to the container, each of 40 mm length, they are mounted into the tube for the atomic beam. The container volume is relatively small and the trap is mounted very close to the oven, so we have to fill the trap each half an hour to keep the performance of the trap constant.

To avoid build-up of Rb vapor inside the experimental chamber, we send the atomic beam after passing the experimental chamber into a second liquid N_2 trap, which is mounted on a DN 63CF flange to the experimental chamber. The construction of this trap is very similar to the trap described above, but the volume of the second trap is much larger than that of the first one. The trap body is made as a tube with two oppositely positioned connection flanges (DN 63CF plus DN 40CF) and a DN 100CF flange to attach the trap container. The trap volume is $\approx 0.5l$, one complete filling is enough for 4 hours of operation.

⁶Performance of the gaskets mounted on the small windows ($\varnothing = 40\text{ mm}$) could be improved using 12 compressing screws instead of 6 (standard). We sealed the small leaks on some $\varnothing = 40\text{ mm}$ windows with a special leak sealant (LeakSeal[©], Caburn).

2.1.4 Baking Procedure and Leak Tests

Obtaining UHV pressures requires careful assembly of the vacuum components. Especially, one has to make sure that all of the components are clean. All the vacuum parts are first cleaned with acetone in an ultrasonic cleaner. After the cleaner, the parts are rinsed with spectroscopy-grade alcohol and dusted off with clean dry air, before they are assembled. Also the copper gaskets are wiped with ultra-pure alcohol before installation to remove any factory residue. Significant improvement of the vacuum condition can be achieved after removing water remains from inner surfaces of the vacuum chamber. For this purpose, the entire vacuum chamber is heated to a temperature of about 250°C and pumped for several days. After the vacuum system is cooled down, the pressure decreases significantly.

Heating from room temperature to 250°C was done in ≈ 10 hours. When the final temperature is reached, the vacuum pressure has risen by a factor of 1000⁷. Baking⁸ the vacuum chamber for a week results in a pressure improvement of a factor of 50. A good option is to connect a mass spectrum analyzer to the vacuum chamber. In this case, the composition of gases inside the vacuum chamber can be monitored. One can easily recognize on every stage of the baking procedure, if a vacuum failure has happened. Cooling the vacuum chamber down to room temperature should be done slowly (at least not faster than heating it up) in order to prevent cracks in windows and leaks at the gaskets. If no leaks have appeared, the vacuum pressure has now improved by a factor up to 100. If the vacuum pressure shows no improvement after baking or becomes even worse, the vacuum chamber has to be checked for leaks. To do this, we used a helium leak detector, see Appendix E.2. The leak rate is measured in mbar l/s. Testing our vacuum chamber after the baking procedure we found several leaks on the 10^{-8} mbar l/s level, by tightening windows and using LeakSeal glue, we reduced the leak rate down to the lower detection limit of the leak tester: $5 \cdot 10^{-11}$ mbar l/s.

2.2 Compensation of Stray Magnetic Fields

To perform the experiments with cold atoms in dark states it is necessary to compensate stray magnetic fields in the interaction region. These residual magnetic fields occur from the massive metal parts in the laboratory and building constructions and from the earth's magnetic field. To realize the compensation, we placed magnetic coils around the experimental chamber, see Fig. 2.5. The compensation coils are made from a braid wire wrapped on aluminium profiles arranged as a cube with 430 mm side length. The regulation electronics provides a controllable constant current in each coil.

To find the proper settings for each coil, we made series of calibration measurements. The idea of these calibration measurements is to use the dependence of the width of dark resonances [7, 5] on the magnetic field. The dark resonances appear as a result of population trapping in a coherent superposition of several atomic levels Ψ , thereby, the

⁷There is a large amount of material driven off the walls of the vacuum system during the initial several hours of the bake. Usually, the pressure after assembling the vacuum chamber is 10^{-8} mbar and goes up to 10^{-5} mbar after the chamber is heated.

⁸Baking at a temperature higher than 180°C promotes the evaporation of water from the chamber surfaces, when the temperature is higher than 250°C, hydrogen will be also removed.

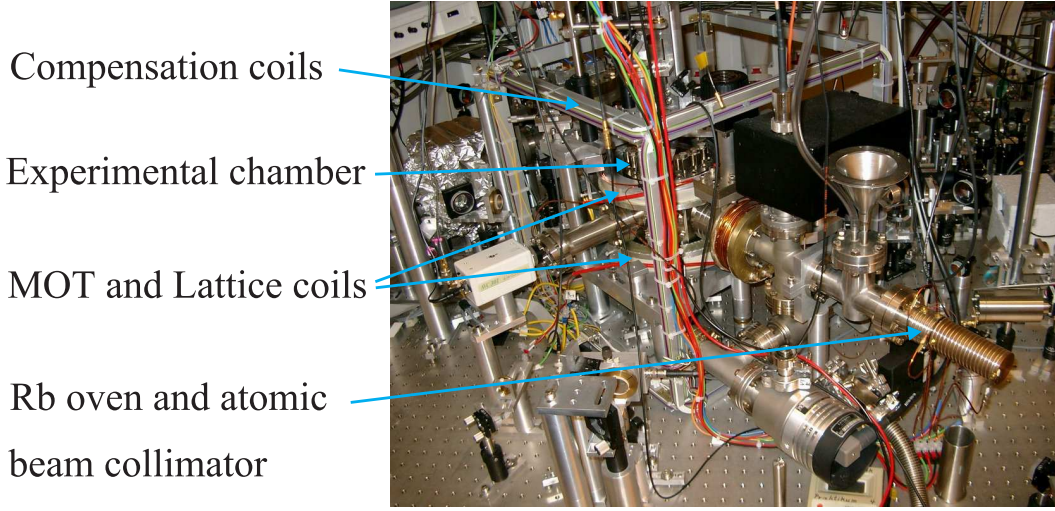


Figure 2.5: A view on the experimental apparatus. Compensation coils are arranged as a cube with 430 mm side length around the experimental chamber.

probability amplitudes for the absorption of a definite light field can interfere constructively or destructively. The transition rate from such a state consists of the sum of the transition rates from the individual levels building a superposition state. This sum can vanish for certain couplings and one observes a sharp decrease of the fluorescence signal, the dark resonance appears. In the case of constructive interference of the excitation pathways the sum takes on its maximum value and the excitation probability of the system is higher when it is in the coherent state Ψ . The fluorescence signal increases and one registers a bright resonance.

To describe the method let us briefly review the physics of coherent population trapping. Consider a system, where an atom with a ground state ($|q\rangle$) $F = 1$ and excited state ($|e\rangle$) $F = 0$ interacts with an electromagnetic field propagating in z direction and being linearly polarized along the x direction. If the quantization axis is oriented along the z direction, one can decompose the electric field into two components with orthogonal circular polarizations (σ_+ and σ_-). The laser frequency ω coincides with the atomic transition frequency. A static magnetic field of strength B is applied collinear to the laser field wave vector.

The Hamiltonian of the system is:

$$H = H_0 + H_B + V_{AL} \quad (2.3)$$

where

$$H_0 = \hbar\omega |e\rangle\langle e| \quad (2.4a)$$

$$H_B = g\mu_B B (|q, +1\rangle\langle q, +1| - |q, -1\rangle\langle q, -1|) \quad (2.4b)$$

$$V_{AL} = \hbar\Omega \exp(-i\omega t) (|e\rangle\langle q, -1| + |e\rangle\langle q, +1|) + H.c. \quad (2.4c)$$

H_0 is the Hamiltonian of the atomic system without magnetic field, H_B describes the energy shifts due to the applied magnetic field (g is the gyromagnetic factor and μ_B the Bohr

magneton), and V_{AL} represents the coupling between atom and laser field⁹. A description of the CPT (coherent population trapping) phenomenon can be simplified in the so-called coupled/noncoupled state basis [4]. The new basis is composed of the excited state $|e\rangle$ and of the two linear combinations of the ground states:

$$|C\rangle = (|q, -1\rangle + |q, +1\rangle)/\sqrt{2} \quad (2.5a)$$

$$|NC\rangle = (|q, -1\rangle - |q, +1\rangle)/\sqrt{2} \quad (2.5b)$$

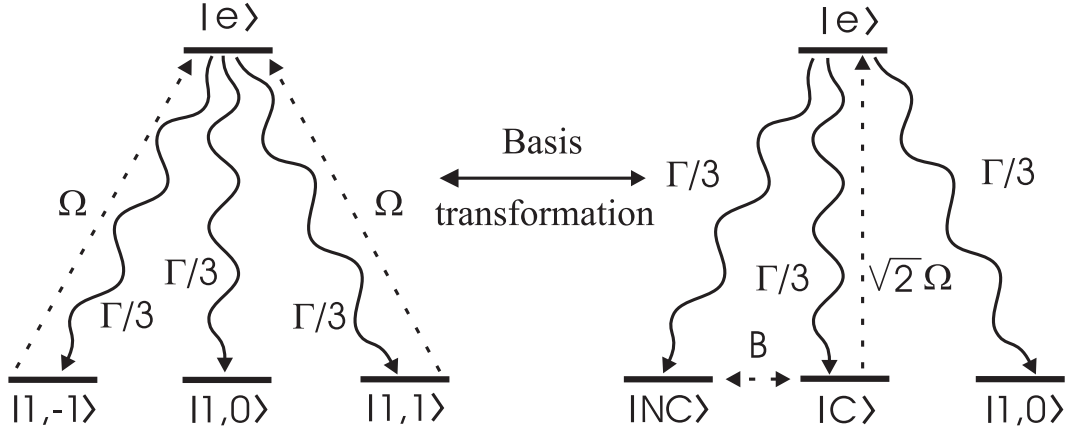


Figure 2.6: Interaction scheme of the transition $|F_g = 1\rangle \rightarrow |F_e = 0\rangle$ resonant with two σ_+, σ_- laser fields. Left: the basis $\{|F_g, M\rangle\}$ is used for the ground state. Right: the basis of coupled/noncoupled states is used.

The noncoupled state $|NC\rangle$ is decoupled from the laser field for any value of the applied magnetic field B . On the other hand, the magnetic field induces a coupling between $|C\rangle$ and $|NC\rangle$. The state $|C\rangle$ is coupled to the excited state via the laser field. The couplings due to the Hamiltonian $H_I = H_B + V_{AL}$ are:

$$\langle C|H_I|NC\rangle = -g\mu_B B \quad (2.6a)$$

$$\langle e|H_I|NC\rangle = \sqrt{2}\hbar\Omega \exp(-i\omega t) \quad (2.6b)$$

as shown in Fig. 2.6. In this new basis, the state $|1, 0\rangle$ can absorb only light with π polarization, i.e., polarized along the z axis. The state $|C\rangle$ absorbs only light with polarization along the x direction, and the state $|NC\rangle$ only light with polarization oriented along the y axis. Since the light is polarized along the x direction, the atoms in the states $|1, 0\rangle$ and $|NC\rangle$ cannot interact with the light field, nevertheless, these states are populated through the spontaneous decay from the excited state $|e\rangle$. The atoms in the state $|NC\rangle$ are in a so-called *dark state* and can absorb only if the light has y polarization. Remaining in the basis $\{|F, M_F\rangle\}$, one could explain the transition of an atom in the coherent superposition $|NC\rangle$ through the coherence transfer of two circularly polarized light fields via a two-photon Raman transition. The levels participating in the formation of the dark state are connected through "Λ chain" (σ_+ and σ_- transitions on the left side in Fig. 2.6). Such a coupling

⁹The expression for V_{AL} is derived in the dipole and rotating-wave approximation.

should satisfy the Raman resonance condition: $\delta_r = (\omega_{L1} - \omega_{L2}) - \omega_{12} = 0$ with ω_{L1} and ω_{L2} being the frequencies of the light fields and ω_{12} the frequency difference of the coupling states. In our example, we have $\omega_{L1} = \omega_{L2}$, and the dark resonance appears only in the vicinity of $\omega_{12} = 0$. An applied magnetic field destroys the nonabsorbing (dark) state and produces an absorption with a linewidth determined by the relaxation rate of the coherent superposition. Therefore, the Hanle effect [16] in the ground state of an atomic system appears as a decrease in the atomic absorption, with a minimum centered at zero magnetic field and a linewidth determined by the relaxation rate of the ground state coherences.

Recently, it was experimentally shown that for the transitions from $F > 0$ into $F' = F + 1$, the constructive interference of the excitation pathways is possible and so the corresponding resonance changes the sign - it becomes bright [2, 49]. Owing to the fact that the degeneracy of the excited state is larger than of the ground state, the sublevels of the excited state also take part in the coupling process. The superposition state is not stable and can decay via spontaneous emission. The coupling of this state to the light field is strong and, therefore, only closed transitions contribute to the bright resonance signal. The appearance of bright resonance at $B = 0$ could be explained as follows [62]: When $B = 0$, the atoms accumulate mostly in the level interacting more with the light field (bright state), leading to a maximum in the fluorescence. When a magnetic field orthogonal to the quantization axis is applied, the populations of the ground states will be partially redistributed, because the Zeeman states are no longer eigenstates of the energy for $B = 0$. Thus, the population of levels weakly coupled to the excited state will increase at the expense of the population of the bright states. This redistribution, leading to a decrease of the fluorescence rate, explains the bright resonance.

In our calibration measurements we register the dependence of an absorption signal on the magnetic field. A linearly polarized laser beam, slightly detuned from the ^{85}Rb D2 line $3 \rightarrow 4$ transition (MOT transition) and with a laser intensity well below saturation, propagates through the experimental region perpendicular to the atomic beam, see Fig. 2.7. Three pairs of magnetic coils, orthogonally oriented with respect to each other, produce the magnetic field. The compensation procedure works as follows: For the polarization of the laser beam depicted in Fig. 2.7, the magnetic field B_z is tuned to obtain the Hanle signal at the zero value of the scanned magnetic field B_y . The magnetic field B_x is set to minimize the width of the resulting Hanle resonance. The absorption of the laser beam is measured as a function of the scanning magnetic field. The sample of such calibration measurement is shown in Fig. 2.8. Fitting the experimental signal with two Lorentz functions, we obtain the width of the bright resonance of 27 mG. The width of this resonance is limited by several processes: transit time broadening and inhomogeneity of the magnetic field in the interaction region. The transit time broadening results from a limited interaction time of the atoms with the light field. If the interaction time of atoms is Δt , then according to the uncertainty relation $\Delta E = \hbar/\Delta t$, the line broadening is $\Delta\nu = 1/(2\pi\Delta t)$. Considering a laser beam with a Gaussian form and an atomic beam with Maxwell velocity distribution, we get [21]:

$$\Delta\nu = 2\sqrt{2\ln 2} \frac{v_p B}{\pi d}, \quad (2.7)$$

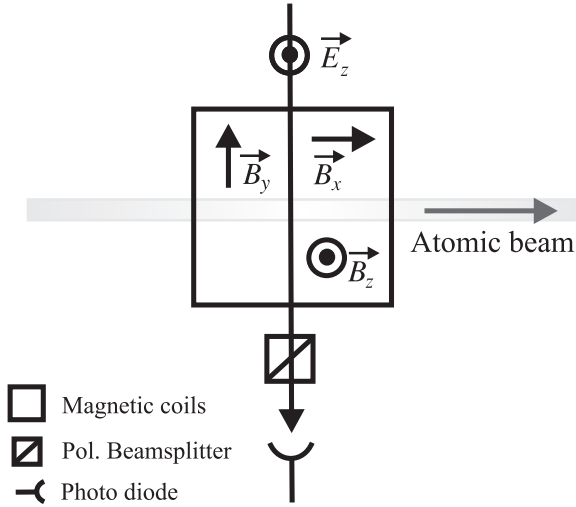


Figure 2.7: Experimental scheme for compensation of stray magnetic fields. Probe transmission signal is measured as a function of the magnetic field. A sample of such measurement is shown in Fig. 2.8. See text for more details.

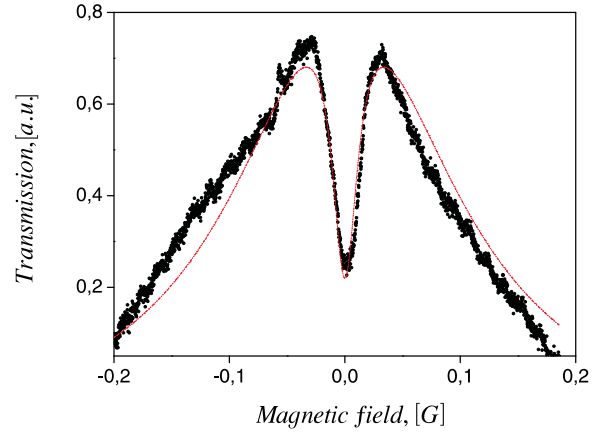


Figure 2.8: An example of the signal from the calibration measurement. The bright resonance in the vicinity of zero magnetic field is a Hanle resonance, whose width is dependent on the quality of the compensation of stray fields in the interaction region. The dashed line is a fit to the experimental data. The width of the resonance is 25 mG.

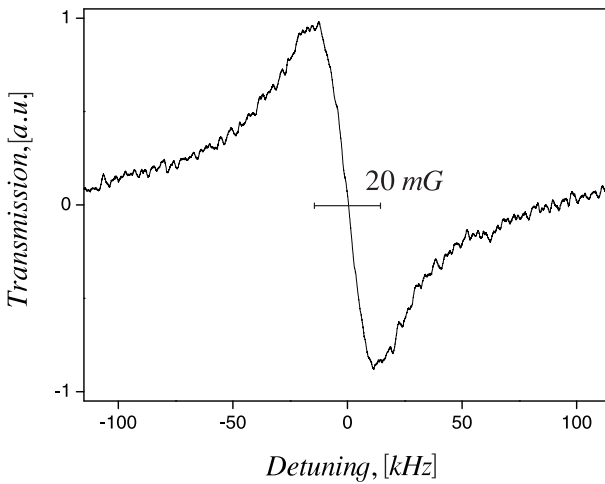


Figure 2.9: Sample of the test measurement of the stray magnetic fields compensation.

with $v_{pB} = \sqrt{3k_B T/m}$ being the most probable velocity in the atomic beam and d the diameter of the laser beam. As can be easily shown¹⁰, the linewidth of the Hanle resonance in Fig. 2.8 is mainly caused by transit time broadening. The other effect which can influence the signal width, is the inhomogeneity of the magnetic field across the interaction region. Actually, the atomic beam diameter is ≈ 30 mm, but the region where the compensation magnetic field is homogeneous is only about 1 cm^3 . After the compensation settings for all three pairs of the compensation coils are found, these settings are fixed. To control that the compensation settings are still correct, we make measurements in regular time intervals. We perform the Raman spectroscopy of magnetic sub-

¹⁰Under the following experimental conditions: a diameter of the laser beam 8 mm, the most probable velocity in the atomic beam 337,3 m/s (beam @ 400K), the transit time broadening is 22.5 mG.

levels of the ground state. For these measurements we use an arrangement of Raman spectroscopy shown in Fig. 5.19. From this arrangement we use only the probe beam and one copropagating pump beam. The polarization of the beams should be oriented perpendicular to each other and parallel to the magnetic fields components along x and z directions. The pump beam is set to the frequency of the dark optical lattice (60 MHz blue detuned from the $F=3 \rightarrow F'=3$ resonance of D1 line) and the probe beam frequency is scanned across the frequency of the pump beam. In the presence of a magnetic field, the transfer curve splits into resonances with the splitting frequency depending on the magnetic field [73]. If all magnetic fields are well compensated, the width of the central structure in the transmitted signal is limited by transfer time broadening to a similar value as in the Hanle resonance measurement as depicted in Fig. 2.9. In conclusion, we compensated the residual magnetic fields to a value of 20 mG, which is sufficiently small to perform the experiments which are the topic of this thesis.

2.3 DAQ System

For carrying out precision measurements on cold atoms, a good control and data acquisition (DAQ) system is necessary. As a control unit we use the ADwin-Gold fast realtime system, whose main feature is a deterministic and robust operation on a 25 ns scale independent of a Windows-PC. A charge-coupled device (CCD) camera, high quality digital oscilloscope (see Appendix E.2) plus self-made external electronics and software, complete the DAQ system.

The following subsection gives an overview of the hardware and software we use in our DAQ and control system.

2.3.1 Control System Hardware

The main unit for controlling the signal sequences in our experiments is the ADwin-Gold system. This system has the following features: 32-bit floating point digital signal processor (DSP) with 512KB CPU RAM and 16MB DRAM, 16 analog inputs, 8 analog outputs with $10 \mu\text{s}$ setting time and 32 digital inputs/outputs. The unit has a compact metal enclosure and is connected via a link cable and acquisition card to a commercial PC with a Pentium III 500 MHz processor.

The experimental control signal sequence is composed of TTL signals, signals with variable DC voltage and voltage ramps. The TTL signals for controlling mechanical shutters and triggering of electronics, as well as DC voltage signals for controlling the laser and magnetic field parameters, are produced directly by the ADwin system. To produce a ramp for scanning the frequency of the test beam and lowering the intensity of the trapping laser, we built additional electronics. This is a set of controllable integrators, whose integration time and amplitude of the output signal are controlled by DC signals from the ADwin system.

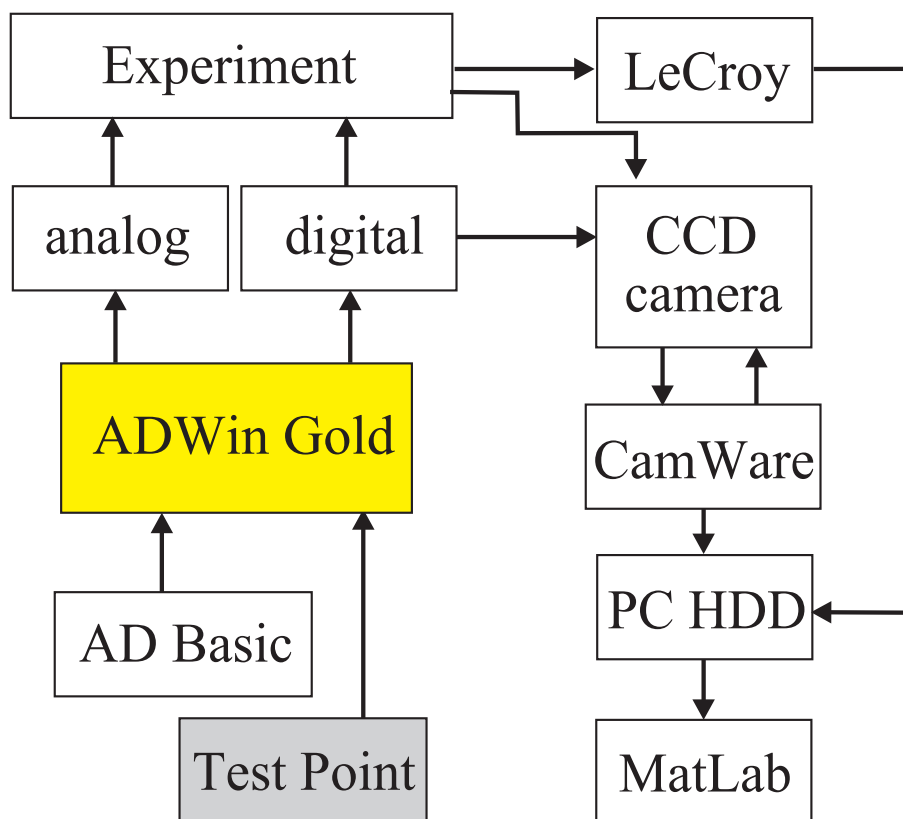


Figure 2.10: Scheme of the experimental control system. The graphical development system *TestPoint* serves as input interface for all experimental parameters.

2.3.2 Control and DAQ Software

The general scheme of the experimental control system is shown in Fig. 2.10. The control signal sequence is programmed with the ADBasic programming language. The code is sent to the ADwin system and operates there in real-time, independently from the main PC. For the parameter input, a *TestPoint* (for details see Appendix E.2) environment was used, in this object oriented language, we create a parameter input window. All experimental parameters such as time settings for the analog and digital output channels, control levels for AOMs, magnetic coils, the experimental cycle time, and number of cycles are set in this window. The *TestPoint* software also makes the calculations between parameter values and control signal values, as in the case of AOMs, whose response to variation in RF power is strongly non-linear. From the *TestPoint* software the signal values and parameters are transferred into the ADBasic program and then to the ADwin processor. The time step of the ADwin system was set to $10\ \mu\text{s}$ in order to provide steep slopes of output analog signals and stability of the control sequence at the same time. The ADwin processor works in cycles and each experimental run is repeated again and again until the experiment is stopped. All mechanical shutters have some time delay and different closing times, so that exact controlling of the timing is necessary. The timing of the experimental sequence is verified with the digital oscilloscope (LeCroy) by comparing the timing of ADwin output

signals and signals from the photodiodes, positioned in the laser beams behind the shutters. We also verified the adjustment of the dark lattice via Raman spectroscopy. These spectra are averaged with the oscilloscope over many experimental cycles and saved on the hard disc drive of the computer.

The CCD camera is controlled by CamWare, a commercial software developed by PCO company. This software controls and reads out the camera. With this software we are able to choose all relevant parameters for the image such as exposition time and binning factor. The images were stored first in a PCO-own 12-bit format (.b16) and are later converted to the ASCII format for analyzing them with self-made MatLab routines. Number of atoms, atomic density, and Gaussian width of the atomic sample in both horizontal and vertical directions are deduced from the gray levels of the image.

2.3.3 CCD Camera System

To take an image of the atomic cloud we use a high performance digital 12-bit CCD camera system (for details see Appendix E.2). The system consists of an ultra compact camera head, which connects to a standard PCI board via a high speed serial data link. The available exposure times range from $10\ \mu\text{s}$ to 10 s. A digital temperature compensation is integrated instead of a space consuming thermoelectrical cooling unit. All camera functions can be remotely accessed and controlled via a digital interface. To collect the fluorescence on a CCD chip we use a commercial television objective (for details see Appendix E.2) together with a 30 mm spacer between camera head and objective to adjust the minimal focal distance of the objective.

Chapter 3

Laser System

All laser systems that we use for our experiments are self-made systems based on commercially available laser diodes. Diode lasers offer many benefits for atom trapping experiments: they are widespread in industry (for the wavelength of Rb) - and, thus, are low cost and easily available, easy to frequency lock and to align, require little maintenance, but they are typically low power (50 mW). For efficient trapping of large numbers of atoms at high densities, this power is not sufficient. Therefore, we use a different type of semiconductor laser - a tapered amplifier - for increasing the output power.

In this chapter, we describe the construction and stabilization method of grating-stabilized and tapered amplifier diode laser systems, that were used in our experiments.

3.1 Master Laser

Let us briefly summarize the features of free-running index-guided single-mode laser diodes. The gain profile of such a laser diode is typically about 10 nm. The emission wavelength is set by competition between the longitudinal modes of the laser cavity, typically separated by 100-200 GHz. Temperature variations cause a change of the cavity length and a frequency shift of the gain profile, so the emission wavelength can be tuned by varying the temperature. However, in the tuning process, the gain of the modes varies in a way that at some point the laser emission frequency jumps from one mode to another, so-called "mode-hopping" occurs, resulting in a number of inaccessible frequency domains. The width of accessible frequency domains is a fraction of the free spectral range of the laser cavity, typically several tens of GHz, while the separation between accessible domains is a multiple of the free spectral length. By varying the injection current of the diode, it is also possible to tune the emission wavelength. This leads to a corresponding temperature change and also a change of the carrier density and, thus, of the refractive index of the semiconductor laser material. Tuning by injection current also suffers from mode hopping. The tuning range by temperature tuning is typically on the order of several tens of nm at a rate of 0.3 nm/K, whereas current tuning typically covers a range of several tens of GHz at a rate of 4 GHz/mA. It should be mentioned that tuning the laser frequency with the injection current is much more quickly than the corresponding tuning due the temperature change. Using a low noise current supply (injection current noise $< 1\mu\text{A}$ integrated over

100 kHz), the linewidth of a free-running, single-mode laser diode is typically on the order of some tens of MHz [63].

3.1.1 Grating Stabilized Diode Laser

Unfortunately, it is not possible to use free-running laser diodes for laser cooling experiments - the mode-hopping behavior and their linewidth which is bigger than the natural linewidth of the atomic transition, make their implementation problematic. These drawbacks of free-running laser diodes can be eliminated by using an optical feedback technique [47]. The emission properties of the diode can be improved if the optical feedback comes from an external resonator with a much smaller linewidth than that of the laser diode (finesse of the external resonator is higher than that from the internal of the laser diode). To realize this coupling, an output facet of the laser diode should be AR coated (this is the fact for the most diode lasers with output power $>20\text{mW}$). Because of the length of the external resonator, its mode spacing is much smaller than that of the internal resonator. To prevent mode hopping one should use a frequency selective optical feedback from an external optical grating. In *Littrow configuration* - the first order reflection from the grating is deflected into the laser diode and the zero order beam serves as the output beam. Adjusting the first diffraction order back into the laser diode provides that the back facet of the diode and the grating form an external cavity coupled to the cavity of the laser diode [78]. This requirement means that the angle of the first order of diffraction Φ_1 is equal to the laser beam incidence angle on the lattice Φ_0 (see Fig. 3.1 for details). The wavelength that fulfills the diffraction condition: $\lambda = 2g \sin \Phi_0$ receives a large amplification and the laser runs single mode at this wavelength (g is grating constant, in our case 1800 mm^{-1}).

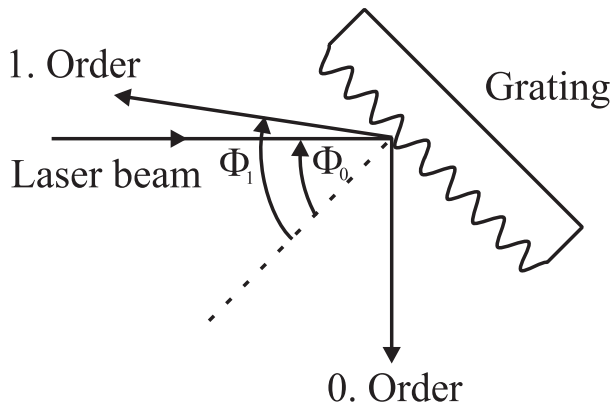


Figure 3.1: Principle of grating stabilization. In the Littrow configuration the first order of diffraction is backreflected into the diode, i.e. $\Phi_1 = \Phi_0$.

The diode is aligned such that the polarization is parallel to the lines of the diffraction grating (vertical to the base mount) - this provides the optimum wavelength selectivity. The divergence of the diode laser beam is corrected by a collimating objective (Optima collimator, see E.2). The axis of the laser diode and the collimator should exactly coincide

Our realization of the grating stabilized laser diode is depicted in Fig. 3.2 and 3.3.

The mounting system consists of three parts: a basis mount, holding the laser diode, an adjustable mount for the collimation optics, and an adjustable mount for the diffraction grating. All metallic parts are made from the aluminium alloy AlZn-MgCu1.5, which provides high heating conductivity and good mechanical elasticity. The laser diode is fixed in the mounting by means of the pressing ring and two small screws. Heat conducting grease provides sufficient thermal coupling between the laser diode and the holders. The emitting light of the laser diode is linearly polarized parallel to the minor axes of the elliptical beam pattern.

(this sets an accuracy challenge for the mechanical workshop). The pre-alignment of the collimator is made by hand and the fine adjustment is done with a micrometer screw which tilts the lever arm of the collimator mount. Some tips for the adjustment procedure can be found in [63]. The diffraction grating is cemented to an adjustable lever arm of the mounting. The fine adjustment of the angles between grating and the incident laser beam is achieved through the micrometer screws positioned at the grating and the base mount. A low voltage piezoelectric transducer (PZT) is placed between the lever and the micrometer screw and is used for scanning and for stabilizing the output wavelength to the atomic resonance. A thermal sensor (AD 590) is fixed on the base mount close to the laser diode. The base mount is placed on a Peltier element mounted on an aluminium base plate, acting as a thermal sink. The temperature of the entire system is stabilized to within few mK , using an electronic servo-loop. A good alignment of the laser system is characterized by a decrease of the threshold current by about 10-15% (for Hitachi laser diodes typically 7-8 mA) as compared to the threshold of free-running diode.

We tested three different laser diode types in our experiments: Sanyo DL7140201, Mitsubishi ML64114R, and Hitachi HL7851G. Hitachi laser diodes (for details see E.2) are the most robust with the longest lifetime and reliable results of spectral characteristics and output power. No additional antireflection coating on the laser diode facet is required due to the fact that about 25% of the incident power was coupled back to the diode from the diffraction grating.

The entire setup is shielded by a metal cover in order to protect the laser against electromagnetic fields and to improve its thermal isolation. In that way, the frequency drift of the laser system is limited to less than 10 MHz over a few minutes and remains below 50 MHz over a few hours. Properly aligned, the system emits at the same frequency within 100 MHz over weeks, without the necessity of realignment. The emission linewidth is reduced to about 1 MHz [63]. When the output frequency is locked to the atomic transition by means of low-bandwidth servo-electronics, a stable emission with a linewidth of typically 500 kHz can be achieved. This fact was demonstrated by analyzing a beat signal from two independent, grating stabilized lasers locked to the Rb resonance.

3.1.2 Pound-Drever-Hall Stabilization

The grating stabilized diode laser system described above, permits reducing the laser linewidth well below the values of the natural linewidth of ^{85}Rb D1 and D2 lines (5,4 MHz and 5,9 MHz respectively). Further, the active stabilization of the laser frequency is required to run the experiments. The stabilization of the laser frequency is based on the comparison of the actual value of a signal connected with the frequency of the laser with the desired value of this signal, which results in a so-called "error signal". The stabilization electronics transforms the error signal into control signals for the laser diode current and for the PZT connected to the diffraction grating, which correct the deviation of the laser. For any stabilization method, the following components are necessary: frequency reference, linear error signal with a steep slope, and a zero signal at the required frequency. As a frequency reference, we take an absorption signal of the atomic resonance. To obtain the doppler-free spectrum of atomic resonances, we used the well-known scheme of saturation spectroscopy [21]. The realization of this scheme is shown in Fig. 3.4. An example of the

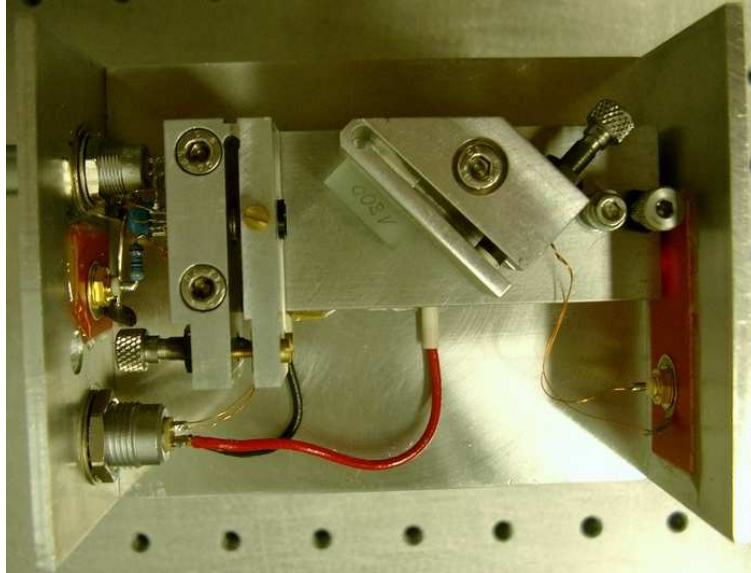


Figure 3.2: Picture of the diode laser setup. Comparing this photography with Fig. 3.3, one can easily recognize all the important parts of the setup.

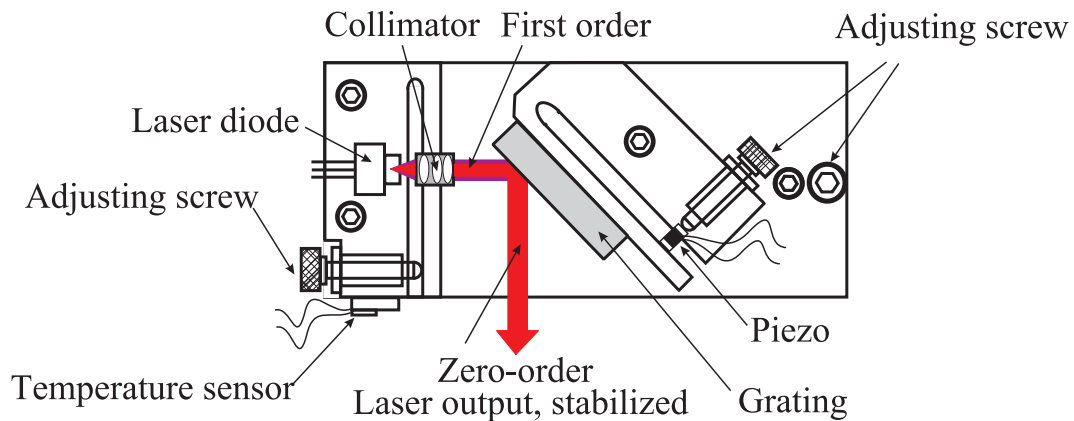


Figure 3.3: Schema of the mechanical setup of the grating stabilized diode laser system. Diffraction grating, laser diode, and collimation optics are mounted on the flex stage, which is fixed to the Peltier element and temperature stabilized. Grating and collimator are also positioned on the flex mounts. With the micrometer screws, the exact positions of the grating and collimator are adjusted, the fine tuning of the grating angle is done with the PZT.

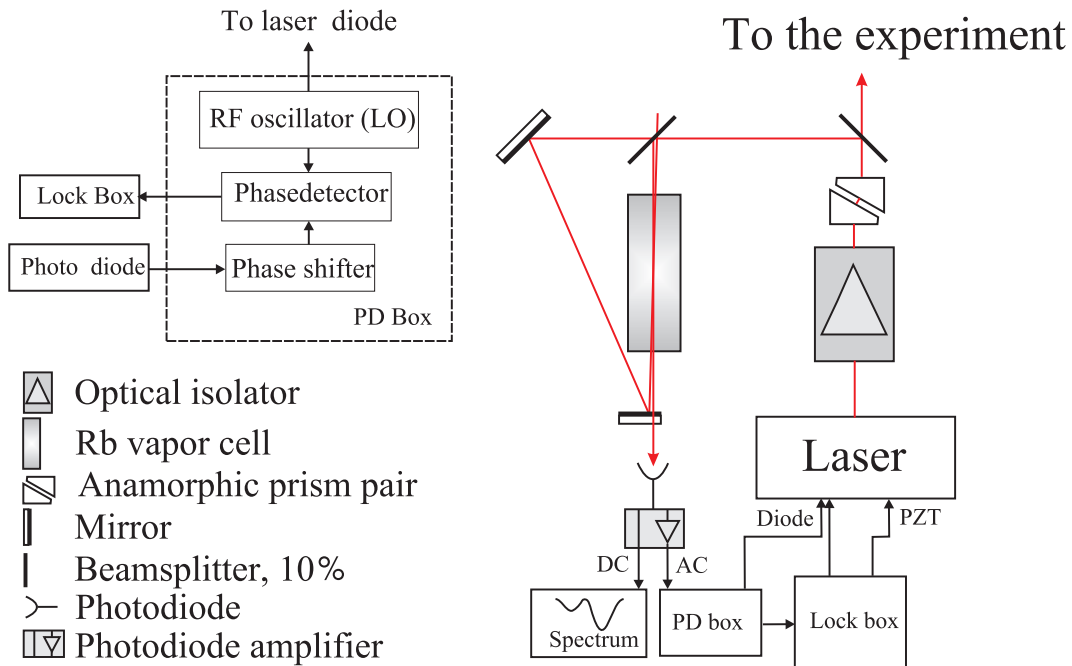


Figure 3.4: *Schema of the laser frequency stabilization to the atomic resonance. In the dashed box, the design of the Pound-Drever box is schematically shown.*

spectrum of Rb lines is shown in Fig. 3.5, a level scheme of the involved transitions is depicted there as well. Several methods of laser frequency stabilization exist, they can be divided into two groups: amplitude stabilization methods and phase stabilization methods. The difference between them is the way how an error signal is created. The first type - amplitude stabilization - is easy to implement. An input signal for the stabilization electronics (a simple PID¹ stabilizer, so-called "lock-box") is taken directly from the transmission signal of the saturation spectroscopy after passing an "offset-box" - a simple electronics that adds some DC level to the signal. The first drawback of this stabilization scheme is that the frequency cannot be locked everywhere, for example not directly on atomic resonance, since the stabilization works only on the slope of the signal. This can be avoided by the implementation of polarization spectroscopy scheme - through tuning of an additional magnetic field and polarization of probe and pump beams, a resonance can be deformed to obtain a dispersive slope instead of a transmission minimum. In our group, such a stabilization scheme was used in a different experiment, see [54]. The other, more dramatic, drawback is the dependence of the input signal on the amplitude and on the stability of the offset-box electronics. If the spectroscopy setup is not well isolated from all kinds of stray light (reflections from the vapor cell windows, day light, room light), then the stabilization point and hence the output frequency of the laser can be shifted.

More reliable results can be achieved with the second type - the phase stabilization method. In this method, the phase delay (dispersion) of the modulated laser light while passing through a reference medium will be determined by comparing the phases of the

¹PID- proportional integral differential, this electronics has the task to hold an error signal at the desired value and to compensate error signal deviations

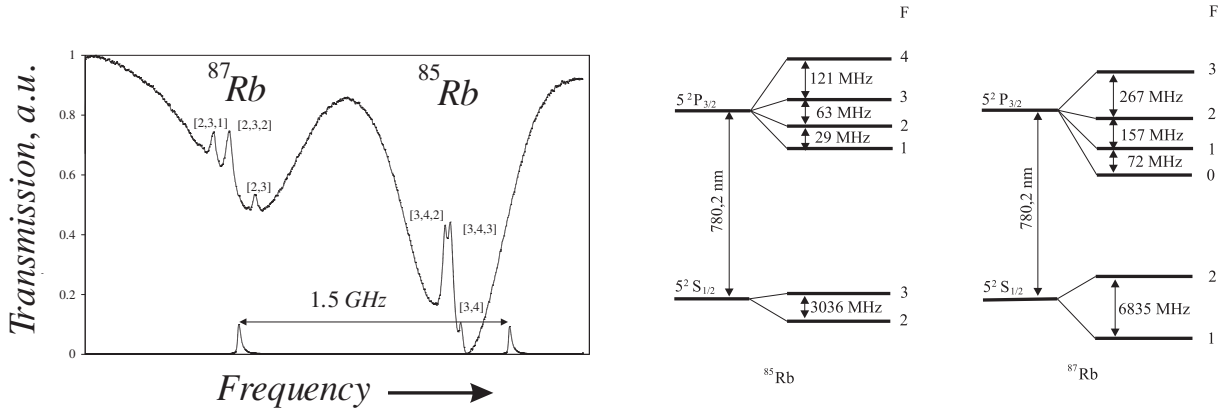


Figure 3.5: Left: Spectrum of the D2 line of Rb. The upper curve shows the doppler-free transmission signal. Transitions $F \rightarrow F'$ are marked in the form $[F, F']$, crossover transitions are marked with $[F, F', F'']$. The lower curve shows the transmission of a Fabry-Perot interferometer, which serves as a frequency reference. Right: the corresponding level scheme of Rb.

carrier and the side band, hence an error signal originates. The scheme of our realization of the *Pound-Drever-Hall*² stabilization is depicted in Fig. 3.4. The local oscillator (LO) produces a stable radio frequency at 40 MHz. The laser diode current is directly modulated with the frequency of the LO, the modulation index is small and adjusted in such a way that the sidebands are not well expressed. Neglecting amplitude modulation, a laser diode with current modulation emits the following electric field:

$$E(t) = \frac{E_0}{2} \exp[i(\omega_0 t + M \sin(\omega_m t))] + c.c. \quad (3.1)$$

where ω_0 is the emission frequency of the unmodulated laser light, ω_m is the modulation frequency, and M the phase modulation index. Using the series expansion by Bessel functions $J_k(M)$ and taking in account that M is small we get:

$$\begin{aligned} E(t) &= \frac{E_0}{2} \sum_{k=-\infty}^{\infty} J_k(M) e^{i((\omega_0 + k\omega_m)t)} + c.c. \\ &\approx \frac{E_0}{2} \left(J_0(M) e^{i\omega_0 t} + J_1(M) e^{i(\omega_0 + \omega_m)t} - J_1(M) e^{i(\omega_0 - \omega_m)t} \right) + c.c. \end{aligned} \quad (3.2)$$

The modulated light is passing through atomic vapor in a setup of saturation spectroscopy and the electric field is transformed to:

$$E_T(t) = \frac{E_0}{2} \sum_{k=-\infty}^{\infty} J_k(M) T_k e^{i((\omega_0 + k\omega_m)t)} + c.c. \quad (3.3)$$

with transmission coefficients given by $T_k = \exp(-\delta_k - i\phi_k)$ with absorption $\delta_k = \alpha_k I/2$ and phase delay $\phi_k = n_k I \omega_m/2$. A photo detector with a bandwidth higher than the

²This method is based on the activities of Pound and Drever, see in the field of frequency modulated spectroscopy [24, 57]. A good overview is given in [9].

modulation frequency ω_m detects all frequency components of the transmitted intensity:

$$I_T(t) = \frac{c\epsilon_0}{2} |E_T(t)|^2 \quad (3.4)$$

In the approximation of slowly varying absorption and phase delay and for the small modulation index M , the signal measured by the photo diode can be expressed as:

$$I_T(t) \sim e^{-2\delta_0} M \left(1 + (\delta_{-1} - \delta_1) \cos(\omega_m t) + (\phi_1 - \phi_{-1} - 2\phi_0) \sin(\omega_m t) \right) \quad (3.5)$$

This signal consists of a dispersive part - an in-phase contribution $(\phi_1 - \phi_{-1} - 2\phi_0)$ - and

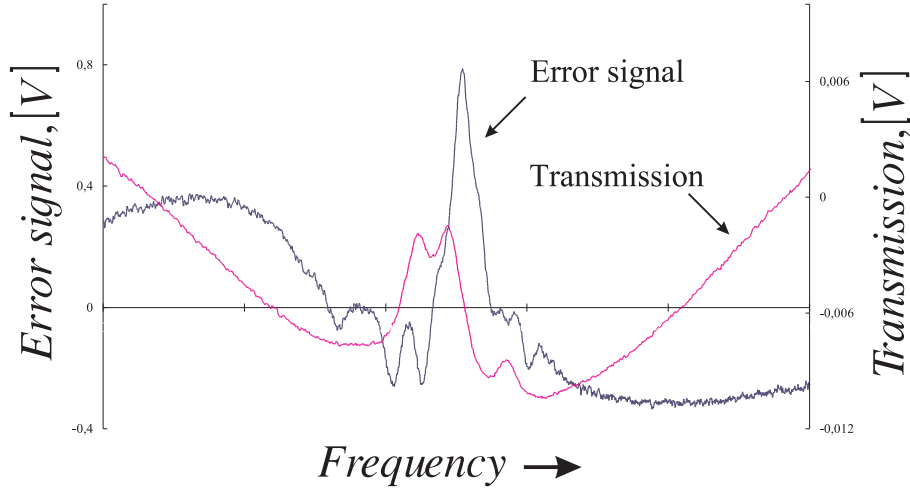


Figure 3.6: An example of signals from saturation spectroscopy and an error signal used for the stabilization. For better visualization, both signals are scanned over the frequency domain of about 1 GHz and show the hyperfine spectrum of the D2 line of ^{85}Rb .

an absorption part - a quadrature contribution $(\delta_{-1} - \delta_1)$. The signal of the photo detector is fed into the phase detector, where the frequency components with ω_m are mixed with $\sin(\omega_m t)$ and converted to a DC signal. The result of this conversion depends on the phase between the photo diode signal and the signal from the local oscillator. In the case that the in-phase component is converted, we get a dispersive signal. The example of such a signal is shown in Fig. 3.6. To stabilize the laser, one has to set the desired point on the slope of an error signal to zero voltage. An offset is added to the error signal because the background from a Doppler profile of the resonance sets the position of a local maximum of transmission, and hence, the positions of the resonances. A servo signal produced by a lock-box, sets the length of the PZT of the grating and diode current of the laser, closing the servo loop.

3.2 Amplifier (Slave Laser)

The laser system described in Sec. 3.1.1 has for our application only one drawback, namely the output power. The nominal output power of free-running single-mode laser diodes is

typically about 50 mW³, the total output power of the grating stabilized laser system is therefore maximally 30-35 mW⁴. For some applications, for example for a MOT with large capture volume or for a dipole trap, more power is needed. An efficient way to enhance the output power of a diode laser system is to use injection locking of a second laser diode with a higher nominal output power. Several realizations of this method are known. First, one can injection lock the same type of laser diode as used in the grating-stabilized setup. In this case, one obtains a laser power of about 50 mW with the same spectral characteristics as the master laser. The gain in power is not very big. A different method uses a broad area laser diode as a "slave" laser in the setup of so-called "V-injection". The laser light from the master laser is injected through the front facet of the slave laser under some angle to the normal of the front facet, the laser beam propagates in the material of the slave laser, is reflected on the rear facet of the chip, and the amplified laser beam leaves the front facet of the slave laser at the angle of deflection. One can gain a factor of 4.5 in output power, see [68]. In our group, such a system was realized and tested [61]. It should be mentioned that these systems have some disadvantages. The gain in power is relatively small compared to the complexity of the optical setup, and they are difficult to adjust.

Another, more efficient way to increase the power of a diode laser system, uses direct injection into a tapered amplifier laser chip.

3.2.1 MOPA Laser Construction

The main part of our master oscillator power amplifier (MOPA) system is a tapered amplifier laser chip (see Appendix E.2 and Ref. [8]). The feature of the tapered amplifier which is responsible for its capability to produce a high-power output, is the special geometry of the gain region. A horizontal cross section of the tapered amplifier (TA) is shown in the magnified detail of Fig. 3.8. The gain region consists of a preamplifier with rectangular cross section (similar to the conventional laser diode), followed by a trapezoidal amplification section. This trapezoidal geometry results in a high output power (up to 500 mW) since the broad output facet of the chip provides a power-density level low enough to avoid destruction of the gain material. The preamplifier region acts as a spatial mode filter for the light injected at the back facet, since it is small enough such that only one spatial mode can propagate. The total gain of the TA chip is on the order of several thousands. Both facets of the TA are antireflection coated to prevent reflection from the facet and weaken the tendency of the TA to start lasing by itself. Unfortunately, the last tendency is not entirely eliminated. Free-running TA emits radiation with a broad frequency spectrum (≈ 10 nm) and a strong central peak with a width of 0.5 nm.

³The maximum output power of the laser diode is limited by the damage threshold of the output facet of the diode. Some new models of laser diodes have higher output power, for example Sanyo DL7140201 - 70 mW. This value is not significantly higher than from a Hitachi diode, but the reliability of these diodes is worse. Other types of laser diodes (broad area laser diodes) with significantly higher output power (500-1000 mW) are not single-mode and not suitable for use in Littrow configuration

⁴The power is reduced due to the reflection losses on the lenses of objective ($\sim 5\%$) and first order reflection from the grating ($\sim 25 - 30\%$)

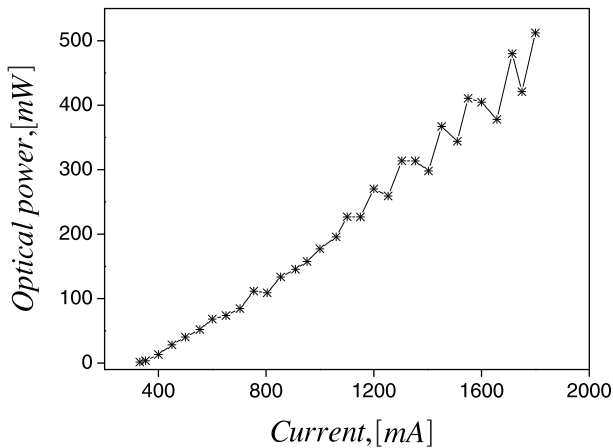


Figure 3.7: Oscillating behavior of the SDL chip, leading to instabilities in output mode quality and power. The graphics shows current-power characteristics of a free-running TA chip.

This feature of a TA chip plays a negative role in its application as a light source for a dipole trap, since the broad emission spectrum has also components near the resonance, therefore, dramatically decrease the lifetime of this dipole trap. Also, some TA chips from the last production cycles may have bad specifications⁵ - an antireflection coating on the facets of the chip is not optimized, resulting in an oscillation behavior of the power-current characteristic, see Fig. 3.7. This leads to mode and power instability of the output and, therefore, more careful adjustment is required. One needs to fine adjust the laser every time the experiment is run. Good features of TA based systems are the high power amplification (up to 250 mW single mode laser power is available by 20-25 mW seeding power) and its relatively easy optical setup.

3.2.2 MOPA Laser System

The scheme of our MOPA set-up is shown in Fig. 3.8, details of the slave laser can be found in Fig. 3.9.

The TA chip is mounted on a temperature stabilized aluminium block. To achieve a high output power with a small frequency bandwidth, the output of a grating-stabilized diode laser (see Sec. 3.1) is injected into the preamplifier region through the back facet of the TA chip. The preamplifier facet has approximately the same shape and dimensions as the output facet of a conventional laser diode, therefore optimal spatial mode matching between TA and master laser chips can be achieved by using equal collimation optics for collimating the master laser and injecting the TA. For this purpose, we use collimation optics from Optima, model 336-1027-660. Another collimator (Melles Griot GLC-001) is placed next to the front facet and provides collimation of the TA output beam. Both injection and output collimator are placed on the adjustable lever arms of the TA chip holder. The position of the collimators can be exactly adjusted by slightly tilting the level arms with micrometer screws. This construction is similar to the diode holder of the master laser, see Sec. 3.1.1. If the master laser is fed into the TA, the output of the TA has the same spectral properties as the master laser and background radiation is suppressed by up to 35 dB. Because of the geometry of the TA, the spatial profile of the output beam is strongly elliptical and astigmatic. Therefore, we use a cylindrical lens and an anamorphic

⁵The production of the SDL 8630 E chip was stopped in 1999. The chip in our dipole trap laser system was manufactured in one of the last production cycles and has negative features connected with the AR coating of the facets. The second SDL chip used in the MOT-MOPA system was produced earlier and does not show such negative behaviour.

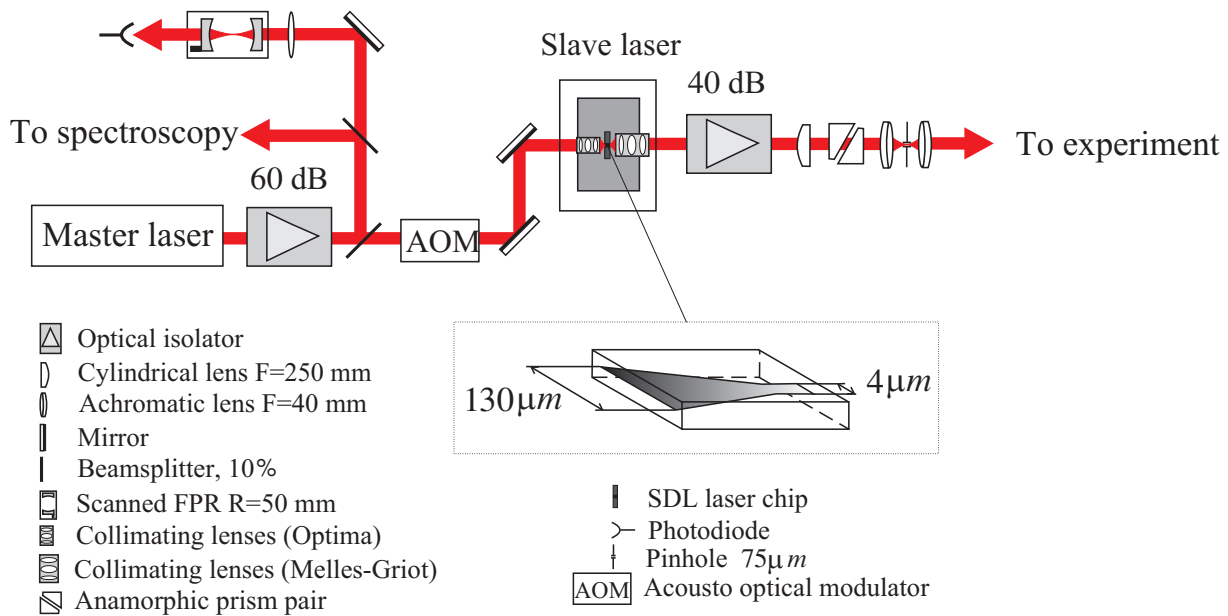


Figure 3.8: *Experimental setup of our MOPA system based on the tapered amplifier (TA). The magnified detail shows the construction of the TA chip.*

prism pair to correct for it. Care has to be taken during the adjustment procedure: the backreflections into the large output facet should be avoided since this can destroy the TA. In this case laser light entering the TA at the output facet would be amplified in the reverse direction and, thus, would lead to very high power densities at the narrow end of the trapezoid. To avoid this, an optical isolator is placed in the beam directly after the collimation lens. An acoustooptical modulator, which is placed between master and slave laser, is used as a quick shutter and sets the desired detuning from the atomic resonance. In our experiment, we use two MOPA systems: the first is used to provide enough power for a MOT with a relatively high capture volume ($\varnothing=25\ \text{mm}$), the second system serves as a light source for a dipole trap. Detailed description of the TA-based optical setup for the MOT and the dipole trap can be found in Sec. 4.4.3 and Sec. 6.3.1, respectively.

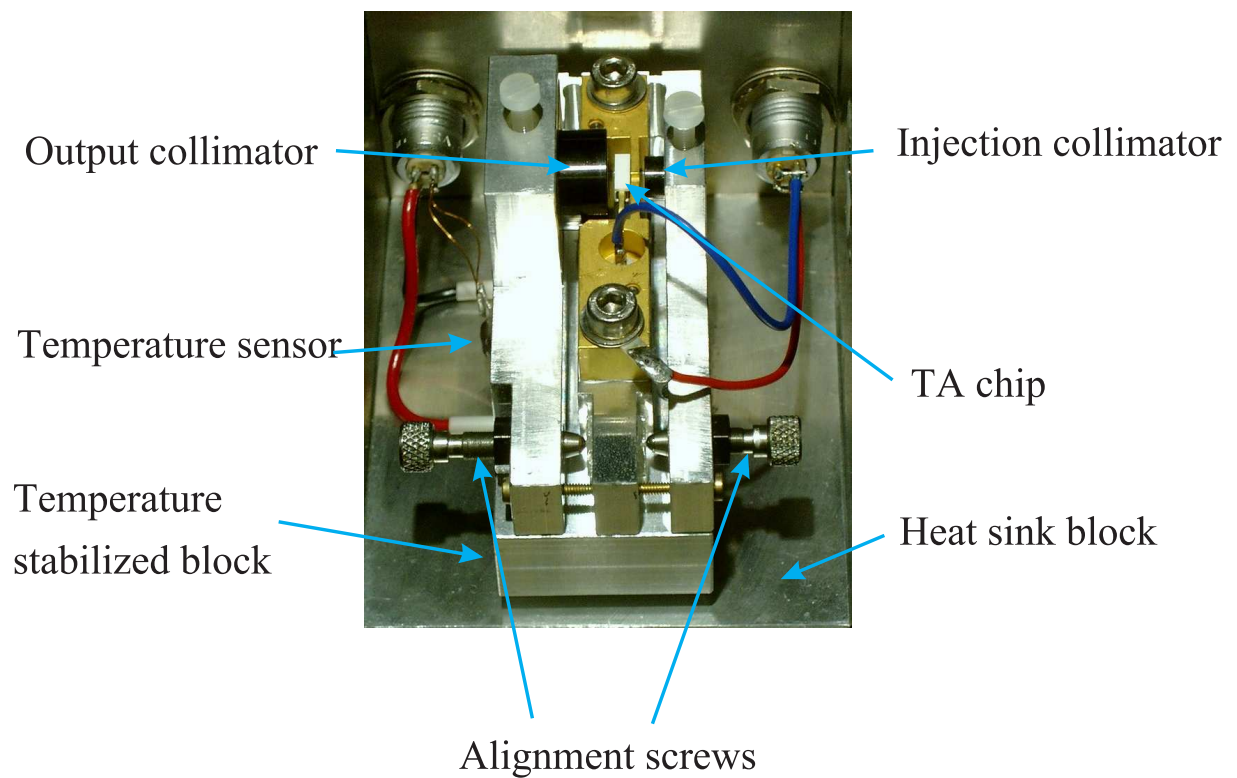


Figure 3.9: A photograph of the slave laser. A Peltier element is placed between heat sink and temperature stabilized blocks.

Chapter 4

Source of Cold Atoms

The experimental investigations of ultracold neutral atoms require methods to cool atoms from initial temperatures of hundreds of Kelvin down to less than 1 mK. The efficient tool to produce such ultracold ensembles of neutral atoms, is the magneto-optical trap (MOT). To cool the atoms, the MOT uses the radiation pressure force, originating from subsequent cycles of absorption and spontaneous emission. In combination with a quadrupole magnetic field, a position dependent force arises and provides a spatial confinement of the atoms. In our experiments, a MOT loaded from a precooled atomic beam produces cold and dense atomic samples in an UHV environment.

In this chapter, the principle of MOT operation is briefly reviewed and our implementation of a MOT with a pre-cooled atomic beam is described and characterized by measurements of the trap density, lifetime and temperature. We briefly compare our MOT setup with other possible implementations.

4.1 Magneto Optical Trap

The idea of a MOT [59] can be easily understood on the example of 1D configuration for a two-level atom with $F = 0$ in ground state and $F = 1$ in excited state, with F - the total angular momentum of the atom. The 1D MOT consists of one pair of counter-propagating laser beams and an inhomogeneous magnetic field. The magnetic field is a linear function of z , $B = bz$, with b being constant. The two laser beams are circularly polarized and red detuned with respect to the atomic resonance. The magnetic field splits the energy levels of the excited state into three magnetic sublevels due to the Zeeman effect. When an atom is moving to the right of the origin, the Zeeman splitting will shift the atom into the resonance with the beam coming from right and out of resonance with the beam coming from left, see Fig. 4.1. This forms the force which is velocity and position dependent. The total force can be written as the force from equation (1.5) with an additional term $\omega_z = \beta z$, which describes the frequency shift of the atomic level due to the Zeeman splitting:

$$\vec{F} = \vec{F}_+ + \vec{F}_- = \hbar \vec{k} \frac{\Gamma}{2} \frac{s_o}{1 + s_o + (2(\delta - \vec{k}\vec{v} - \beta z)/\Gamma)^2} - \hbar \vec{k} \frac{\Gamma}{2} \frac{s_o}{1 + s_o + (2(\delta + \vec{k}\vec{v} + \beta z)/\Gamma)^2} \quad (4.1)$$

In the limit of small atomic velocities ($\vec{k}v \ll \Gamma$) and low laser intensity ($s_o \ll 1$) we obtain the following expression for the total force:

$$\vec{F} = 4\hbar\vec{k}\frac{2\delta}{\Gamma}s_o\frac{(\vec{k}\vec{v} + \beta z)}{(1 + (2\delta/\Gamma)^2)^2} = -\alpha v + \frac{\alpha}{k}\beta z \quad (4.2)$$

where α is the damping constant and α/k the spring constant of the trap. This expression is identical with (1.6) except from the fact that the factor $\vec{k}\vec{v}$ is now $\vec{k}\vec{v} + \beta z$. The inhomogeneous magnetic field produces the position dependent force with friction component. The characteristic damping time constant for Rb-atom and $dB/dx=10$ G/cm is:

$$\tau = k\beta = \frac{\hbar k}{g\mu_B \frac{dB}{dx}} = 0.91ms \quad (4.3)$$

The motion of an atom in the MOT under the action of confining force (4.2) is strongly over damped. This can be seen from the equation of damped harmonic oscillator:

$$\ddot{z} + \gamma\dot{z} + \omega_{trap}^2 z = 0 \quad (4.4)$$

with

$$\gamma = 4\hbar k^2 \frac{2\delta}{\Gamma} \frac{s_o}{M(1 + (2\delta/\Gamma)^2)^2} \quad (4.5)$$

and

$$\omega_{trap}^2 = 4\hbar k \frac{2\delta}{\Gamma} s_o \beta \frac{(\vec{k}\vec{v} + \beta z)}{(1 + (2\delta/\Gamma)^2)^2} \quad (4.6)$$

The following parameter describes a character of the atomic motion in the trap:

$$\frac{\gamma^2}{4\omega_{trap}^2} = \frac{\hbar k^3 2\delta}{\beta\Gamma} \frac{s_o}{M(1 + (2\delta/\Gamma)^2)^2} \quad (4.7)$$

The parameters γ and ω_{trap} have their maximum (for maximum attenuation and rigidity) at $I = I_o$ and $\delta = -\Gamma/2$, so the relation (4.7) takes the form:

$$\frac{\gamma^2}{4\omega_{trap}^2} = \frac{\pi E_{rec}}{4\lambda\beta\hbar} \quad (4.8)$$

This expression gives the ratio between photon recoil energy E_{rec} and the increase of the Zeeman energy over the wavelength $\lambda\hbar\beta$. For typical experimental parameter $\beta = 2\pi \cdot 1.4$ MHz/cm ($b = 10$ G/cm) is the expression $\gamma^2/4\omega_{trap}^2 = 22 \gg 1$ for Rb. The atomic motion in the MOT is commonly strongly overdamped.

The most common scheme of a three dimensional MOT , used in a variety of laser cooling experiments, includes three pairs of laser beams having $\sigma_+ - \sigma_-$ configuration that are mutually perpendicular to each other plus a quadrupole magnetic field, which is generated with a pair of coils positioned in an anti-Helmholtz configuration, see Fig.4.1 for details.

For our investigations we choose ^{85}Rb because the wavelength of its optical transitions can be easily produced with the diode lasers, and due to its physical characteristics trapping

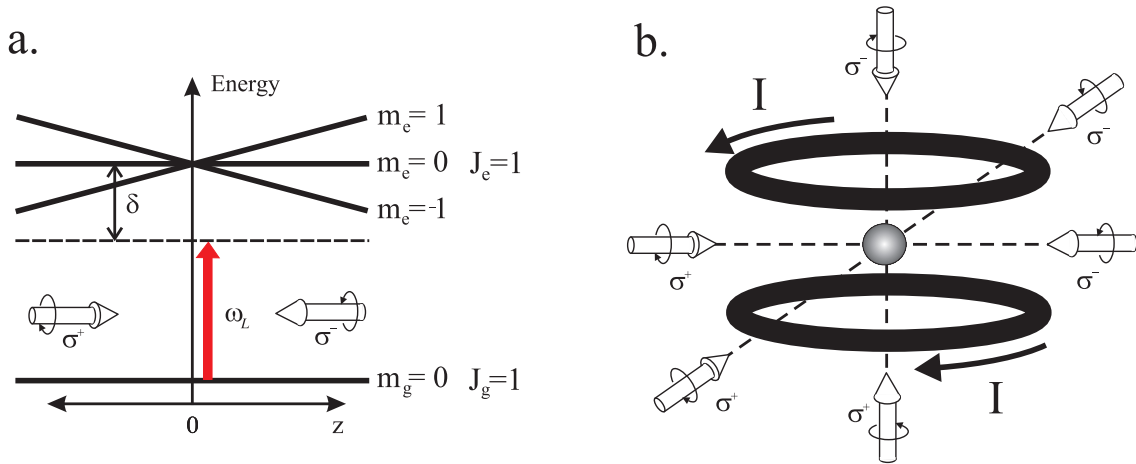


Figure 4.1: Operation scheme of a standard MOT: a. Energy-level diagram of two-level atom, immersed in a magnetic field $B_z(z) = bz$. The frequency and polarization of the counterpropagating laser beams are chosen to produce damping and restoring forces for the atomic motion along the z -axes. b. Trapping scheme in three dimensions. The quadrupole magnetic field is generated by two coils of opposing current. Laser light, indicated by heavy arrows, counterpropagates along x , y , and z , and is polarized shown with respect to the axis of propagation.

and cooling is relatively easily to realize. The cooling cycle is realized on the ($5^2S_{1/2}(F = 3) \rightarrow 5^2P_{3/2}(F = 4)$) transition of the D2-line of ^{85}Rb , see Fig. 4.2. This transition has a wavelength of 780.027 nm ¹ and a natural linewidth $\Gamma/(2\pi) = 5.9\text{ MHz}$. The transition is closed, but due to the relatively small separation between $F=4$ and $F=3$ levels of only 121 MHz and the fact that the typical detuning for MOT operation is $\delta = -2\Gamma$, the probability for the off-resonant excitation into the $F=3$ state is $1/1000$. Once excited into the $5^2P_{3/2}(F = 3)$ state, the atoms can populate the lowest hyperfine state ($5^2S_{1/2}(F = 2)$) over spontaneous decay, and so are loosed for the cooling process. Therefore, an additional (so-called "repumper") laser tuned to the $5^2S_{1/2}(F = 2) \rightarrow 5^2P_{3/2}(F = 3)$ transition, brings the atoms back into the cooling cycle.

4.2 Capture Range of the MOT

The trapping potential of a MOT is typically several mK deep, which means on the velocity scale values less than 10 m/s . Therefore, only the atoms up to this maximal velocity can be captured in the trap. This limitation can be understood from the following consideration: the trapping laser beams are red detuned from the Bohr frequency at zero atomic velocity and zero magnetic field, that is in the middle of the trap. The increasing magnetic field from the trap center outwards shifts the atoms with the decreasing velocity into the resonance with laser, resulting in a resonant condition for a resting atoms at some distance R_C from the trap center. Beyond the sphere with a radius of R_C , also called capture radius, no atoms interact with the trapping light. Only the atoms with a velocity such that their maximum

¹value in air

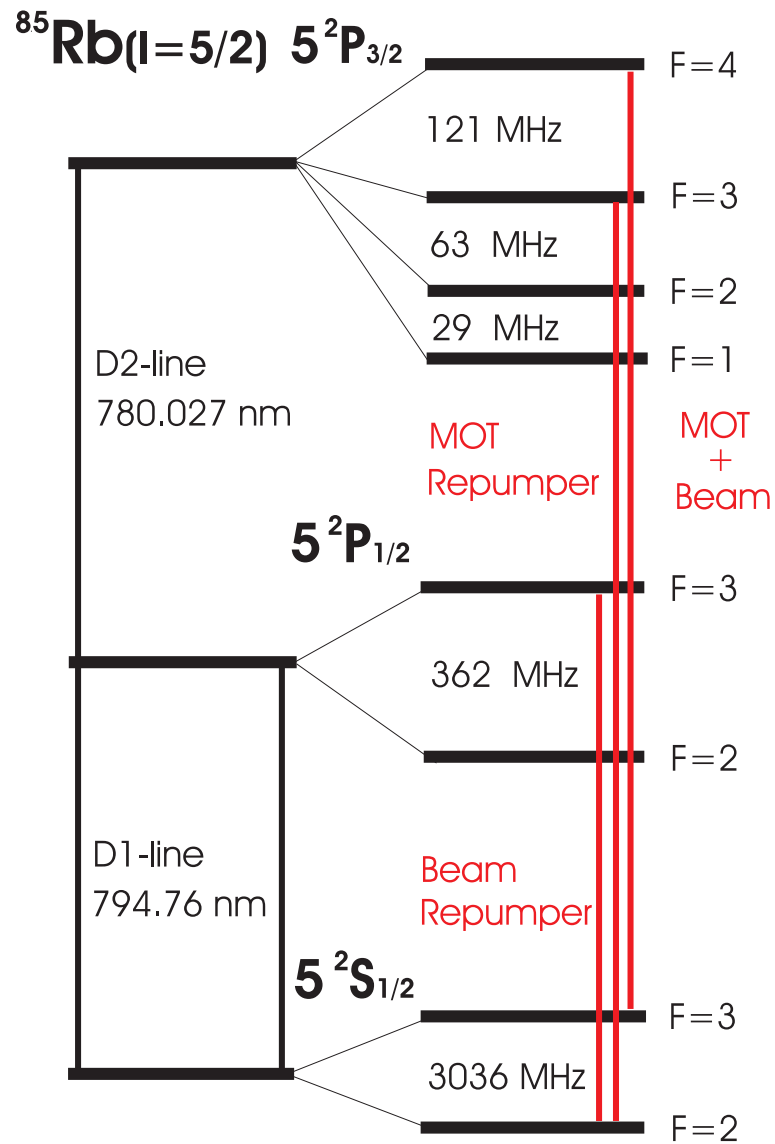


Figure 4.2: Energy Levels of ^{85}Rb . The ground state consists of two hyperfine states with $F=2$ and $F=3$. The cooling transition for the MOT and beam cooling is $5^2\text{S}_{1/2}(F=3) \rightarrow 5^2\text{P}_{3/2}(F=4)$ of the D2-line. The repumping laser for the MOT drives the $5^2\text{S}_{1/2}(F=2) \rightarrow 5^2\text{P}_{3/2}(F=3)$ transition of the D2-line. The repumper for the beam cooling is tuned to the $5^2\text{S}_{1/2}(F=2) \rightarrow 5^2\text{P}_{1/2}(F=3)$ transition of the D1-line. All wavelengths are given as values in air.

Doppler shift is twice the Zeeman shift at the capture radius: $kv_{max} = 2bR_C = 2\delta$, can be trapped in the MOT. Where $b = dB/dz$ and δ being the detuning from the resonance. Using the rubidium transition and assuming the experimental values of $\omega_1 = 3.5\Gamma$ and $\delta = 1.5\Gamma$ we get $R_C = 18.8\text{ G}/b$ with b in Gauss/cm. With the magnetic field gradient of $15\text{ G}/\text{cm}$ we find $R_C = 1.25\text{ cm}$. The capture velocity is calculated to be $v_C = 6.6\text{ m}/\text{s}$. At room temperature, the middle velocity of rubidium atoms is $v = \sqrt{kT/M} = 170\text{ m}/\text{s}$, so only a small part of atoms ($\sim 8 \cdot 10^{-6}$) can be trapped by the MOT. At this point, one has to mention the two alternatives for loading the MOT: loading from a *vapor* and loading from a cooled *atomic beam*.

4.3 Loading Schemes for MOTs

In the first realization of a MOT [59], a cold atomic beam was used as a source of atoms for loading the trap. Later, it was demonstrated that atoms could be directly captured in a MOT from a low-pressure vapor [53]. Each of these loading schemes has pros and cons, which we will briefly discuss now.

Let us begin with the atomic beam loading configuration. To efficiently cool down the atoms in an atomic beam, it is necessary to maintain the resonance condition for the atoms on the entire way from the oven to the trap region. This can be realized by shifting the atomic resonance with a magnetic field (Zeeman cooling technique [56]), or by shifting the frequency of the cooling laser (chirped laser technique [3, 26]). A Zeeman slower decelerates an intense thermal atomic beam along the propagation axis of the beam by the radiation pressure, while the spontaneous emission processes give rise to a transverse heating of the atoms. This results in a strongly diverging beam with a flux of up to 10^{11} at/s. This loading method has following benefits: most of the atoms in the atomic beam can be decelerated and, thus, can be captured in the MOT; the vacuum in the MOT region is not significantly influenced by the atomic beam source, since the Zeeman slower acts as a differential pumping route between oven and MOT region². The drawback of the beam method consists in the complexity of the set-up, that requires a Zeeman section, an oven and collimating sections, and an additional laser with sufficient power to saturate the atomic transition. The main disadvantage of this method is that atoms are loaded from a very small spatial angle (typically $3 \cdot 10^{-4}$), resulting in relatively small loading rate (small number of atoms, but almost all of them are cold enough to be trapped in a MOT). The divergence of the beam imposes geometrical constraints on the arrangement of the Zeeman slower's output and the trapping volume of the MOT. The slowing light on axis or the magnetic fields involved, can disturb the successive MOT.

Alternatively, a MOT can be easily load from a low-pressure vapor. At this point one has to mention that this method is only effective in the case of earth-alkali elements, because of their high vapor pressure at room temperature, see for Rb the Tab. B.4 in the Appendix B. Along with the obvious advantages of this method, concerning the simplicity

²For rubidium, the slower length should be about 80 cm, and with the inner diameter of a slower tube of typically 1 cm (a good compromise between beam collimation factor and the current in the Zeeman magnet, providing the required magnetic field on the beam axis), a pressure difference of two order of magnitude can be established between oven and the main chamber.

of the experimental set-up by elimination of a precooling stage, such as Zeeman slower or frequency-chirped lasers, and loading from the whole spatial angle of 4π , there exist several drawbacks, namely: only small amount of atoms from the vapor (approx. 10^{-6}) can be trapped by MOT; background vapor is a source of energetic atoms hitting and ejecting those atoms, already trapped in a MOT. These background collisions limit the trap-confinement time and consequently the total number of atoms trapped in a MOT. In most experiments it is desirable to have a large number of atoms for as long as possible in a trap, for example in order to support evaporative cooling, a critical step in the production of a BEC.

In our experiment we try to combine the advantages of these two different loading schemes. That means, an enhanced spatial angle for loading (as in a vapor method) together with the better vacuum conditions (as in a beam method).

4.4 Our Magneto-Optical Trap

Our setup uses a pre-cooled thermal atomic beam for loading the magneto-optical trap. The beam geometry is designed in a way to maximize the loading rate of the MOT. Beam collimation is realized with a multichannel plate (see Sec. 2.1.1), providing an exit surface of 25 mm in diameter and collimation factor of 30. With a distance of 40 cm between collimator and MOT region all these parameters provide relatively high spatial angle of $2 \cdot 10^{-2}$ for loading atoms into the MOT, in comparison to the typical spatial angle of $5 \cdot 10^{-6}$ provided by a Zeeman decelerator.

Since the magnetic coils of our MOT have a radius of 10.5 cm, we can use the magnetic field ramp for additional deceleration of the thermal atomic beam.

4.4.1 Atomic Beam and Beam Deceleration

We will shortly review the essential points of beam physics. The Maxwell-Boltzmann velocity distribution of atoms in a gas is given as

$$f(v) = \left(\frac{m}{2\pi k_B T}\right)^{3/2} \exp\left(-\frac{mv^2}{2k_B T}\right) = \left(\frac{1}{\pi v_0^2}\right)^{3/2} \exp\left(-\frac{v^2}{v_0^2}\right) \quad (4.9)$$

where $v_0 = \sqrt{2k_B T/m}$ is the most probable velocity. In the atomic beam, the velocity distribution has a form:

$$f_B(v) = \frac{2}{v_0} \left(\frac{v}{v_0}\right)^3 \exp\left(-\frac{v^2}{v_0^2}\right) \quad (4.10)$$

and the mean velocity in the beam is given as

$$\bar{v} = \int_0^\infty v f_B(v) dv = \frac{3}{4} \sqrt{\pi} v_0 \quad (4.11)$$

The fraction of atoms in the beam below a certain velocity v_c , is given by

$$\int_0^{v_c} f_B(v) dv = 1 - \left(1 + \left(\frac{v_c}{v_0}\right)^2\right) \exp\left(-\frac{v_c^2}{v_0^2}\right) \Big|_{v_c \ll \bar{v}} \simeq \left(\frac{v_c}{v_0}\right)^4 \quad (4.12)$$

The rate of atoms, transmitted through a channel of radius r and length l can be calculated as

$$Q = n \frac{A}{2} 2\pi \int_0^\infty f(v) v^3 dv \int_0^{\theta_m} \sin \theta d\theta \quad (4.13)$$

$$= n \frac{A}{2} 2\pi \frac{v_0}{2\pi^{3/2}} \int_0^\infty f_B(v) dv \int_0^{\theta_m} \sin \theta d\theta \quad (4.14)$$

$$\cong A \frac{v_0}{2\sqrt{\pi}} \frac{1}{2} \left(\frac{r}{l}\right)^2 = \frac{nAv_0}{4\sqrt{\pi}} \left(\frac{r}{l}\right)^2 \quad (4.15)$$

where $n = p/k_bT$ is the atomic density. The total rate of atoms reaching the MOT volume can be estimated by the summation over all channels (in our case 324). With $r = 0.4 \text{ mm}$, $l = 24 \text{ mm}$, $n = 1.14 \cdot 10^{20} \text{ at/m}^3$ (Rb vapor pressure at 150°C is $p = 0.665 \text{ Pa}$, see Tab. B.4) one can easily obtain the total flux of $Q = 2 \cdot 10^{13} \text{ at/s}$.

The Eq. 4.12 shows strong dependency of the loading rate, i.e. flux of atoms with velocities below v_c , on the capture velocity of the MOT. The MOT capture velocity can be extended by increasing the detuning of the MOT capture beam. In our case, we set the detuning to 2.5Γ , which results in $w_1 = 4.5\Gamma$, $s = 1.8$, and $v_c = 11.78 \text{ m/c}$. This means that only each 380 000-th atoms can be trapped in the MOT. To increase the flux of slow atoms we use the scheme of beam deceleration: a laser beam is counterpropagating to the atomic beam and the resonance condition during the deceleration is maintained by varying magnetic field produced by the MOT coils.

The velocity of a decelerated atom changes as: $v = v_i - at$, where v_i is the initial velocity and a the constant deceleration. The distance travelled by an atom is given as: $s(t) = v_i t - \frac{1}{2} at^2$. Summing up the above relations and assuming $s_i = v_i^2/2a$, one easily obtains:

$$\frac{v}{v_i} = \left(1 - \frac{s}{s_i}\right)^{1/2} \quad (4.16)$$

When atoms are decelerating, they are tuned out of resonance with the slowing laser. To compensate this Doppler effect one can chirp the laser frequency or change the transition frequency within the atoms using the Zeeman effect. Magnetic field will shift both levels of the cooling transition, therefore the difference in these shifts has to cancel the Doppler shift at every moment during the slowing process:

$$kv = \Delta g \Delta m \frac{\mu_B}{\hbar} B \quad (4.17)$$

where μ_B is the Bohr magneton, and B the magnetic field. For the $^{85}\text{Rb } 5^2S_{1/2}(F = 3, m_F = 3) \rightarrow 5^2P_{3/2}(F = 4, m_F = 4)$ cooling transition, the factor $\Delta g \Delta m = 1$, see Tab B.5. As in the case of MOT, a repumper laser beam should be added to the cooling beam in order to close the cooling cycle. Though, the $\Delta g \Delta m$ -factor for a repumper transition should have the same value as for the cooling transition. The proper transition can be found on the D 1-line: $5^2S_{1/2}(F = 2, m_F = 2) \rightarrow 5^2P_{1/2}(F = 3, m_F = 3)$.

The magnetic field should be tailored in space in such a way, that all decelerating atoms always experience the suitable magnetic field along the direction of propagation. This can

be realized if the magnetic field shows the same dependence on slowing distance as the velocity in Eq. 4.16, namely:

$$B(x) = B_{max} \sqrt{1 - x/x_i} \quad (4.18)$$

with $B_{max} = \frac{\hbar k v_i}{\mu_B}$ being the initial magnetic field. The frequency shift due to the magnetic field is given by $\delta\omega = \pm \frac{\mu_B}{\hbar} B = 1.4 \frac{GHz}{G} B$, where $+$ ($-$) is valid for σ_+ (σ_-) light.

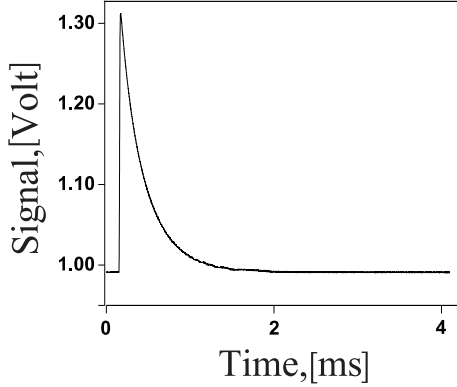


Figure 4.3: Shut-down measurement of the MOT magnetic field. The signal is measured with a "pick-up" coil.

In the case of quadrupole magnetic field of the MOT, the field gradient b is linear and the spatial dependence of the magnetic field has the form: $B = bx$. With the same gradient at the beginning of the deceleration, the linearly decaying magnetic field needs double distance to reach zero value in comparison to the optimal tailored magnetic field of Zeeman slower according to Eq. 4.16. In Fig. 4.4, the comparison of the spatial dependencies of Zeeman slower field (square-root tailored, in red) and MOT field (linear decaying, in black) are shown. For the deceleration procedure this means that in a quadrupole magnetic field, atoms need double distance to be stopped as compared to the situation in the Zeeman slower.

4.4.2 Magnetic Coils

As previously mentioned, a suitable magnetic field is needed for the MOT operation. It is created by two magnetic coils arranged in a so-called anti-Helmholtz configuration, i.e. the spacing between coils is equal to the coil's diameter, and the electric current in the coils is counterpropagating. The magneto-optical trap is located in the center between the coils, where magnetic field vanished. From the trap center outwards, the field is increasing homogeneously and linearly. The field gradient is not isotropic, in the vertical direction (coils axis) it is twice as large as in the horizontal plane:

$$\left. \frac{dB}{dz} \right|_{z=0} = -\frac{3\mu_0 IN}{2} \cdot \frac{R^2 L}{\left(R^2 + (L/2)^2\right)^{5/2}} \quad (4.19)$$

where L is the separation of the two coils, R is the coil radius, N is the number of turns in one coil, I electric current, and $\mu_0 = 1.2566 \cdot 10^{-6} Vs/Am$ the magnetic constant. For our setup, $L=1.12R$, and with $R=10.5$ cm, $N=120$ turns, $I=10A$, the gradient in the trap center is set to 11.6 G/cm. Each magnetic coil is made of copper wire of 2 mm diameter wrapped on the U-form aluminium ring. The rings are cut in the axial plane to avoid the building of ring currents. These currents can dramatically increase the inductance of coils,

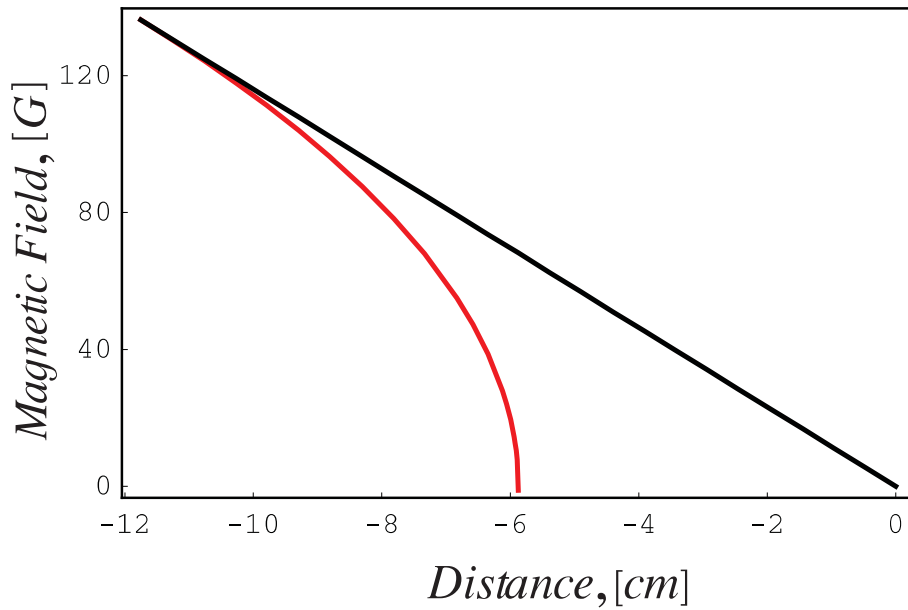


Figure 4.4: *Spatial dependence of the Zeeman slower magnetic field (in red) and quadrupole magnetic field of MOT (in black). The gradients on the beginning of deceleration (at $B_{max} = 136\text{ G}$) are equal for both fields. Decay distance of the linearly dependent field is twice as large as of the optimal tailored field from Eq. 4.16*

and thus the switch-off time for the magnetic field. For our setup, this effect is enhanced through the vacuum chamber body, since the magnetic coils are positioned outside the chamber.

The inductance of each magnetic coil is measured to 3 mH, which is consistent with the calculations, based on the geometrical parameters of the coils. The complete shut-down process of the magnetic field in the coils, mounted on the chamber, take less than 2 ms for a typical MOT magnetic field ($I=10\text{ A}$). To obtain the decay time of MOT magnetic field, we measure the induced voltage in a "pick-up" coil, positioned coaxial with one of the MOT coils. The result of such measurement is shown in Fig. 4.3.

To provide a heat dissipation, each coil has a water cooled ring, which is implemented in the coil body. At the typical current of 10 A, about 55 W has be dissipated in each coil.

4.4.3 Optical Setup for MOT

As mentioned in Sec. 4.1, three pairs of laser beams with $\sigma_+ - \sigma_-$ polarizations are required to construct a MOT. The simplest way is to reflect the laser beams back after they passed through the MOT region. This scheme has one drawback: due to the absorption, the reflected laser beam is weaker than the forthcoming one. Thus, radiation pressure is imbalanced. This results in the shift of trapped cloud out of the MOT center (place where magnetic field is zero). If the MOT beams are used as "flash-light" during the detection, the imbalance of the radiation pressure cause an acceleration of atoms and thus can distort the experimental results. We choose the six-beam design of the MOT. Combining six independent laser beams along three spatial directions allows us to precisely adjust the

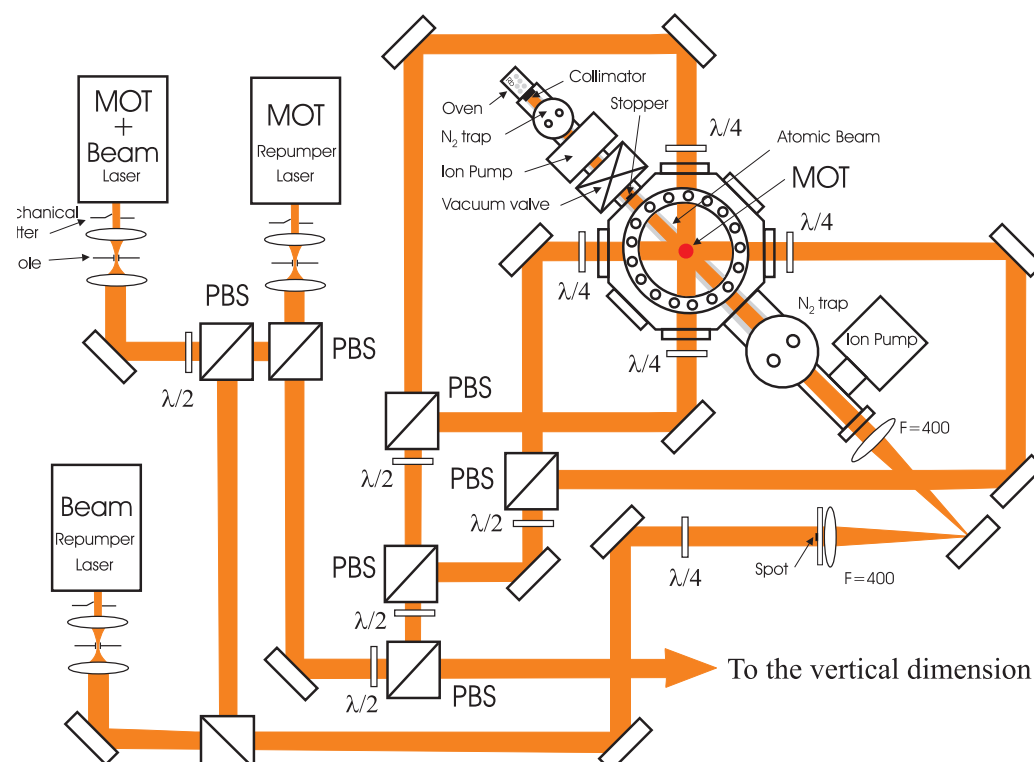


Figure 4.5: Optical scheme of our MOT setup, including atomic beam cooling scheme. PBS-polarizing beamsplitter.

power balance between laser beams, and, hence, the radiation pressure inside the MOT. This scheme needs twice as large laser power as the scheme with the retroreflected beams.

The optical scheme of our MOT setup is depicted in Fig. 4.5, where the two-dimensional view of the setup is shown. Three diode laser systems serve as light sources for the MOT and beam cooling. All laser systems are protected through Faraday isolators against optical feedback. The radiation for the cooling transition for the MOT and beam deceleration is produced by MOPA laser system (see Sec. 3.2.1). Total output power of this system can reach up to 220 mW, which is quite enough to drive the cooling transition above the saturation, even with a quite large diameter of the light beams (25mm). The repumping laser systems are grating stabilized diode lasers (see Sec. 3.2.1). We use in our experiments two separate laser systems, since the wavelengths for MOT and beam repumper are different (see Sec. 4.4.1 and 4.1). All laser beams can be separately shut off by mechanical shutters (Densitron, see Appendix E.2) placed in the middle of a 1:1 telescopes. The shut off time is measured to 100 μ s.

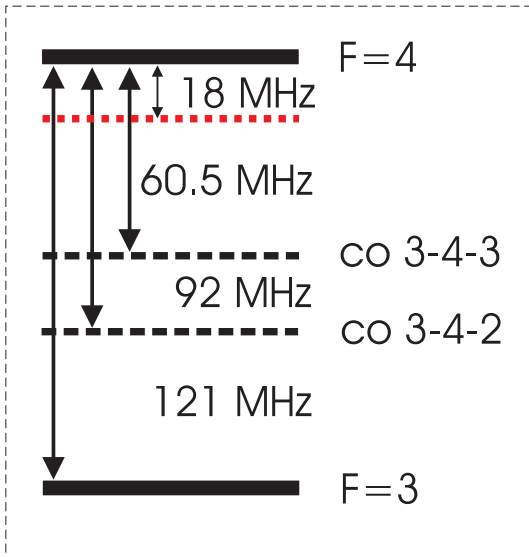


Figure 4.6: *Detuning scheme for the MOT. Red dotted line marks the detuning of our MOT from the atomic resonance. Using an AOM at 76 MHz we can stabilize the laser frequency to the 3-4-2 crossover.*

light beam from each laser system is mode filtered with a pinhole and expanded to the diameter of MOT beams. The power balance between the dimensions and inside each dimension of the MOT optical setup is set with the help of $\lambda/2$ retardation plates and polarizing beam splitters, see Fig. 4.5. The cooling and repumper laser beams for atomic beam deceleration are also combined together on the polarizing beam splitter and injected into the vacuum chamber through a rear window. This combined laser beam is slightly focused to compensate the divergence of the counterpropagating atomic beam. To avoid the influence of the unbalanced radiation pressure on the trapped atoms, we project a spot

An acousto-optical modulator is placed inside the MOPA laser system between master laser and the amplifier, see Fig. 3.8. This modulator allows us to tune the frequency of the laser system in the range of about 40 MHz and to regulate the output power of the system by varying the power of the controlling radiowave signal. To reach the optimal settings for the cooling, we set the detuning of the AOM to 76 MHz, so that we can stabilize the laser system to the 3-4-2 crossover on the ^{85}Rb spectrum (see Fig. 3.5, and 4.6), which has a detuning of 92 MHz from the $F = 3 \rightarrow F' = 4$ cooling transition, so that we can end up with a red detuning of 2.5Γ to the cooling transition. The slope of the error signal in the vicinity of 3-4-2 crossover signal is steeper and larger in the amplitude as compared to other transitions (see Fig. 3.6), so that stabilizing to it provides more reliable and frequency stable output.

The light beams from cooling and repumper laser systems are combined together on the polarizing beam splitter. Before being mixed, the

of 4 mm diameter into the area of MOT via a 2-f image system, see Fig. 4.5. To avoid an influence of the atomic beam on the trapped atoms, we blocked the central part of atomic beam with the stopper ($\varnothing=4$ mm), which is installed inside the vacuum chamber.

4.4.4 Parameters of the MOT

The magneto-optical trap is characterized by three main parameters: number of trapped atoms, atomic density and the lifetime of atoms in the trap. The number of atoms and atomic density can be obtained through the fluorescence from a trapped atomic sample. The power P_Ω , detected by a photo diode (or CCD camera) from a solid angle Ω is proportional to the number of scattered photons, and hence to the number of trapped atoms N :

$$P_\Omega = N \frac{\Omega}{4\pi} \hbar\omega \Gamma_{sc} \quad (4.20)$$

where ω is the atomic resonance frequency and Γ_{sc} denotes the photon scattering rate, which is given for a two-level atom as: $\Gamma/2 (s/(1+s))$. In the case of ^{85}Rb we can assume that all 7 Zeeman sublevels are uniformly occupied, so that the saturation parameter s should be multiplied with the correction factor $\kappa = 3/7 \approx 0.43$. Taking in account $s = s_0/(1 + (2\delta/\Gamma)^2)$, where $s_0 = I/I_0 = 2\omega_1^2/\Gamma^2$ is the resonant saturation parameter, we can express the number of trapped atoms as:

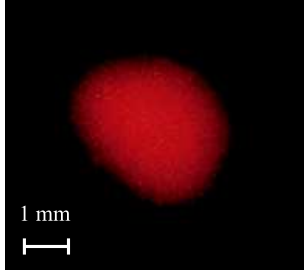


Figure 4.7: Atomic cloud in the MOT.

$$N = P_\Omega \frac{4\pi}{\Omega} \frac{\lambda}{2\pi\hbar c} \frac{2(1 + \kappa s_0 + (2\delta/\Gamma)^2)}{\kappa s_0 \Gamma} \quad (4.21)$$

with λ being the atomic wavelength and c the light velocity. We register the power scattered light with a calibrated CCD camera system, see Appendix E.2. Taking in account parameters of the CCD camera and using Eq. 4.21, we obtain the number of trapped atoms $N = 3.9 \cdot 10^9$ for the experimental parameters $s_0 \simeq 8$ and $\delta \simeq 2.5\Gamma$. From the images, captured with the camera system we can obtain the extension of the atomic sample in the trap and, hence the density of atoms, which was measured to be $\rho = 5 \cdot 10^{10} \text{ at/cm}^3$. A typical picture of atomic sample trapped in the MOT is shown in Fig. 4.7.

The time evolution of trapped atoms provides information on the vacuum conditions and two-body collisions that occur at high atomic densities. The result of a lifetime measurement is depicted in Fig. 4.8. Decay of the atomic sample is properly described by³:

$$N(t) = N_0 \frac{(1 - \xi)e^{-t/\tau}}{1 - \xi e^{-t/\tau}} \quad (4.22)$$

where τ is the exponential decay time due to collisions with background gas and parameter $\xi = \beta n_0/(\beta n_0 + \sqrt{8}/\tau)$ describes the losses due to two-body collisions (β is the two-body collision rate, n_0 the atomic density). From the data in Fig. 4.8 we deduced: $\tau = 7.9 \text{ s}$ and $\xi = 0.072$. The exponential decay time $\tau = 7.9 \text{ s}$ shows that the vacuum conditions

³The derivation of Eq. 4.22 is described in C

and, hence the background gases collision rate, are quite small and will not disturb our experimental investigations. From the trap loss parameter ξ one can deduce the two-body collision rate, which is in our case $\beta \sim 5 \cdot 10^{-12} \text{ cm}^3/\text{s}$. Similar values were observed in other experiments [29], where the trap losses were studied in a wide range of experimental parameters. A good overview on the collision losses can be found in [79].

To study the influence of the additional trap load rate, originating from the deceleration of the atomic beam, we measure the density and number of atoms in the MOT in two regimes: with additional cooling and without it. It turns out that deceleration of the loading atomic beam increases the number of trapped atoms by a factor of 2, but the density decreases by a factor of 0.8. This is in a reasonable agreement with the results of detailed study of density dependence in the MOT on the number of trapped atoms [45, 71]. Namely, in the "optical density" regime, increase in the number of atoms brings decrease of the atomic density. Typical values for our MOT without additional beam cooling were: $N \sim 1.8 \cdot 10^9 \text{ at}$ and $n \sim 8.5 \cdot 10^{10} \text{ at}/\text{cm}^3$.

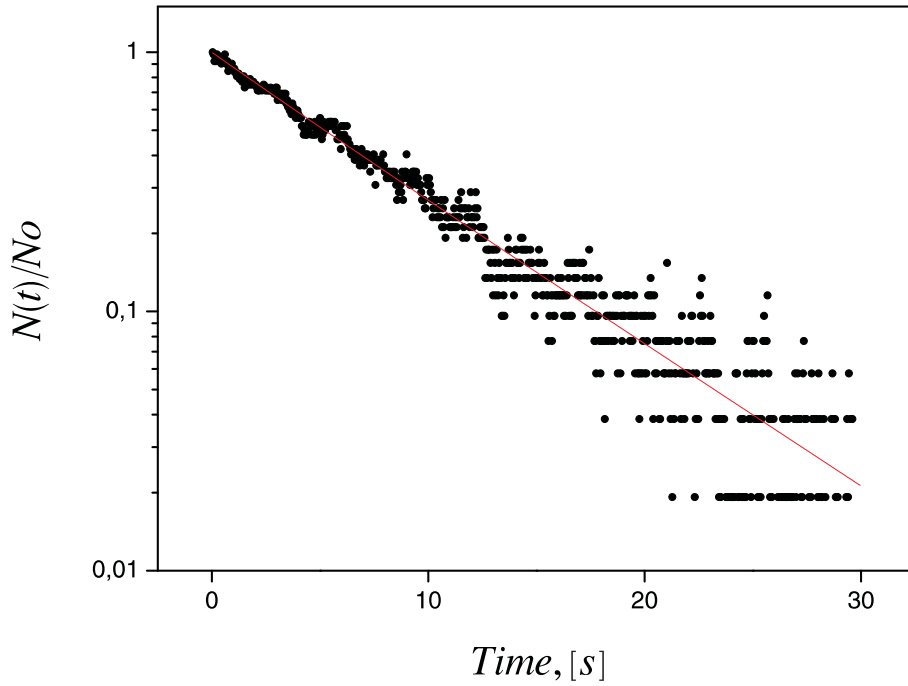


Figure 4.8: Decay of the MOT. The red line is a fit with $\tau = 7.94 \text{ s}$ and the decay parameter due to inelastic collisions $\xi = 0.072$, see Appendix C.

Chapter 5

2D and 3D Dark Optical Lattices

This chapter presents our experimental results on dark optical lattices. We begin with a brief review of basic properties of conventional optical lattices (Section 5.1). In Section 5.2 we give a short description of the physics of dark optical lattices and present our implementation of a two-dimensional dark optical lattice (2D DOL). We characterize the 2D DOL with respect to the lifetime, the temperature, and the fundamental vibrational frequency measured by means of stimulated Raman spectroscopy. We demonstrate the reduced fluorescence level of this type of optical lattices. Finally, the novel 3D configuration for dark optical lattice is described and its ability to trap and cool atoms in three dimensions is presented in Section 5.3.

5.1 Conventional (Bright) Optical Lattices

5.1.1 One-Dimensional Optical Lattices

The first experimentally observed optical lattice had the same geometry of electrical fields as a 1 D *lin* \perp *lin* molasses configuration leading to Sisyphus cooling, for details see Sec 1.3.1. This field configuration provides not only localization and quantization of the atomic motion inside optical-potential wells, but also the cooling, which is necessary to have a large fraction of the atoms in the lowest vibrational levels of the potential wells.

Sisyphus Cooling and Quantization of the Atomic Motion

Consider an atom with a $F = 1/2 \rightarrow F' = 3/2$ transition (see Fig. 5.1) placed in a light field composed of two counterpropagating laser beams with frequencies ω , field amplitudes E_0 , having orthogonal polarizations \vec{e}_x and \vec{e}_y (Fig. 5.2).

$$\vec{E}_1 = \frac{E_0}{2} \vec{e}_x (\exp^{i(kz - \omega t)} + c.c.) \quad (5.1)$$

$$\vec{E}_2 = \frac{E_0}{2} \vec{e}_y (\exp^{i(kz - \omega t)} + c.c.) \quad (5.2)$$

The resultant electric field:

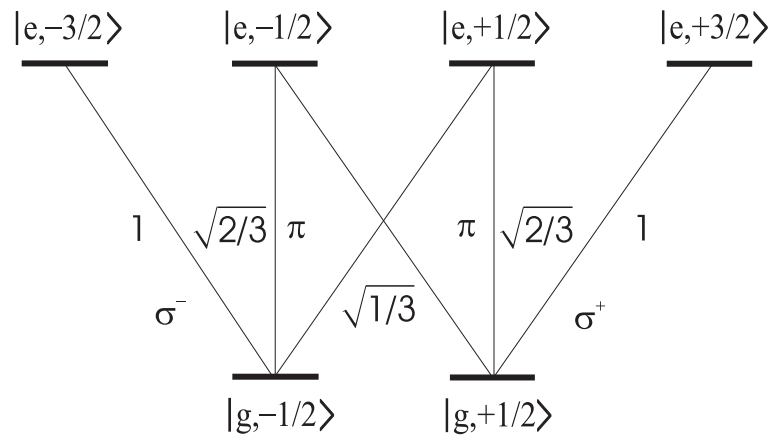


Figure 5.1: Level scheme and Clebsh-Gordan coefficients for the $F = 1/2 \rightarrow F' = 3/2$ transition.

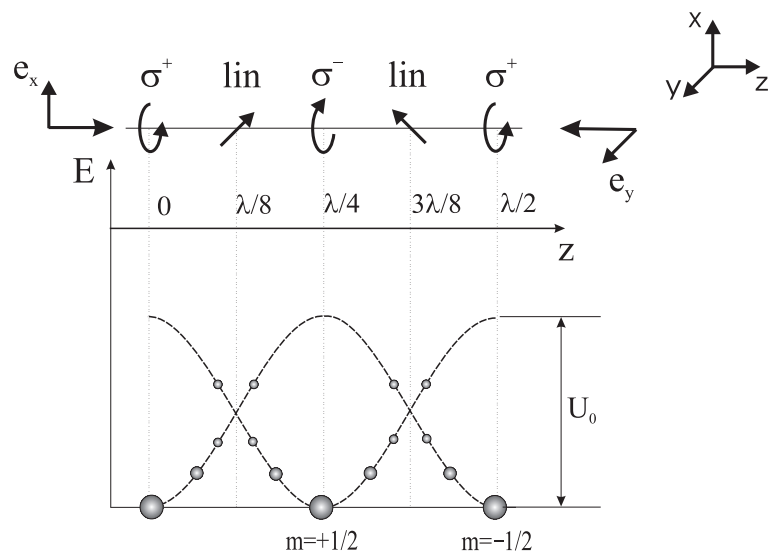


Figure 5.2: Above: $\text{lin} \perp \text{lin}$ configuration consists of two counterpropagating laser beams with same frequency and orthogonal linear polarization. The resultant field exhibits a polarization gradient with a $\lambda/2$ periodicity. Below: Light shifts for a $F = 1/2 \rightarrow F' = 3/2$ transition. The spatial dependence of light shifts is due to the polarization gradient. The light shift is maximal at the points of pure circularly polarization.

$$\vec{E}_z = (E_+ \vec{e}_+ + E_- \vec{e}_-) \exp^{-i\omega t} + c.c. , \quad (5.3)$$

exhibiting a polarization gradient, shown in Fig. 5.2, with:

$$\vec{E}_+ = -i \frac{E_0}{2} \sqrt{2} \sin(kz) \quad (5.4)$$

$$\vec{E}_- = \frac{E_0}{2} \sqrt{2} \cos(kz) \quad (5.5)$$

$$\vec{e}_\pm = \mp \frac{\vec{e}_x \pm i \vec{e}_y}{\sqrt{2}} \quad (5.6)$$

Equation 5.3 shows, that the total field can be decomposed into two standing waves of σ_+ and σ_- polarization with an offset of $\lambda/4$ to each other (so that antinodes of one standing wave coincides with the nodes of another). The light intensity $I_L \propto |E_z|^2$ is everywhere constant, only the field polarization changes from circular to linear and back to circular as one moves a distance $\lambda/4$ along the z-axes.

Let us take a look on the dynamics of an atom interacting with such a field. At the points where the light is circularly polarized, the optical pumping transfers all available atoms into sublevels with $m_g = 1/2$ in the case of σ_+ polarization, or in $m_g = -1/2$ in the case of σ_- polarization, see Fig. 5.2. The spatial correlation of optical pumping and light shifts provides the basis for the Sisyphus cooling mechanism, see Sec. 1.3.1. The atoms loose their kinetic energy and become localized in the vicinity of the potential minima.

The maximum light shift, and hence, the deepest optical-potential well, arises at the positions where the light is circularly polarized because the Glebsh-Gordan coefficient for a transition $m_g = F \rightarrow m_e = F + 1$ (or $m_g = -F \rightarrow m_e = -(F + 1)$) is equal to 1. Moreover, at these points the most light-shifted sublevel is the only one populated by optical pumping. The typical depth of the potential wells is on the order of the maximum light-shift $\Delta \approx \omega_1^2/4\delta$, where ω_1 is the resonant Rabi frequency for a transition with a Clebsh-Gordan coefficient equal to 1.

In the limit of low saturation , the optical potentials for the ground states $|g, \pm \frac{1}{2}\rangle$ are:

$$U_+ = \frac{U_0}{3}(2 + \cos 2kz), U_- = \frac{U_0}{3}(2 - \cos 2kz) \quad (5.7)$$

where $U_0 = \hbar \delta s/2$ is the maximum value of the light shift potential and $s = 2\omega_1/(4\delta^2 + \Gamma^2)$ is the saturation parameter with associated Rabi frequency $\omega_1 = -dE_0/\hbar$ (d is the dipole moment for the transition with Clebsh-Gordan coefficient equal to 1), Γ is a natural width of the upper level and $\delta = \omega - \omega_A < 0$ is the detuning of the lattice from the atomic resonance. For atoms located in the bottom of a well, the potential is nearly harmonic so for small z we can approximate it as

$$U_- \cong \frac{3}{2}U_0 + k^2 z^2 \quad (5.8)$$

from $U_0 k^2 z^2 = \frac{1}{2} M \omega_{vib}^2 z^2$ and using $E_{rec} = \frac{\hbar^2 k^2}{2M}$, we get the oscillation frequency of an atom:

$$\omega_{vib} = \frac{2\sqrt{E_r U_0}}{\hbar} \quad (5.9)$$

According to the semiclassical model of Sisyphus cooling [20], the minimum temperature achieved in the cooling process scales with the depth of the potential wells U which in principle can be made arbitrary small. When the temperature approaches the recoil limit $k_B T = E_{rec}$, the atomic de Broglie wavelength becomes comparable with the optical wavelength and thus comparable to the width of the optical-potential wells involved in the cooling mechanism. In this regime it is no longer justified to treat the atomic external degrees of freedom classically. However, before one gets close to E_{rec} by approaching low values of U , another limitation of this model arises. As a necessary condition our resulting steady-state temperature should correspond to a mean velocity $v_{rms} = \sqrt{U/M}$ smaller than the capture velocity $v_{cap} = \Gamma_p/k$. This condition can be reformulated as $\omega_{vib}\tau_p$ which indicates that the semiclassical model works as long as the time for a vibrational period $1/\omega_{vib}$ of an atom inside the potential well of depth U is longer than the optical-pumping time. When U tends to zero, $\omega_{vib}\tau_p$ increases and will eventually exceed $\sqrt{2}$. At this point the atomic velocities will exceed the capture velocity v_{cap} and the friction coefficient will start to decrease below the value predicted in Eq. 1.20. Long before U gets even close to the recoil energy, the system enters the regime where between successive optical pumping cycles the atom will oscillate many times in its potential well.

Localized Atoms: the Lamb-Dicke Regime

A quantum treatment of atomic motion is necessary if U is close to the recoil energy. Similarly to the situation of an electronic gas in a solid, a band model with discrete allowed energy bands separated by band gaps is employed. In the experiments, the depth of the potential wells is typically on the order of a few MHz , while the typical band gap at the bottom of the potential wells is on the order of few hundred kHz . The recoil temperature corresponds to a few kHz showing that at such low temperatures one may expect only a few of the lowest states in the optical potential to be populated. due to the extremely small tunnelling rates for these low-lying states [12], one may treat each potential well as completely independent and thus may apply a harmonic-oscillator model.

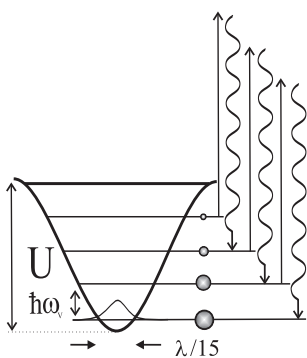


Figure 5.3: Harmonic-oscillator model for an optical lattice. The populations of vibrational levels are indicated with circles.

In this picture, the cooling arises due to spontaneous Raman transitions between different vibrational states as depicted in Fig. 5.3. The relaxation rates Γ_n of the low-lying vibrational levels via such Raman transitions are proportional to the vibrational quantum number n and the optical-pumping rate Γ_p for a free atom multiplied by a small factor $\eta = E_{rec}/E_{vib}$ (called Lamb-Dicke factor, which reflects that the extension of the wave function of an atom localized in an optical lattice is much smaller than the wavelength of light, see Fig. 5.3), i.e. $\Gamma_n \approx (2n + 1)\eta\Gamma_p$. Here, $E_{vib} = \hbar\omega_{vib}$ is the energy separation between adjacent vibrational states. The factor $(2n + 1)\eta$ plays a similar role as the Franck-Condon factor in molecular physics. The spatial confinement of the atomic centre-of-mass wave functions increases with decreasing n : the wave functions of well-confined levels have little overlap with those of any other level. The steady-state populations of vibrational levels decrease strongly with increasing vibrational

number. Besides inelastic transitions which change the vibrational quantum number and lead to cooling, there are also elastic transitions leading back to the initial vibrational level. These transitions are clearly not suppressed by the Lamb-Dicke effect and thus occur at a rate Γ_p . For this reason, red-detuned optical lattices on a $F \rightarrow F' = F + 1$ atomic transition are called bright optical lattices. As a consequence the fluorescence spectrum consists mainly of an elastic component arising at the frequency of the trapping field and much smaller vibrational sidebands symmetrically grouped around the elastic peak due to Stokes or anti-Stokes processes. As the calculations shows [69],[17], the fraction of atoms in the lowest state can be quite large - more than 30% and is a growing function of F . Due to this and the fact that the vibrational ground state can only contribute to Stokes processes, the Stokes component of the vibrational sidebands is larger than its anti-Stokes counterpart [43].

5.1.2 Multi-Dimensional Optical Lattices

To realize a two-dimensional (2D) optical lattice it is necessary to create points in space with pure σ_+ and σ_- polarization of light. Two intersecting standing waves with crossed linear polarizations were used [39] to construct such 2D light fields, see Fig. 5.4.

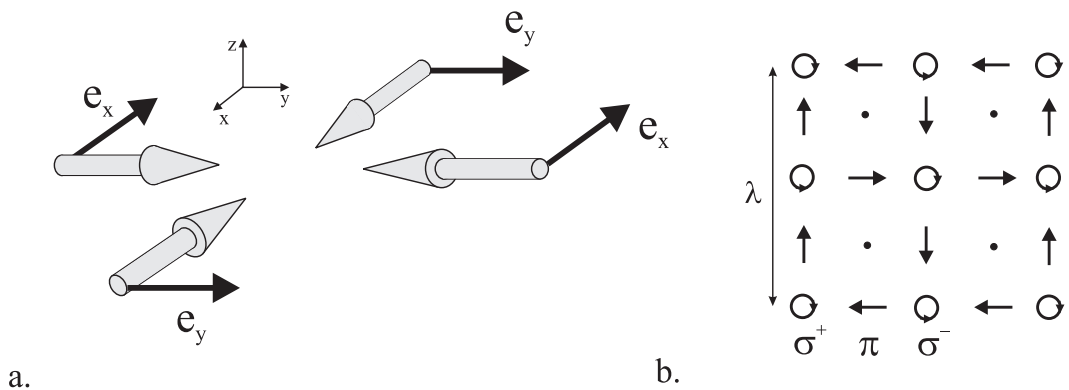


Figure 5.4: *Light field topography of 2D optical lattice. a) The light field is created using four linear polarized laser beams. b) The resulting polarization pattern with $\psi = 90^\circ$.*

In a 1D optical lattice, the fluctuations in the relative phase between the two forming beams result only in a translation of the lattice. The topology of the lattice remains constant. A translation of the lattice has little influence on the atoms, since the timescale for the atomic dynamics is short compared with the phase fluctuation time. Constructing a 2D lattice with four laser beams it is necessary to control the relative phase ψ between the standing waves formed along the x and y -axes as depicted in Fig. 5.4. A pattern with alternating σ_+ and σ_- wells is obtained with $\psi = 90^\circ$.

Another way to create the required polarization pattern is to use only three laser beams as is shown in Fig. 5.5. In this configuration is not necessary to control the relative phase [34]. Generally, for a space with n dimensions it is possible to construct a "phase-stable" polarization pattern using $n + 1$ light fields, for details see [34]. Comparing these two ways of creating a multidimensional lattice, on the one hand, we have the

simplicity of experimental realization (in the case of three-beam configuration), but on the other hand, using four-beam configuration we can easily change the topology of the total field. Moreover, in the case of dark optical lattices, the four beam configuration seems

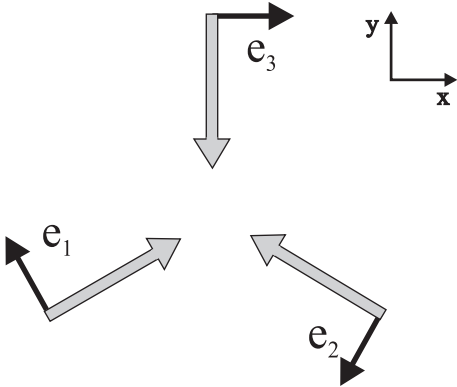


Figure 5.5: Configuration with minimum number of beams. Three coplanar beams making an angle of 120° with each other and polarized in their plane of propagation.

multiple scattering of light [45]. The other limiting factor is the lattice itself, where the retro-action of the atoms upon the light field modifies the potential wells in a way that disturbs cooling and trapping mechanisms. The lattice geometry can be modified by mutual interatomic interactions [66] or by the backaction of the induced atomic polarization on the lattice field [40].

A method to overcome these limitations in bright optical lattices is to design a lattice that makes use of dark states - states in which atoms only interact weakly with the light field. In such optical lattices, also called dark optical lattices, the atoms are bound at the locations where, due to selection rules, they are practically decoupled from the light field.

5.2 Bichromatic Dark Optical Lattice

5.2.1 1D Dark Optical Lattice

Dark Optical Molasses

In this subsection we examine the implementation of a blue-detuned light field with appropriate polarization gradient in order to obtain Sisyphus cooling into dark states. The result is a modified optical molasses with reduced fluorescence level where atoms are collected in states which don't couple to the light field. This state promises no spatially modulated light shift and hence no periodical structure is created.

Consider an atom with an $F \rightarrow F'$ transition which interacts with two counterpropagating light beams having crossed linear polarizations ($lin \perp lin$, Fig. 5.11) and blue detuning from the atomic transition. In the absence of a magnetic field and for integer angular mo-

to be the only one where the localization of atoms is possible in three dimensions. To extend a lattice into three dimensions, a σ_+ standing wave in the third dimension was added to the 2D configuration. Controlling the phase difference between the standing wave and the 2D field several lattice geometries are possible [77]. Combining a $lin \perp lin$ standing wave with a 2D light field, an antiferromagnetic 3D optical lattice can be realized [77]. Similar to the 2D case, it is possible to construct a 3D optical lattice without controlling the phases between different directions. Namely, combining four laser beams [33],[74].

An important feature of bright optical lattices is, that the atoms are trapped in the regions with maximum light intensity. As a consequence, atomic densities exceeding a few 10^{11} at/cm³ are impossible in such optical lattices. One of the limiting factors are density limitations of the MOT - due to absorption and

menta, at each point x there is a state $|\psi_{NC}(x)\rangle$ which is not coupled to the light field. This state is generally a superposition of the different Zeeman sublevels with spatially-dependent coefficients. For $F > 1$ the dark state is no longer an eigenstate of the kinetic energy and is thus slightly coupled to the other eigenstates $|\psi_C^j(x)\rangle$ ($j=1,\dots,2F$) of the light-shift Hamiltonian. At points where the total electric field has a purely circular polarization σ^+ ,

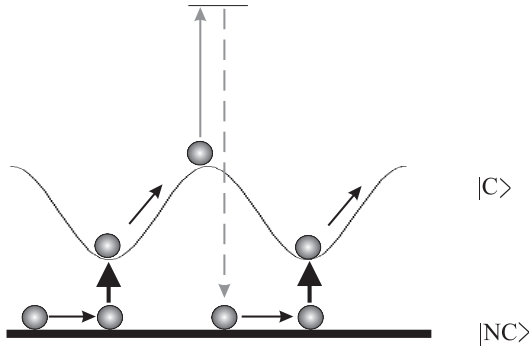


Figure 5.6: Scheme of the Sisyphus cooling mechanism in a dark optical molasses.

the non-coupling state $|\psi_{NC}(x)\rangle$ coincides with the Zeeman sublevel $|+F\rangle$, when the light polarization is σ^- then $|\psi_{NC}(x)\rangle = |-F\rangle$. Coupled states exhibit space-dependent positive light shifts. Because the eigenstates are position dependent, there is a motional coupling between the uncoupled and the coupled states, which is most efficient when the energy difference between the coupled and uncoupled states is minimal, see Fig. 5.6. The motional coupling transfers some atoms from the uncoupled state to the coupled one. In the coupled state, atoms climb a potential hill before being optically pumped back to the uncoupled state near the maximum of the potential

hill where the interaction with the light field is maximal. This process leads to an efficient Sisyphus cooling, see Fig. 5.6. This configuration is called "grey" or "dark" molasses

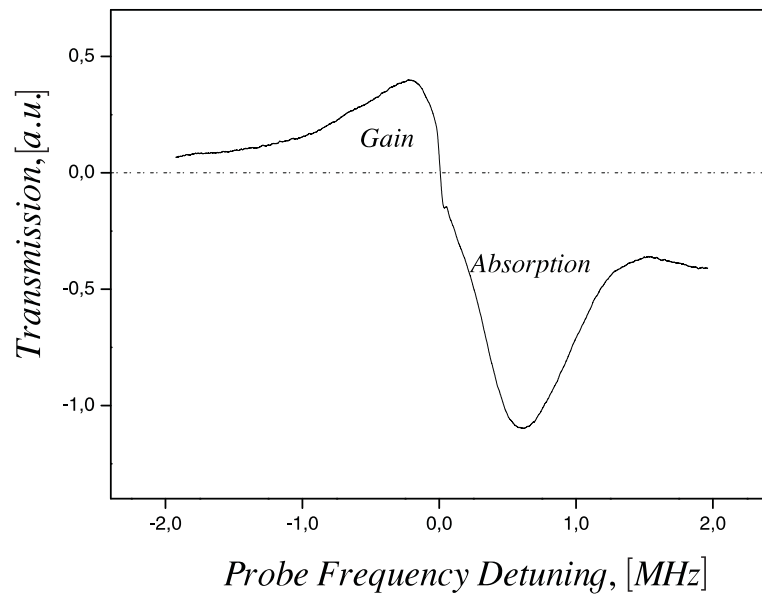


Figure 5.7: Probe transmission spectrum in a ^{87}Rb 3D dark optical molasses. The laser frequency is blue-detuned by $\delta = 10\Gamma$ from the atomic resonance. A broad resonance in the absorption is due to stimulated Raman transitions from the uncoupled to the coupled state.

because most of the atoms are in the uncoupled state and emit almost no fluorescence.

A way to see that atoms are in the uncoupled (dark) state is to perform probe transmission spectroscopy. A weak probe beam with the same polarization as that of the laser

beams, composing the molasses field, is propagating through the atomic cloud enclosing a small angle with a molasses beam. The transmitted signal from the probe beam is recorded as a function of its detuning from the frequency of the molasses beams. A probe transmission spectrum, recorded under circumstances discussed in more detail in Fig. 5.19, is shown in Fig. 5.7.

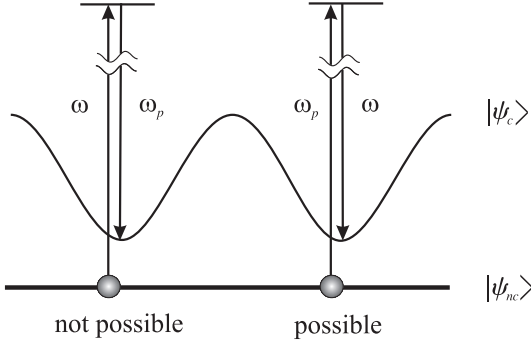


Figure 5.8: Raman coupling in the spectroscopy signal from dark optical molasses. Because the atoms are not coupled to the molasses light field there is no sideband at $\omega_p < \omega$

corresponding to this process is located at a frequency detuning $\omega - \omega_p$ equal to the light shift of the coupled level and the width of the resonance is on the order of the optical-pumping rate of the coupled level.

In this spectrum the absorptive resonance on the right is much more pronounced than the resonance providing gain on the left. Both resonance features can be explained due to Raman coupling between the uncoupled (dark) state and the state which couples to the light field. Since most of the atoms are in the uncoupled state, the Raman process involving absorption of a photon from the molasses light field and stimulated emission of a photon into the probe beam (probe beam amplification) is suppressed as compared to the Raman process involving absorption of the probe photon and stimulated emission in the molasses beam (probe beam absorption). Atoms are mostly transferred from the uncoupled state into the coupled state, see Fig. 5.8. The resonance corresponding to this process is located at a frequency detuning $\omega - \omega_p$ equal to the light shift of the coupled level and the width of the resonance is on the order of the optical-pumping rate of the coupled level.

Dark Optical Lattice

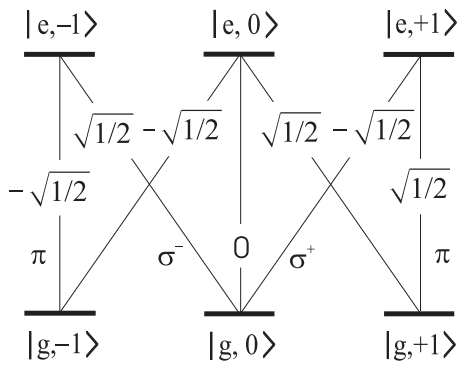


Figure 5.10: Level scheme and Clebsch-Gordan coefficients for the $J = 1 \rightarrow J' = 1$ transition.

In the dark molasses discussed above (see Sec. 5.2.1), the dark state is not spatially modulated, i.e. the optical potential for the dark state is flat. This situation can be changed if a homogeneous magnetic field is applied to the system. Then, the dark state acquires a spatially varying coupling to the light field and thus potential wells for the dark state are created.

Consider an atom with a $F = 1 \rightarrow F' = 1$ (see Fig. 5.10) transition placed in a light field with alternating σ and π polarizations¹ and an additional external homogeneous magnetic field. There exist two limits for the magnitude of the magnetic field. The Zeeman shift due to the external magnetic field can be smaller (small field limit) or larger (large field limit) as compared to the light shifts of the ground state sub-levels.

Only in the limit of large magnetic field, the dark (or non-coupled) states are associated

¹such polarization pattern is created in a $lin \perp lin$ standing wave, see Fig. 5.11

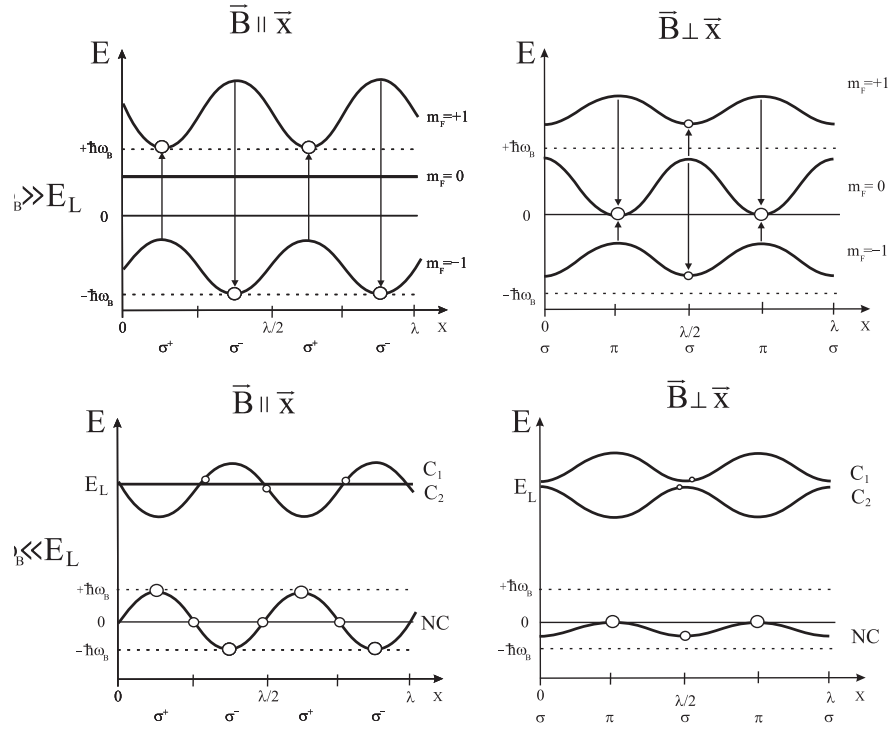


Figure 5.9: Ground state energies for different \vec{B} and $\hbar\omega_B$

with Zeeman sub-levels m_F of the ground state. In the limit of small magnetic field, the non-coupled state arises as a linear superposition of different Zeeman sub-levels.

For an atom placed in the superposition of a light field and a magnetic field, the Hamiltonian of the system will consist of three terms: the light shift, the kinetic energy $P^2/2M$, and the Hamiltonian of Zeeman shift. There are two relevant parameters $\hbar\Delta/E_{rec}$ and $\hbar\omega_B/E_{rec}$, where E_{rec} is recoil energy, $\Delta = \omega_1^2/4\delta$ is the light shift with ω_1 - resonant Rabi frequency and δ - detuning from the resonance, $\hbar\omega_B$ is the splitting between the Zeeman sub-levels $|m_g = +F\rangle$, $|m_g = -F\rangle$ and $|m_g = 0\rangle$ of the free atom. Consider first the case of a large magnetic field when $\omega_B \gg \Delta$, so that the projection m_F of the total angular momentum F on the magnetic field direction, which defines the quantization axis, still is a good quantum number. Let us take a look at the case when the magnetic field is oriented along the standing wave axis ($B \parallel x$). The light field contains no π component of polarization, hence the sub-level $m_F = 0$ is not populated, and the system behaves as an effective 3-level system. The light shift of the $m_F = 0$ state is depending only on the total intensity and thus is spatially constant. The light shifts of the two outermost magnetic sub-levels depend on the polarization. In the places of purely σ_+ polarization ($x = \lambda/8$ and $5\lambda/8$, see Fig. 5.11), the state $m_F = 1$ is a dark state, while on the places of σ_- polarization ($x = 3\lambda/8$ and $7\lambda/8$, see Fig. 5.11) the state $m_F = -1$ is completely decoupled from the light, see Fig. 5.9. Consequently, on these positions, the total population is pumped into the corresponding outermost Zeeman sub-level. With the positive (blue) detuning of the trapping beams from atomic resonance, these places are also the minima of light shift potentials, and so we obtain an optical lattice.

The dark states are characterized through the additional condition that in the presence of a magnetic field they have to be eigenstates of the Zeeman shift Hamiltonian. Let us take a look at the case of a small magnetic field $\omega_B \ll \Delta$, where the Zeeman splitting is a small perturbation as compared to the light shifts, and the lowest optical potential is mainly associated with uncoupled states. Because of the nonzero magnetic field, the potential of the lower level, which was flat for $B_0 = 0$, becomes spatially modulated because of the Zeeman shift. It presents maxima when $|\psi_{NC}(x)\rangle = |m_g = +F\rangle$ and minima when $|\psi_{NC}(x)\rangle = |m_g = -F\rangle$. At these places, the dark state is stationary and collects the entire population. At all other places, the dark state is a linear superposition of Zeeman sub-levels and the population can be transferred through the Larmor precession to the coupled states C_1 and C_2 , see Fig. 5.9. In this regime, the depth of the trapping potential is given through the Zeeman splitting.

Let us take a look at the case of transversal magnetic field ($\vec{B} \perp x$). The quantization axes is chosen parallel to the magnetic field ($\vec{B} \parallel y$), so the light field contains no pure σ_+ or σ_- polarization, but there exist places ($x = \lambda/4, 3\lambda/4$) with pure π polarization, see Fig. 5.11. At these places, the sublevel $m_g = 0$ is the dark state and has a light-shift minimum in the case of large magnetic fields, see Fig. 5.9. At the places, with $x = 0, \lambda/2, \lambda$,

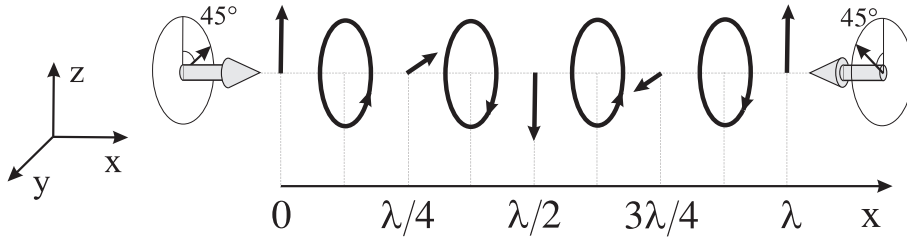


Figure 5.11: $lin \perp lin$ standing wave

the orientation of polarization is perpendicular to the quantization axes (σ -polarization), which means that the polarization is composed from σ_+ and σ_- components. Here, the potential minima for the $m_g = \pm 1$ states are located, which couple to the light, i.e., they are light shifted. In the limit of small magnetic fields, the non-coupled state has its light shift minima at places with σ polarization as shown in Fig. 5.9.

Finally, we wish to discuss question whether the atoms can be efficiently cooled down into the dark potential minima. Because of the small potential depth, efficient sub-Doppler mechanisms are necessary similarly to the case of bright optical lattices.

Consider the case of a large magnetic field ($\hbar\omega_L \gg E_L$, see Fig. 5.9). The steady-state populations for an atom at rest are labelled in Fig. 5.9 with circles. The arrows show the direction of the population transfer due to optical pumping. For both directions of the magnetic field, the length of upwards arrows is larger than the length of downward arrows. This indicates that due to optical pumping on average the system dissipates potential energy at the expense of its kinetic energy.

In the regime of large magnetic field, through Sisyphus mechanisms the sub-Doppler cooling forces acts on the atoms and provide that in steady-state the mean kinetic energy of atoms is below the trapping potential height. In the regime of small magnetic field ($\hbar\omega_L \ll E_L$), the $lin \perp lin$ configuration fulfills for an atom with the ground state $J > 1$

all conditions for appearing of non-adiabatic cooling force [77]. One expect also in this case the temperatures that are low enough to localize the atoms in the low-lying bound states.

A theoretical analysis [32] of a dark optical lattice realized in a $lin \perp lin$ configuration on a $J = 4 \rightarrow J' = 4$ transition in a magnetic field pointing along the standing wave axis ($\vec{B} \parallel \vec{x}$) shows that most of the atoms are trapped and cooled inside the potential minima. It was shown that the population of low-lying vibrational levels is maximal if the light shift and Zeeman splitting are on the same order of magnitude.

5.2.2 2D Dark Optical Lattice

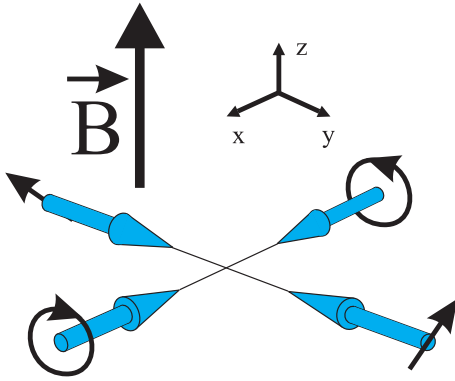


Figure 5.12: Light field configuration of 2D dark optical lattice (DOL)

field ($\vec{B} \perp \vec{x}$), where atoms are localized in the antinodes of the π polarization component [38].

We now extend the concept of dark optical lattices for the two and three dimensional space. Unfortunately, it is not possible to generalize the one-dimensional dark optical lattice with longitudinal magnetic field ($\vec{B} \parallel \vec{x}$) for the multidimensional case. If the total light field has nodes than for blue-detuning ($\delta > 0$) the nodes are the absolute light-shift potential minima for all Zeeman substates. The population will not be preferentially pumped into one of the Zeeman sublevels, so that Sisyphus cooling mechanisms are impossible in the vicinity of the potential minima. On the other hand, it is impossible to create a multi-dimensional light field configuration which does not provide nodes of its π polarization component. One way to overcome this problem is to create an optical lattice with a transversal magnetic

5.2.3 Light Field Configuration

The 2D configuration is build in the horizontal plane in the intersection region of two branches of a folded Michelson interferometer, see Fig. 5.15. Four laser beams with polarizations as depicted in Fig. 5.12 are superimposed. Two pairs of counterpropagating travelling waves form two standing waves: a $\sigma_+ \sigma_-$ wave along the x-axis and a $lin \perp lin$ wave along the y- axis, see Fig 5.12

$$\vec{E}_x = E_0 e^{i\psi} (\vec{e}_1 \cos(kx + wt) + \vec{e}_2 \cos(-kx + wt)) = -i \frac{E_0}{\sqrt{2}} e^{i\omega t} (\vec{e}_y \cos kx + \vec{e}_z \sin kx) e^{i\psi} + c.c. \quad (5.10)$$

$$E_y = E_0 (\vec{e}_3 \cos(ky + wt) + \vec{e}_4 \cos(-ky + wt)) = \frac{E_0}{\sqrt{2}} e^{i\omega t} (\vec{e}_x \cos ky + \vec{e}_z \sin ky) + c.c. \quad (5.11)$$

where

$$\vec{e}_1 = \frac{\vec{e}_y + i\vec{e}_z}{\sqrt{2}} \quad \vec{e}_2 = \frac{\vec{e}_y - i\vec{e}_z}{\sqrt{2}} \quad (5.12)$$

$$\vec{e}_3 = \frac{\vec{e}_x + \vec{e}_z}{\sqrt{2}} \quad \vec{e}_4 = \frac{-\vec{e}_x + \vec{e}_z}{\sqrt{2}} \quad (5.13)$$

are the polarization vectors of the forming laser beams.

If the time-phase difference between two standing waves is properly adjusted ($\psi = 90^\circ$, so that the total energy density is spatially constant), the total light field can be decomposed into two polarization components π and σ with field vectors parallel and perpendicular to a homogeneous magnetic field, such that the nodes of π coincide with the antinodes of σ and vice versa, see Fig. 5.13.

$$\vec{E}_\sigma = \frac{\vec{E}_0}{\sqrt{2}}(\vec{e}_y \cos(kx) + \vec{e}_x \cos(ky)) \quad (5.14)$$

$$\vec{E}_\pi = \frac{\vec{E}_0}{\sqrt{2}}\vec{e}_z(\sin(ky) + i\sin(kx)) \quad (5.15)$$

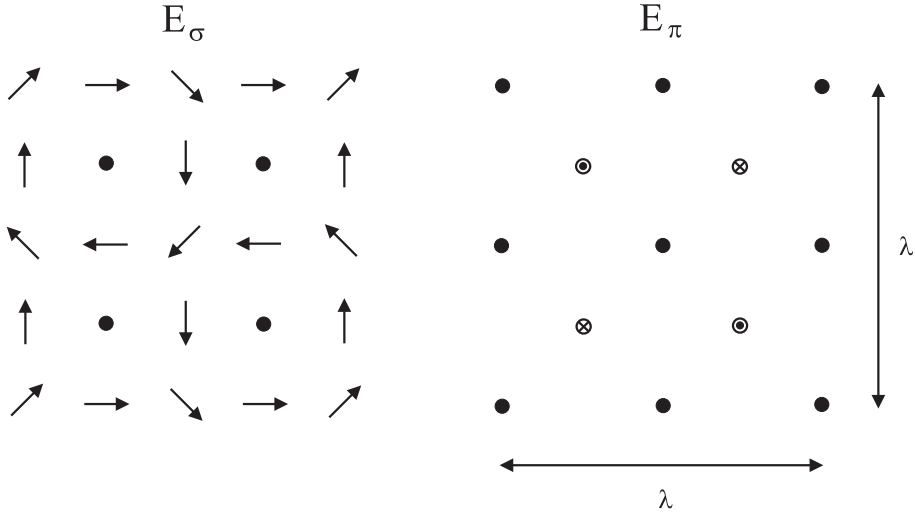


Figure 5.13: Light field of 2D dark optical lattice for appropriate choice of the time-phase difference can be decomposed into π and σ components.

In this way we produce the appropriate σ -component for trapping of atoms in the $m = 0$ -substate and the π -component that is different from zero at the σ -nodes in order to provide optical pumping into the trapped ($m = 0$) level².

²Another light field schemes can be used to produce a dark optical lattice. One can use a bichromatic field with one frequency component tuned to the blue side of an ($F \rightarrow F$)-transition and the other blue-detuned with respect to an ($F \rightarrow F - 1$)-transition, with both transitions starting from the same ground level. Alternatively, one may use bichromatic light fields with one frequency component strongly detuned to the red side of a ($F \rightarrow F + 1$)-transition and a second less intense component resonant with an ($F \rightarrow F$)-transition, where again both transitions connect to the same ground state [38].

5.2.4 Repumping Laser Field

The $3S_{1/2} \rightarrow 3P_{1/2}, F = 3 \rightarrow F' = 3$ transition of the $D1$ -line of ^{85}Rb , used for the realization of the dark optical lattice, is not closed. Thus, approximately every second photon from the lattice field tuned to the $F = 3 \rightarrow F' = 3$ transition, transfers an atom in the $F = 2$ ground state. The atoms accumulate in the $F = 2$ state and thus cease to interact with the lattice field. This problem is usually solved by using of an additional, so-called "repumper" light field, which is tuned in the resonance with the $F = 2 \rightarrow F' = 2$ transition. Now atoms are excited again state and through spontaneous emission process can go back into the $F = 3$ state, thus closing the trapping cycle. The on-resonance repumper light field would couple the trapped atoms to the light field and noticeably increase the elastic photon scattering component. To avoid this, we decided to implement a blue-detuned repumper light field which is commensurable with the trapping field, i.e. both light fields will have the same polarization structure and orientation. We superimpose the trapping and repumper light field which is blue-detuned $\delta_{rep} \approx 3\Gamma$ from the $F = 2 \rightarrow F' = 2$ transition, see Fig. 5.14.

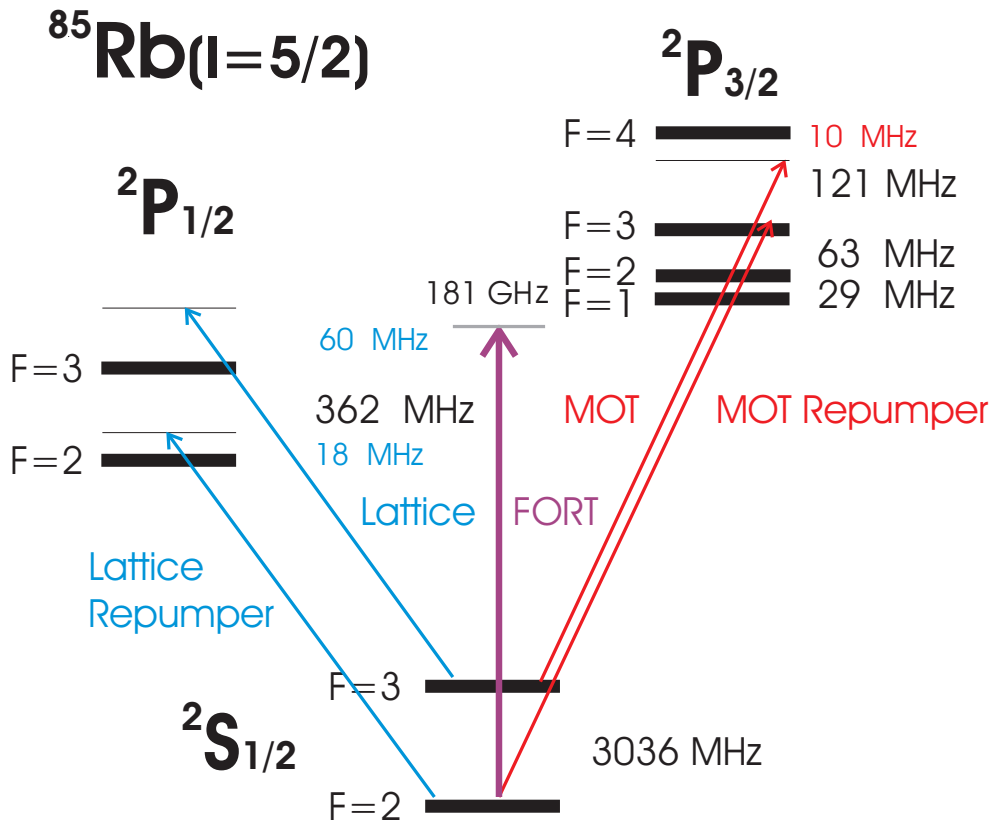


Figure 5.14: Energy levels and transitions in ^{85}Rb , which are relevant to our experimental investigations. Transition $2S_{1/2} \rightarrow 2P_{3/2}$ is used for cooling and trapping in the MOT and for the FORL, $2S_{1/2} \rightarrow 2P_{1/2}$ is a transition where the dark optical lattice is realized.

Implementing the repumper light field in the geometry of the dark optical lattice, we have to take into the account that the periodicity of trapping and repumper light fields are

not exactly the same since the wavelength of the involved transitions differ by 3.3 GHz . Overlapping the two light fields with slightly different frequencies leads to a "beat"-effect: the total field is amplitude-modulated with the period $\lambda_{\text{beat}} = 2\pi/(k_2 - k_1)$, where k_1 and k_2 are the wave vectors of the two light fields composing the lattice. Designing the lattice field, attention should be given to the distances between the end mirrors and the intersection region of the arms (distances AO and BO in Fig. 5.15), and to the length of the interferometer arms (distances AOC and BODC in Fig. 5.15).

In the intersection region, where the atoms are trapped in the optical lattice, the amplitude of the total field should be maximal. In this case the trapping potential coincides with the potential formed by the repumping field and atoms, confined in the dark states by the trapping potential remain in the dark states of the repumping potential. The electrical field at this position is given by:

$$E = E_0 e^{i\omega t} (e^{-ik_{1,2}a} + e^{ik_{1,2}a - 2ik_{1,2}L_a}) + c.c. = E_0 e^{i\omega t - ik_{1,2}L_a} 2\cos(k_{1,2}(a - L_a)) + c.c. \quad (5.16)$$

where $a = x, y$. With the requirement $\cos(k_{1,2}(a - L_a)) = 1$ for both k_1 and k_2 we get a condition on the distance $L \approx L_p n$, where n is an arbitrary integer number and $L_p = 2\pi/\Delta k = 8.8 \text{ cm}$ is the period of the beat.

Another requirement on the design of an optical lattice setup comes from the fact, that for a stabilization of the time-phase between two axis of Michelson interferometer (see Sec. 5.2.5) we need also a maximum in the amplitude of total field outside the interferometer. This condition means that on the beamsplitter (PBS2 in Fig. 5.15), the field amplitude from each arm of the interferometer should have maximal value. Not only the length of each arm should be a multiple of L_p , but also a difference between arms lengths should satisfy this condition. Our set-up for the optical lattice, see Fig. 5.15, is designed in the way to fulfil these requirements.

5.2.5 Phase Stabilization

In Sec. 5.1.2 several possibilities to create two-dimensional dark optical lattices were discussed. In the design of 2D and 3D optical lattice configurations it is necessary to consider the role of the phases of the incident beams for the interference pattern formed by these beams. The phases have to be actively kept at certain values in order to maintain the proper interference pattern.

It turns out that only the four-beam configuration with a special choice of polarizations of the interfering beams allows the localization of atoms in two dimensions. In the case of a three-beam geometry in the 2D configuration or four-beam geometry in the 3D configuration, one obtains a potential exhibiting antidots [72]. Instead of wells, associated with the localized minima of the potential, one finds there that the minima correspond to lines. Because the atoms can move along these lines, the atomic dynamics in such "gray" optical lattices is rather different from that in a red-detuned optical lattices [72].

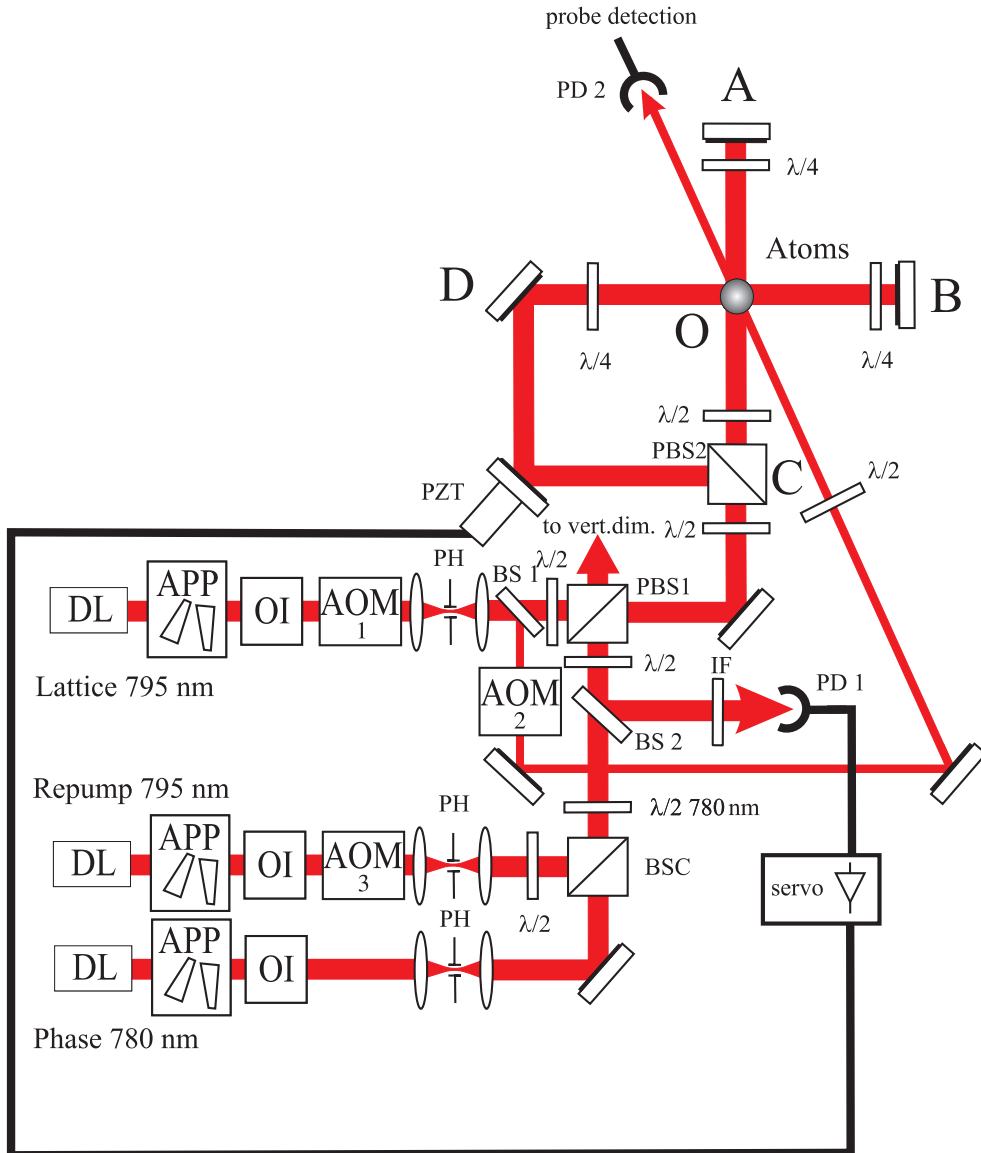


Figure 5.15: Scheme of the experimental set-up for a 2D dark optical lattice. Abbreviations: DL-diode laser, APP-anamorphic prism pair, OI- optical (Faraday) isolator, AOM-acousto-optical modulator, PH- pinhole with diameter $20\mu\text{m}$, BS-beamsplitter, BSC- beamsplitter cube, PBS- polarizing beamsplitter cube, PD-photodiode, PZT-piezoelectric transducer, IF-interference filter (serve to pass through only the light of the laser for a time-phase stabilization of the lattice) .

Phase Stabilization of Dark Optical Lattice

To stabilize the time-phase difference between two arms of the Michelson interferometer, building our lattice configuration, we used the light of an additional diode laser, referred to as time-phase laser in the following. The stabilization is based on adjusting the optical path length in the Michelson interferometer. A variation of the optical path length in one of the interferometer arms is equal to the variation of the time-phase difference. With a piezo-mounted mirror, which allows to change the position of the mirror by several μm by applying a voltage of several hundred volts, we realize an active stabilization scheme of the relative time-phase difference. The position of the piezo-mounted mirror is adjusted by a low-frequency servo feedback loop to the desired value. A fraction of the interference signal formed by backreflected light coming out from the polarizing beamsplitter (PBS1), see Fig. 5.15, is splitted on a 10% non-polarizing beamsplitter (BS2) and send through the interference filter (IF)³ to the photodiode (PD1). A change of the time-phase difference manifests itself in a changing intensity on the photodiode. The photodiode signal is now feeded in the servo loop which controls the position of the piezo-mounted mirror. Most of the optical elements assembling our interferometer are fixed on a massive metal plate, which allows for a high passive stability of the relative time-phase difference. As a consequence, an electronic servo-loop with relatively small bandwidth ($< 2\text{kHz}$) is fully sufficient for stabilization.

The frequency of the time-phase laser is tuned some tens of nanometer away from the D_2 line of ^{85}Rb at 780 nm, so that its light field has no influence on the optical lattice. The light field of the time-phase laser is collimated to a diameter of ≈ 9 mm, spatially filtered with a $20\ \mu\text{m}$ pinhole in the focus of a telescope and combined on a polarizing beamsplitter cube with the light beams forming the optical lattice.

An advantage of using an additional laser instead of using the light of trapping laser for stabilizing the phase difference is, that now we are able to turn off the lattice light fields during the MOT loading phase and transfer phase, hence we can avoid loss of atoms due to changing magnetic field in the transfer phase. All light fields forming the optical lattice can be turned off separately by using acoustooptical modulators. The shut on/shut off times for the lattice light fields are measured to be $0,5\ \mu\text{s}$.

5.2.6 Experimental Setup for a 2D Dark Optical Lattice

Our scheme of the experimental set-up for a two dimensional dark optical lattice is depicted in Fig. 5.15. The periodic optical potential is created by the light from a grating-stabilized diode laser, see Sec. 3.1.1. Its frequency is stabilized $\sim 10\Gamma$ linewidth above the $F = 3 \rightarrow F' = 3$ resonance of ^{85}Rb D_1 line. The laser beam passes some preparation steps before being used for the lattice: a pair of anamorphic prisms, an optical Faraday isolator, an acoustooptical modulator (AOM) and a telescope with a pinhole⁴ in its focus (for spatial filtering of the beam). An anamorphic prism pair is used to compensate the ellipticity of the laser diode output beam. A Faraday isolator is necessary to avoid the back-reflection of the laser beam into the laser diode, which can make impossible its frequency stabilization.

³The interference filter is used to separate the light of the time-phase laser from the total light field

⁴For details, concerning these devices see Sec. E.1

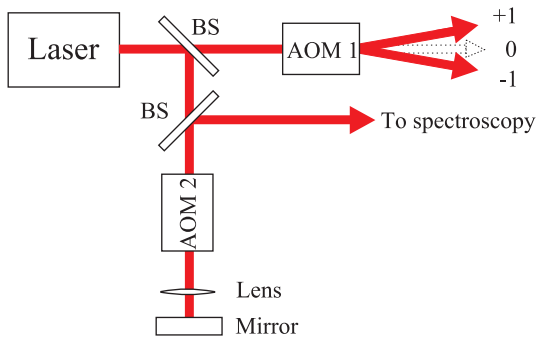


Figure 5.16: *Frequency stabilization scheme for the DOL lasers. AOM1 is placed in the output of the laser as shown in Fig. 5.15 (AOM1 and AOM3 on this Fig.). AOM2 is placed in the spectroscopy part of the set-up in a "double-pass" scheme.*

The AOM has several missions: first, it is used as a fast switch—we can switch on/off our lattice by changing the power of a radio frequency signal controlling the AOM (see Sec. 5.2.5); second, we can attenuate the frequency and intensity of the laser beam by attenuating the RF frequency and power; third, it is necessary to perform a probe transmission spectroscopy on the lattice. Spatial filtering of the lattice beam is required, because only if the lattice beams have almost plane wave fronts, interference of the standing waves results in a regular spatial pattern. The laser beams forming the repumper light field and the light field for phase stabilization are prepared in the same way as the beam for the lattice field. The lattice and repumper beams are collimated to a diameter of 6 mm each, the beam for the time-phase stabilization is collimated to a diameter of 9 mm.

After preparation, all the laser beams are combined together before entering the folded Michelson interferometer. First, the light beams of the repumper and time-phase laser are combined on the beamsplitter cube (BSC). After passing the beamsplitter, the polarization of the time-phase light field is rotated with a half-wave plate to be parallel with that of the repumper field. Thus, using combinations of $\lambda/2$ retardation plates and polarizing beamsplitter cubes (BSC2), all the light fields (lattice, repumper and time-phase) can be combined and adjusted in the intensity. Rotating the $\lambda/2$ retardation wave plates we can set the required intensity relation between the horizontal and vertical dimensions.

The detunings of the lattice and repump lasers from the atomic resonances are realized with AOMs, according to the scheme depicted in Fig. 5.16. In this scheme, one AOM (AOM1) is placed in the output of the corresponding laser and is adjusted to reflect the laser beam either into the "-1" order of diffraction (reducing the frequency of the laser beam, the case of lattice light field) or into the "+1" order (increasing the laser frequency, the case of repumper laser). The second AOM (AOM2 in the Fig. 5.16) is placed in the frequency stabilization section of the laser set-up and is adjusted in the so-called "double-pass" scheme, i.e., the light beam passes the AOM twice, thus the frequency change of the light field is doubled. The frequency of the lasers is stabilized to the crossover resonance 2-3-2 (ν_{cross}) of the $_{85}\text{Rb}$ D1-line, see Fig. 5.17. The slope of the error signal from the crossover line is steeper and larger in amplitude as compared to the signals from resonance transitions, thus providing more reliable frequency stabilization. To achieve a detuning of 60 MHz from the 3-3 resonance of the $_{85}\text{Rb}$ D1-line for the lattice laser beam, we set the frequencies $\nu_{AOM1} = +90$ and $\nu_{AOM2} = +81$. The total detuning can be calculated as: $\nu_{out} = \nu_{cross} + 2 \cdot \nu_{AOM2} + \nu_{AOM1} = \nu_{3-3} - 181 + 180 + 81 = \nu_{3-3} + 60 \text{ MHz}$. In the same manner, we realized the desired detuning of 21 MHz for the repumper transition 2-3 of the same Rb-line by setting $\nu_{AOM1} = -115$ and $\nu_{AOM2} = -70$. The total detuning in this case can be calculated as: $\nu_{out} = \nu_{cross} + 2 \cdot \nu_{AOM2} + \nu_{AOM1} = \nu_{2-3} + 181 - 230 + 70 =$

$\nu_{2-3} + 21 \text{ MHz}$.

The total power in the horizontal dimension is divided between the branches of the interferometer by a combination of $\lambda/2$ retardation wave plate and polarizing beamsplitter cube. The polarizations of the individual branches are adjusted with the retardation plates according to the scheme from Fig. 5.12. To make sure that the polarizations of all light fields will rotate equally and to maintain the thermal stability of our setup, we mostly used air spaced zero-order retardation waveplates (see Sec. E.1). To form a standing wave, each of the incoming beams is retroreflected. Special care is taken in the alignment of the retroflected beams: the incoming and reflected beams are collinear to better than 10^{-5} rad, securing that the time-phase difference is not varying over the atomic sample.⁵

5.2.7 Experimental Time Sequence

The typical experimental time sequence has the following structure. First, we load the atoms into a MOT from a thermal atomic beam. The number of trapped atoms is enhanced by cooling the atomic beam with additional light fields (see Sec. 4.4). The MOT is loaded for 1.5 seconds using a standard MOT configuration of six laser beams plus additional cooling laser beam. Some milliseconds before the MOT is switched off, we first turned off the repumper light field for cooling the atomic beam, followed by the cooling light field. Then the light fields for MOT are turned off (first repumper and later trapping light), the quadrupole magnetic field of MOT is switched off, and a homogeneous magnetic field is turned on - the procedure of switching the magnetic fields for the typical values of MOT and optical lattice magnetic fields takes about 2 ms. Subsequently, the light fields for the optical lattice are turned on. The trapping potential of our optical lattice is deep enough to trap the atoms directly from the MOT, so no additional cooling steps are needed. After the atoms evolved for some millisecond in the optical lattice (typically 5 ms, the lifetime of 2D optical lattice) first the light field, and then the homogeneous magnetic field are extinguished and after different times of free expansion, the atoms are irradiated with a resonant light pulse. When the light pulse is fully turned on (typical values for rising slope are $400 \mu\text{s}$) we open the exposure window of the CCD camera for $500 \mu\text{s}$. From the recorded images we calculated the dimensions of the atomic cloud in horizontal σ_x and vertical σ_y

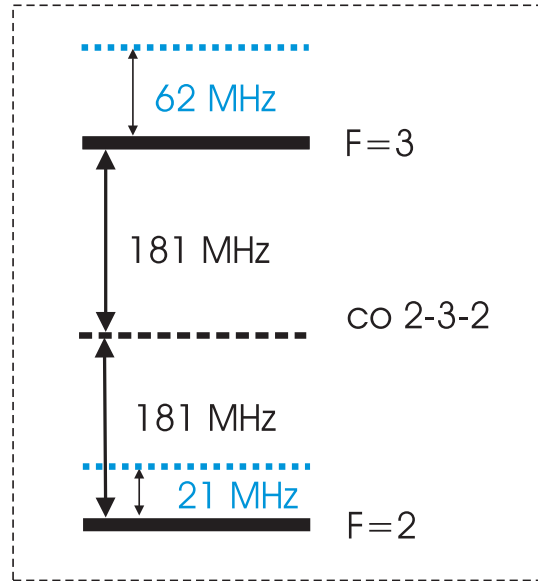


Figure 5.17: *Detuning scheme for the DOL. Blue dotted lines mark the detunings of DOL lattice and repumper light fields from the atomic resonances.*

⁵An experimental sign for a good alignment is when the retroreflected beam goes through the pinhole of the spatial filter back to the laser diode. On this position one can see how important is a good (at least 60dBm) optical isolation of the laser. Another point to mention about stability and adjustment features is that one has to choose properly the mirror mountings of the interferometer mirrors: they should be stable and sensitive to the adjustment. In our case we used the mountings from "Lees" company.

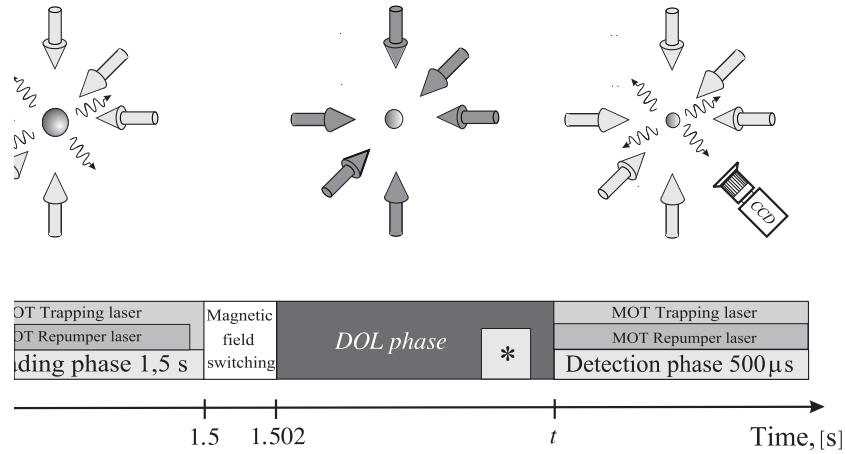


Figure 5.18: Experimental sequence of the dark optical lattice. The period during which measurements (Raman spectroscopy see Sec. 5.2.8, fluorescence observation, see sec. 5.2.10) take place is denoted with the sign "*".

directions. From the evolution of σ_x and σ_y in time we can deduce the temperature of the atoms in these directions. All the light fields are switched with AOMs, so the switching process is not adiabatic and the atoms are not additionally cooled by adiabatic lowering of the potential depth. A typical sequence for a temperature measurement is depicted in Fig. 5.18. For the absorption spectroscopy and fluorescence measurements in the optical lattice we start the signal recording when the optical lattice is still on.

5.2.8 Spectroscopic Monitoring of OL-Vibrational Spectra

A commonly used method to study the properties of optical lattices is probe transmission spectroscopy [18]. Adding a supplementary weak beam of frequency ω_p (see Fig. 5.15 and 5.19) one can monitor the intensity of the transmitted probe beam or measure the intensity of a four-wave mixing process emission, when the frequency of the probe beam ω_P is scanned around the frequency ω_L of the lattice beams. As was already mentioned in Sec. 5.2.1, two features appear on such a spectrum: a dispersive signal near $\delta = \omega_P - \omega_L = 0$ and a signal originating symmetrically around $\delta = 0$ at $\pm\delta = \omega_{vib}$ ⁶, positioned symmetrically around $\delta = 0$. Let us first examine the signal from stimulated Raman scattering process, giving rise to peaks at $\pm\delta = \omega_{vib}$.

At the beginning of this discussion we will take a look on the experimental requirements for this spectroscopy method. Stimulated Raman spectroscopy requires that probe and pump (here lattice light field) fields are coherent in phase. Thus, we split approximately 5% from the laser beam that forms the lattice light field to serve as a probe beam, see Fig. 5.15. With two AOMs: The first one, AOM1 (whose frequency (80 MHz) is constant) is placed in the beam, creating the lattice field and is used for switching the optical lattice; the second, AOM2, whose frequency is varied around the frequency of the AOM1 ($80 \text{ MHz} \pm \delta$), is positioned in the probe beam. In this way, we are able to tune the frequency of the probe

⁶ ω_{vib} is a vibrational frequency of atom in the potential well of optical lattice

beam around the frequency of the lattice field ($\delta = \omega_P - \omega_L = \omega_{AOM1} - \omega_{AOM2} \pm \delta$ with $\omega_{AOM1} = \omega_{AOM2} = 80\text{MHz}$) by maintaining the phase coherence.

The superposition of probe and lattice beams yields an interference pattern that moves in the sample with a phase velocity $v = \delta/|\vec{k} - \vec{k}_p|$. This interference pattern yields a modulation of the trapping potential. The atoms are now oscillating in the potential which is modulated. When the modulation frequency is equal to the oscillation frequency of the atoms, the probe signal shows a resonant behavior. The polarization of the probe beam should be adjusted such that the interference amplitude will be maximal and hence the amplitude of the probe beam signal. The atoms are localized at the points of π -polarization

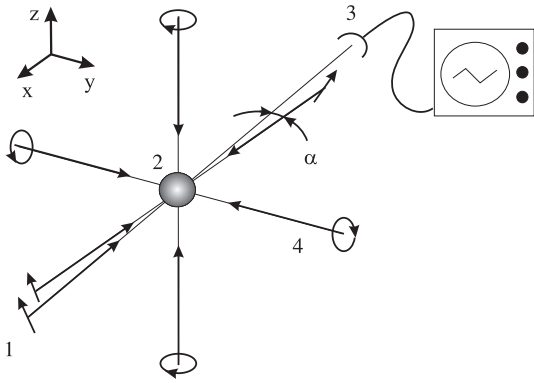


Figure 5.19: Scheme of the Raman spectroscopy in dark optical molasses. 1 - a probe beam, having the same polarization as the nearly co-propagating molasses beam, 2 - atomic cloud, 3 - detection system, 4 - molasses light beams.

in the $m = 0$ states, so the probe beam should have a σ component of polarization in order to excite atoms from these dark states. If the probe beam is π polarized (parallel to the magnetic field) no sideband structure appears on the spectrum, turning the probe beam polarization to the σ polarization (perpendicular to the magnetic field) give rise to the Raman peaks on the probe transmission spectrum at the frequencies $\delta = \pm\omega_{vib}$. Their amplitude is maximal when the polarization of the probe beam is parallel to the polarization of a co-propagating lattice beam ⁷.

Let us now examine this process from a quantum mechanical point of view. Since the atomic motion in the trapping potential is quantized, there exist discrete vibrational levels. When the frequency difference between probe and lattice field matches the vibrational frequency, stimulated Raman transitions among the vibrational levels in the potential wells are excited. Because of the population difference between the vibrational levels (the lower lying levels are more populated than the upper ones), at the detuning $\delta = \omega_P - \omega_L < 0$ a stimulated Raman process with amplification occurs, see upper scheme in Fig. 5.20 (a), while at the detuning $\delta > 0$ probe absorption is detected, see lower scheme in Fig. 5.20 (a).

Depending on the detuning and intensity of the lattice field, the amplification and absorption values vary about 10%. In Fig. 5.20 (b), an experimental spectrum is shown for a vibrational frequency of 90 kHz. For a fixed intensity of the probe beam, the amplitude of the vibrational signal is maximized when the time-phase difference between the lattice arms is set to $\psi = 90^\circ$.

The spectrum of Fig. 5.20 (b) has a dispersive shape with a width corresponding to the depth of the $m_F \neq 0$ potential wells. This shape originates from the stimulated Raman transitions between $m_F = 0$ and $m_F = 1, 2, 3$. Similar transitions are observed if the phase difference between the lattice arms is set to $\psi = 0^\circ$. In this case, the atoms are not cooled

⁷Then the interference pattern has maximum amplitude, so the trapping potential modulation is maximize (at fixed power of probe and lattice beams)

down into the light potentials anymore. This is also the reason for the asymmetrical form with respect to the frequency axis of the signal for the $\psi = 0^\circ$ situation. On the contrary to the $\psi = 90^\circ$ situation, the amplitude of the signal decreases noticeably during the measurement because atoms leaving the interaction region if they are not effectively cooled.

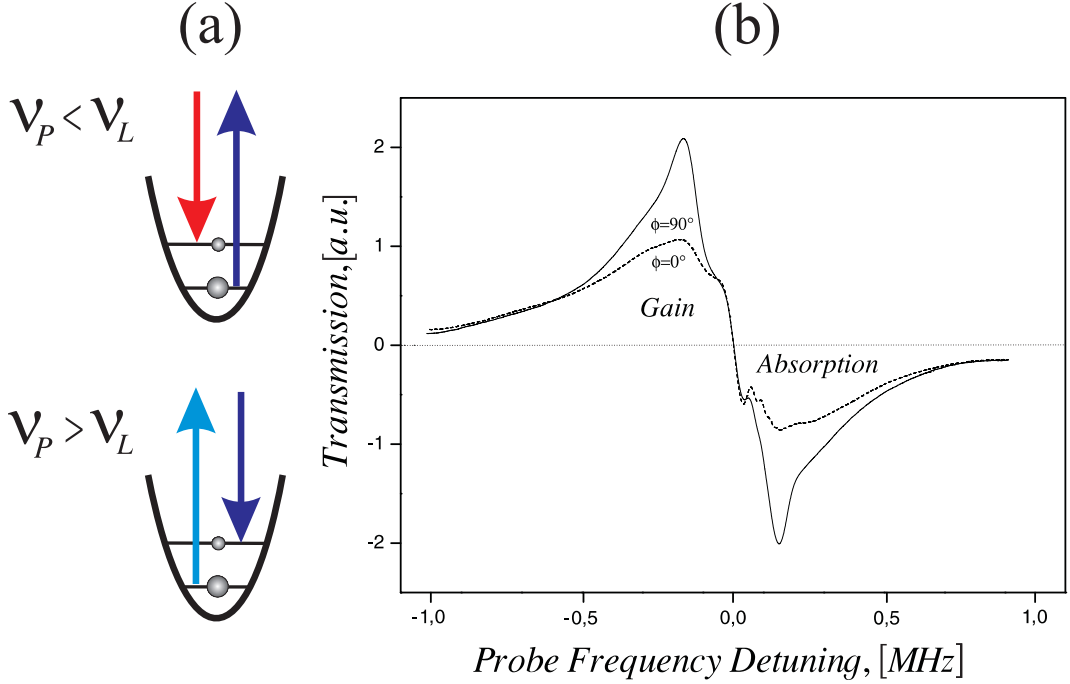


Figure 5.20: Left: Scheme for the Raman transitions in the case of probe amplification (upper scheme) and attenuation (lower scheme). Right: Probe transmission spectra of a 2D dark optical lattice. The polarization of the probe was oriented parallel with respect to that of the nearly co-propagating lattice beam. The Raman resonances are observed at 131 kHz with the corresponding width of 90 kHz. The experimental parameters of this measurement are: the Zeeman splitting $1.1\hbar\Gamma$, detuning from the atomic resonance 10Γ , Rabi frequency 4.7Γ ($\Gamma/(2\pi) = 5.98 \text{ MHz}$)

The amplitude of the Raman resonances at $\psi = 90^\circ$ is maximized for the Zeeman splitting of $\hbar\omega_B \cong -1.1\hbar\Gamma$. The resonances can be also observed for other settings of magnetic field in the region of the Zeeman splitting from $-2.1\hbar\Gamma$ to $-0.2\hbar\Gamma$. This is in a good agreement with the theoretical prediction [32], according to which the population of lowest vibrational levels is maximal if the Zeeman splitting is on the same order of magnitude as the light shift.

The lifetime of a vibrational level in a potential well, and hence the linewidth of Raman resonances, originates from two processes: 1) optical pumping towards a different potential well (another sublevel of the ground state of a trapped atom) and 2) transition towards another vibrational level belonging to the same potential well. For the $m = 0$ potential, optical-pumping processes leading back to the initial vibrational level without changing the value of m are forbidden, because the coupling polarization component σ has odd parity with respect to the center of the potential wells. This is in contrast to the conventional

optical lattices, where such elastic processes exceed all other processes by more than an order of magnitude. The relaxation rates due to m -changing transitions leading from the $m = 0$ well to the $m = \pm 1$ wells are larger than those resulting from inelastic transitions which lead back to the initial $m = 0$ potential but change the vibrational quantum number. This is also in contrast to conventional lattices where m -conserving transitions play the dominant role in the relaxation of vibrational populations. For dark optical lattices it is the vanishing of the coupling polarization component in the trap centers that suppress the relaxation of the vibrational levels, while in conventional lattices vibrational relaxation is suppressed by the Lamb-Dicke effect. The suppression in both cases is of comparable magnitude.

For an atom trapped in the $m = 0$ state, the probability to leave the potential well comes from the nonzero average of the σ component of light on the atomic wavefunction. This quantity Γ_n is proportional to $\Gamma' \langle n | I(\sigma) / E_0^2 | n \rangle$, where n is the vibrational quantum number and $I(\sigma)$ of the σ component of light. Because $I(\sigma) \approx E_0^2 k^2 x^2$ near the bottom of the well, Γ_n can be approximated by $\Gamma' \langle n | k^2 x^2 | n \rangle$ and using the properties of the harmonic oscillator, one finds [18]

$$\Gamma_n \approx \Gamma' \frac{E_{rec}}{\hbar\omega_{vib}} (2n + 1) \quad (5.17)$$

The experimentally observed width of the Raman resonances is much smaller than the photon scattering rate

$$\Gamma' \approx \frac{\omega_1^2}{2\delta^2} \Gamma \quad (5.18)$$

If the vibrational lines would be well isolated, the width of the transition between two vibrational levels $n \rightarrow n + 1$ would be on the order of $n\Gamma'(E_{rec}/\hbar\omega_{vib})$ [18], that is smaller than Γ' because of the Lamb-Dicke factor $\eta = E_{rec}/\hbar\omega_{vib}$ ⁸. The factor $(2n + 1)$ (similarly as the Frank-Condon factor in molecular physics) comes into play because of the spatial confinement of the atomic center-of-mass wave function which increases with decreasing n : the wavefunctions of well-confined levels have little overlap with those of any other levels. Rate equations involving the relaxation rates of the vibrational levels yield their steady-state populations. These steady-state populations decrease strongly with increasing vibrational quantum number.

The shape of the Raman resonance is an envelope of different transitions $n \rightarrow n + 1$, which have different frequencies due to the anharmonicity of the potential. Thus the width of Raman signals can give information whether the population is mostly in lower ($n = 0, n = 1$) vibrational levels or not.

We used the signal of probe beam spectroscopy for a fine adjustment of the lattice light field (polarization of individual beams, geometrical adjustment of the branches and time-phase difference). Since the width of the Raman peaks is dependent on the population of the vibrational levels, on the symmetry of the potential wells and on the equality of the potential depth at different lattice sites an indication for a perfect alignment are narrow Raman peaks with maximal amplitude for the fixed probe-beam power. As was mentioned

⁸For our experimental conditions we arrive Lamb-Dicke factor $\eta \sim 1/34$

above, the geometry of the lattice potential is strongly dependent on the time-phase difference between the branches of the interferometer, thus the Raman spectrum was used for fine adjustment of the time-phase difference.

Finally, let us briefly mention a feature appearing on the probe spectrum in the vicinity of $\delta = 0$, which originates from a Rayleigh scattering process. Rayleigh scattering results from the scattering of light on any nonpropagative modulations of atomic observables (in the case of optical lattices: magnetization, density and velocity) [19] and the width of the Rayleigh resonance carries the information on the damping time of these observable variables.

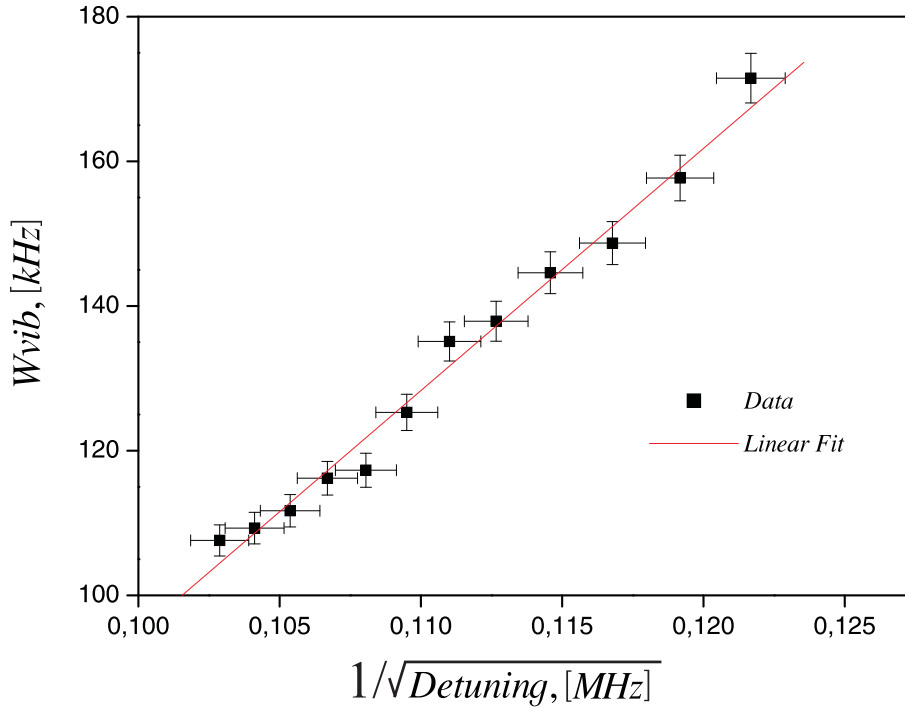


Figure 5.21: Dependence of the vibrational frequency of atoms in the lattice potential on the detuning ($1/\sqrt{\delta}$) of the lattice field.

The vibrational frequency of the localized atoms follows the relation $\omega_{vib} = 2\sqrt{\Delta\omega_{rec}}$. In our case, the ground state $m = 0$ couples only on the σ -component of the light field. Therefore, we expand the optical potential of this component in the vicinity of its minimum, i.e. in the vicinity of the places of pure π polarization:

$$U_{m=0}(x) \cong \hbar \frac{\omega_1^2}{8\delta} (kx)^2 \quad (5.19)$$

the corresponding vibrational frequency in this potential is given by:

$$\omega_{vib,m=0}(x) = \omega_1 \sqrt{\frac{\omega_{rec}}{2\delta}} \quad (5.20)$$

For the typical experimental conditions of our setup, we expect to detect the Raman resonances at $\omega_{vib} \simeq 110 \text{ kHz}$. Moreover, as can be seen from Eq. 5.20, the vibrational

frequency should vary linearly with $1/\sqrt{\delta}$. In Fig. 5.21 the experimental confirmation of this dependence is shown.

5.2.9 Temperature Measurements

Typical temperatures of the atoms in our two-dimensional dark optical lattice are about $14 \mu K$. Note that such temperatures are achieved only along the trapping (horizontal) dimensions. Along the vertical direction no trapping potential is available, hence the cooling is not working. This is due to the fact that the geometry of the two-dimensional dark optical lattice has open channels in vertical direction. The atoms are trapped at the positions of pure π polarization. In the horizontal plane these points are embedded in the variable σ field. In the vertical direction there exists no variation, neither in the π nor in the σ component, i.e., the atoms are not confined and move freely in vertical tubes. Along this direction the atoms can be heated so that the temperature is noticeably higher than the initial temperature in the MOT, the typical value for the temperature in the vertical direction is about $500 \mu K$.

Temperature is well defined in a system which is in thermal equilibrium, i.e., the atomic velocities follow a Maxwell-Boltzmann distribution. There exist several methods to measure the temperature of atomic ensemble. They can be divided into two categories: spectroscopic methods and time-of-flight methods.

One spectroscopic velocimetry method is based on recoil-induced Raman resonances [19]. This method was introduced by Meacher et al. [50]: nearly co-propagating pump and probe interact with a cloud of free atoms. Analyzed in the momentum basis, the absorption of a pump photon followed by the stimulated emission of a probe photon can be viewed as a Raman transition between two states with different transverse momenta. The transmission spectrum of the probe (as a function of δ) is proportional to the derivative of the momentum distribution.

In the experiments carried out in this thesis, a time-of-flight (TOF) method has been used to measure the temperature of the trapped atoms. This diagnostic method was developed for the optical molasses [48, 64] and gives the vertical temperature of an atomic ensemble. The basic idea of this method is as follows: a cloud of trapped atoms is released from a confining potential by turning off the light beams. Under the effect of gravity the atoms fall towards a probe located a few centimeters below the trap position. By passing through the nearly resonant light of the probe beam the atoms emit fluorescence photons. The temporal variation of this fluorescence is related to the initial velocity distribution of the atoms in the trapping potential and therefore to the kinetic temperature of the atoms. By measuring the temporal distribution of the fluorescence signal, and comparing it with a Maxwell-Boltzmann distribution, the temperature can be derived. The main problem of this method is that it requires precise knowledge of the initial size of the atomic cloud, especially in the case of low initial temperatures of the atomic ensemble.

In our experiments we used a slightly modified TOF method, namely instead of installing an additional probe beam, we used the near-resonant light of our MOT setup to illuminate the free expanding atoms after a given time of free expansion. The fluorescence signal was monitored with a normalized CCD camera. From the time evolution of the atomic cloud size we can reconstruct a 2D momentum distribution and, hence the

temperature of the ensemble.

Let us examine a simple theoretical model of the cloud expansion. After the trapping forces are removed, the evolution of atoms is described by $x(t) = x_0 + vt$. Atoms are distributed in the velocity according to the Gauss distribution $f(v) = \exp(-v^2/v_0^2)$ with $v_0 = 2kT/m$, so for the spatial distribution we get:

$$f(x, t) = e^{-\frac{m}{2kTt^2}(x-x_0)^2} \quad (5.21)$$

at the beginning of the expansion, the atomic cloud has already non-zero radius σ_0 , so

$$f(x, t = 0) = e^{-\left(\frac{x_0}{\sigma_0}\right)^2} \quad (5.22)$$

The normalized number of atoms at a given time t in a certain volume is

$$\frac{N(x, t)}{N_0} = \int e^{-\frac{m}{2kTt^2}(x-x_0)^2 - \left(\frac{x_0}{\sigma_0}\right)^2} dx_0 \quad (5.23)$$

$$= \sigma_0 \int e^{-\gamma(y-y_0)^2 - y_0^2} dy_0 \quad (5.24)$$

$$= \sigma_0 e^{-\frac{\gamma}{\gamma+1}y^2} \int e^{-(\gamma+1)\left(\frac{\gamma}{\gamma+1}y - y_0\right)^2} dy_0 \quad (5.25)$$

$$\approx e^{-\frac{\gamma}{\gamma+1}\frac{1}{\sigma_0^2}x^2} = e^{-\left(\frac{x}{\sigma(t)}\right)^2} \quad (5.26)$$

where the following substitutions: $\gamma = \sigma_0^2/v^2 t^2$, $y = x/\sigma_0$, $y_0 = x_0/\sigma_0$ and $\sigma^2(t) = \sigma_0^2 + 2kTt^2/m$ have been used. We thus described the evolution of an atomic cloud after the trapping forces were removed. The temperature of the atomic ensemble can be determined by fitting of $T = (\sigma(t)^2 + \sigma_0^2)m/2kt^2$, where the width of the atomic distribution at the beginning of measurement σ_0 and after a certain time interval t , $\sigma(t)$, are deduced from the widths of Maxwell-Boltzmann distributions fitted to the data.

5.2.10 Evolution of the Atomic Cloud

We studied the evolution of the atomic cloud in our two-dimensional dark optical lattice. At different times of evolution in the lattice, we took images of the fluorescence from atoms trapped in the lattice. Our observations show that the size of atomic cloud in the direction of confinement (horizontal direction) remains constant, whereas the size in vertical direction is growing very fast. Along the horizontal directions, the confinement is high and during the lifetime of the two-dimensional lattice (typically 5 ms, which is also the typical time interval of our measurements) nearly no diffusion can occur. For the behavior of atoms in the vertical direction we found the following explanation. As can be seen from the experimental data (shown in Fig. 5.23), after 1 ms in the lattice, atoms gain a final temperature and expand now linearly with time. The reason is, that in the beginning of the lattice phase, a large number of photons are scattered as the result of the cooling processes in the lattice. In fact, the initial temperature of the MOT of $70\mu K$ is reduced to $13\mu K$ in the horizontal directions, so we can estimate the number of inelastic scattered photons per atom for this cooling process as:

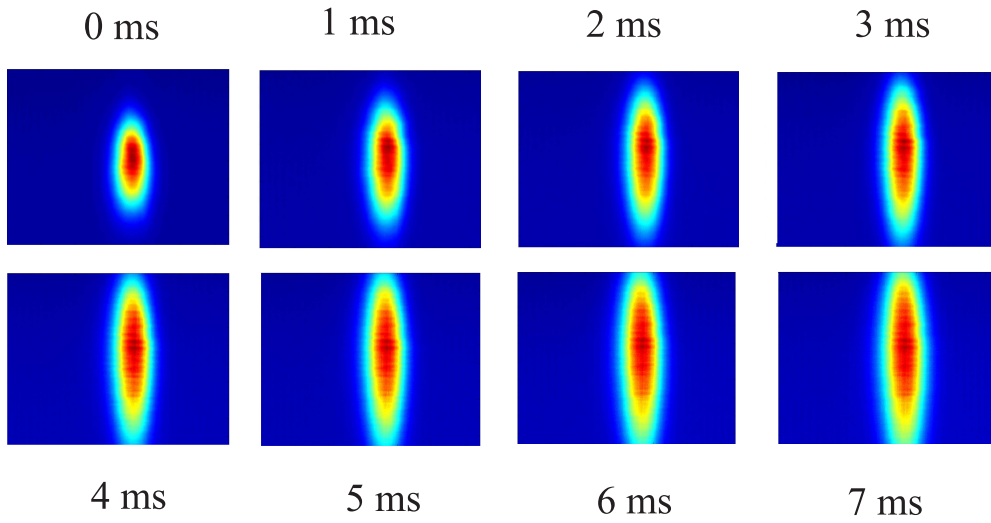


Figure 5.22: *Evolution of the atomic cloud in the 2D dark optical lattice.*

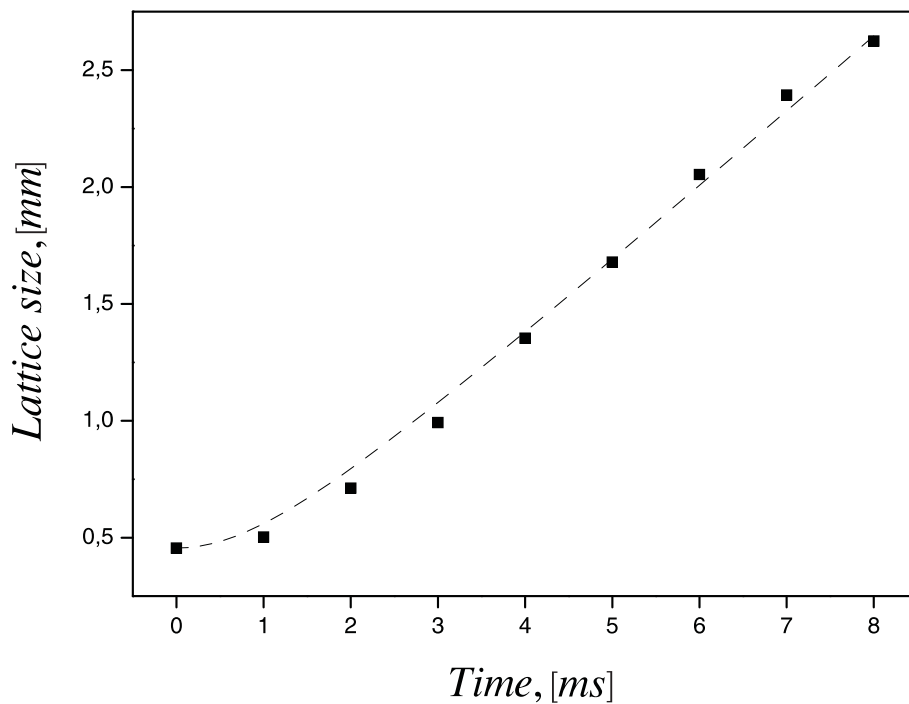


Figure 5.23: *Vertical size of the atomic cloud trapped in the 2D dark optical lattice as a function of time. The data points corresponding to the y-axes are gained from the raw data as follows: we take into account the finite size of the light field forming our lattice and fitted the data (dashed line) with the convolution of two Gauss functions (one corresponding to the light field, typ. $w_0 = 2\text{mm}$, and the other one to the atomic distribution).*

$$n_{scatt} = \frac{T_{MOT} - T_{latt}}{T_{rec}} = 154 \quad (5.27)$$

The number of elastic photons per atom emitted during this time is evaluated by division by the Lamb-Dicke factor η (see Sec. 5.1.1)

$$n_{elast} = n_{scatt} \cdot \eta = 154 \cdot 8 = 1232 \quad (5.28)$$

These photons contribute to the vertical heating and the corresponding temperature increase can be estimated as follows :

$$\delta T_{vert} = n_{ph} \cdot T_{rec} = (n_{elast} + n_{scatt}) \cdot T_{rec} = 513 \mu K \quad (5.29)$$

After the cooling phase, atoms are trapped in the optical lattice and, hence pumped into the dark states where they are unable to scatter further photons, so the heating in the vertical direction is stopped. Atoms move now ballistically along the vertical direction with the new increased temperature. Time required for the cooling phase we estimate as:

$$t = n_{ph} \cdot 1/\Gamma_{pump} = 374 \mu s \quad (5.30)$$

With the model of ballistical expansion :

$$\sigma_x = \sqrt{\sigma_o^2 + 2kT/M(t - t_o)^2} \quad (5.31)$$

we found a satisfactory agreement between experimental points and theoretical fit(see Fig. 5.23). The value for the temperature of atoms in the vertical dimension received from this model ($T = 602 \mu K$) show the good correlation with the temperature value of $544 \mu K$ measured according to the ballistically expansion method described in Sec. 5.2.9).

The lifetime of our 2D dark optical lattice was measured to be typically about 5 ms. We explain this small value by strong heating of trapped atoms in the vertical direction. Considering the vertical temperature of $544 \mu K$, the *Rb* atoms which are confined in the center of the trap will leave the trap volume ($w_o = 1.7 mm$) in 7 ms. This value corresponds well with the measured lifetime.

5.3 Extension to the 3D DOL

Our two-dimensional dark optical lattice configuration does not provide cooling and trapping in the vertical dimension, see Sec. 5.2.10. The light shift potentials look like tubes, opened vertically on both ends, thus providing efficient escape channels for trapped and cooled atoms. This atom loss mechanism was shown in the experiments described in Sec. 5.2.10 and Sec. 5.2.9. To provide efficient trapping for the cold atoms, an additional light field oriented along the vertical dimension should close the trapping potential.

5.3.1 3D DOL Configuration

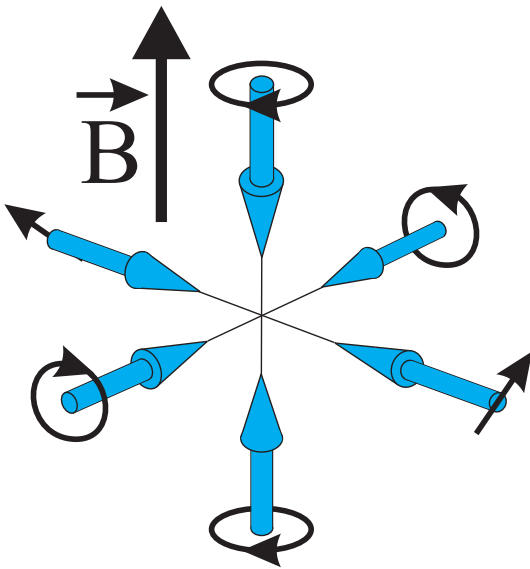


Figure 5.24: *Light field configuration of 3D dark optical lattice (DOL)*

In order to obtain a three-dimensional dark optical lattice, we add to the two-dimensional configuration (described in Sec. 5.2.2) a σ -polarized standing wave along the vertical dimension. The corresponding light field configuration is depicted in Fig. 5.24. The localization in 2D DOL takes place in the minima of σ -polarization, the component of the light field which is perpendicular to the vertically oriented magnetic field (see Sec. 5.2.2). The π -component of the total light field has maximum amplitude at those places, providing an efficient pumping into the dark state. The only way to provide trapping in the vertical dimension is to create a σ -polarized light field, exhibiting maxima and minima along the vertical axis. Such a condition is fulfilled in a σ -polarized standing wave as shown in Fig. 5.24. At the places, where the vertical σ -polarized standing wave exhibits minima, the π -component from the 2D optical lattice provides optical pumping into the dark state, and

hence the localization in the potential minima along the vertical direction.

Let us now discuss the role of the phase difference between the vertical σ -polarized standing wave and the 2D DOL oriented in the horizontal plane. As described in Sec. 5.2.5, to maintain the desired polarization pattern of the 2D optical lattice (see Sec. 5.2.3) one should actively control the phase between two standing waves that form the lattice. In the case of 3D optical lattice, which is created by intersection of three standing waves, one has to control two phases: one between the horizontal standing waves, and the second between horizontal plane and the vertically oriented standing wave. How important is to control the phase between vertical and horizontal planes in the 3D dark optical lattice, and what kind of complications it will imply if this phase remains uncontrolled? The uncontrolled phase between horizontal and vertical planes leads only to the spatial shift of the potential minima along the vertical axis (on the contrary to the role of the phase difference in the horizontal plane, where the proper phase difference makes the trapping possible). The time constant for the potential minima position change is much longer than the cooling

time for the atoms inside the potential minima. Therefore, one can assume that the atoms adiabatically follow the changing positions of the potential minima. For the application of the 3D DOL as trapping and cooling potential it is thus unimportant to fix the phase between the horizontal and vertical planes to a certain value.

5.3.2 Properties of 3D DOL

Localization, temperature and lifetime are important parameters in characterization of optical lattice. To prove, that our 3D dark optical lattice provides an efficient localization of atoms in the potential minima of light field, we measured the transmission spectrum of a probe beam according to the scheme from Sec. 5.2.8. To confirm the trapping along the vertical direction, one should record Raman sidebands in the transmission of a vertically oriented probe beam. On the other hand, it is desirable to see the direct difference to the situation in 2D lattice. Also, the confinement in the vertical dimension will noticeably change the signal from the horizontally oriented probe beam, since cooling and trapping in vertical direction dramatically increase the population of the lowest vibrational levels in the optical potentials. That is why we decide to directly compare the signals from transmission spectroscopy in the cases of 2D and 3D dark optical lattices. We record the transmission signal from the 3D dark optical lattice according to the measuring scheme, described in Sec. 5.19. Then we blocked the light beam forming the vertical σ -polarized standing wave, and took the signal from the 2D dark optical lattice. The conditions, that are relevant for the 2D optical lattice and the probe beam, remain unperturbed for both signals. The only difference is the addition of the vertical standing wave, ensuring the 3D extension of the dark optical lattice. As can be seen from Fig. 5.25, considerably more atoms are trapped in 3D DOL in comparison to the 2D lattice. The detected vibrational frequency of the localized atoms remain the same, since the parameters of the horizontal 2D DOL are unperturbed. Signal from the Raman spectroscopy of the 3D DOL can be used as an indicator for a good power balance between horizontal and vertical dimensions of the dark optical lattice. Indeed, if the optical potentials in the vertical and horizontal directions are not equal, that would lead to the different vibrational frequencies along vertical and horizontal axis. We optimized the power balance between horizontal and vertical dimensions by monitoring the Raman spectroscopy signal in the horizontal plane (for details of this spectroscopy arrangement see Sec. 5.2.8). The power is well balanced if the Raman resonances in the 3D DOL are not broadened in comparison to the 2D DOL and positions of these resonances remain the unperturbed.

Another good indicator for a successful realization of 3D dark optical lattice is a uniform temperature along the three dimensions. As is shown in Fig. 5.26, in our 3D DOL the vertical and horizontal temperatures are equal. This temperature measurement yields a value of $8.5 \mu K$. The form of the atomic ensemble inside the lattice and after the release remains symmetrically and constant, which delivers an additional confirmation for the homogeneity of the total optical potential.

From the fact, that the trapping optical potential of our 3D DOL is independent from the direction and the cooling in all three dimensions, one expects the increase in the lifetime of the atoms inside the optical lattice. We observe a value of 116 ms, which is more than order of magnitude larger than the lifetime of the 2D DOL (see Sec. 5.2.2). This value is,

however, much smaller than the lifetime of the 3D dark optical molasses, which is typically about 1 s. This discrepancy in the lifetime values one could explain with the fact that in the optical lattice the cooling and trapping processes occur under strong interaction with the light field which leads to the population of the continuum. Those atoms contribute to the loss. On the contrary, in the dark molasses atoms are pumped into the dark state which is completely decoupled from the light field, the final lifetime of the molasses is therefore limited only by the vacuum conditions.

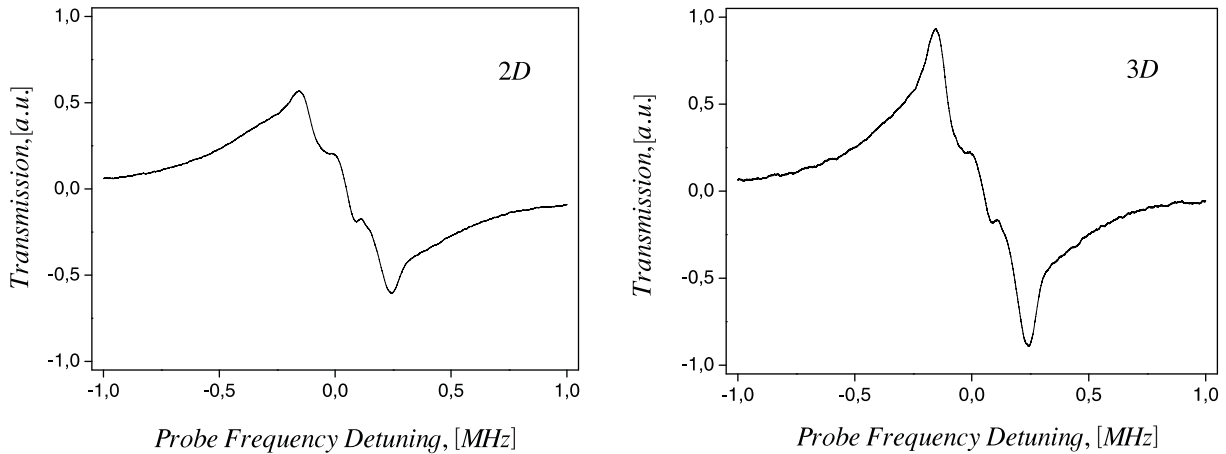


Figure 5.25: Comparison between spectra of 2D and 3D dark optical lattices. Left: Signal from Raman spectroscopy acquired in the scheme 5.19 from 2D DOL. Right: The signal taken in the same setup from 3D DOL. The vibrational frequencies are equal in both cases, since the parameters for 2D lattice remain the same. Considerably more atoms are localized in the potentials of 3D lattice due to the trapping in the vertical direction.

5.3.3 Temperature Dependence on Lattice Parameters

In this section we study the dependence of the temperature of the trapped atomic sample on the value of the magnetic field B . The experimental sequence is described in Sec. 5.2.7. Dark optical lattice is loaded from the MOT. The value of the magnetic field is set prior to the beginning of the optical lattice phase. We let atoms evolve in the dark optical lattice for 6 ms, and then measure the temperature of the atomic ensemble with the time-of-flight method, see Sec. 5.2.9.

The experimental results are presented in Fig. 5.27. It can be seen that the temperature increases with the magnetic field as long as the Zeeman splitting $\hbar\omega_B$ between the outermost ground-state Zeeman sublevels is smaller than the typical light shift $\hbar\Delta$ of the coupled states. The temperature reaches its maximum when $\hbar\omega_B$ is on the order of $\hbar\Delta$, and then decreases towards an asymptotic value.

Our explanation of this temperature behavior is based on the analysis of Refs. [55, 72]. For zero magnetic field, the atom-laser configuration is very similar to the one employed in subrecoil cooling, and one expects very low temperatures. In the limit of small values of the magnetic field $\hbar\omega_B \ll \hbar\Delta$, most atoms are accumulated in the energy states associated with the lowest nearly dark optical potentials. As the magnetic field increases from

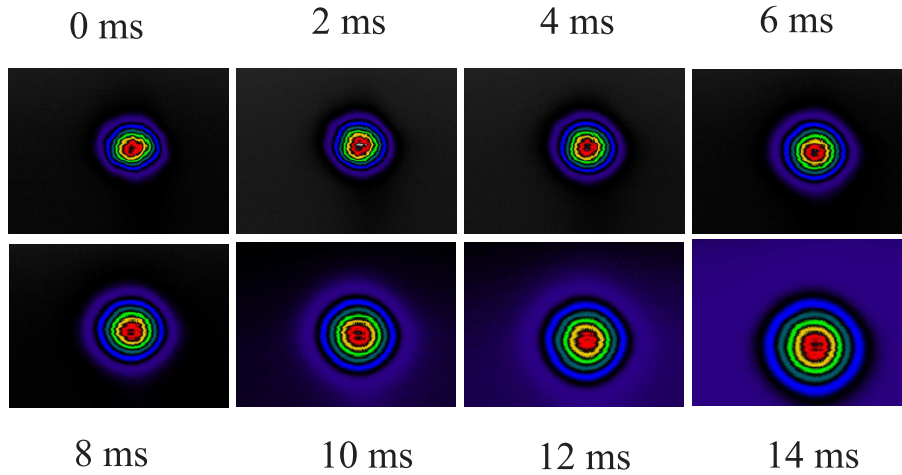


Figure 5.26: Pictures from the time-of-flight temperature measurement of the 3D dark optical lattice. The symmetrical form of the atomic sample, preserved at all times of free expansion indicates the identical temperatures in the vertical and horizontal directions. For comparison with the 2D case see Fig. 5.23

zero, potential wells of depth $\hbar\omega_B$ start to develop around points where the uncoupled state coincides with the Zeeman sublevel $m_g = 0$ and where atoms become trapped and spatially localized. With increasing magnetic field atoms will be more tightly confined in the potential wells induced by the magnetic field and the temperature of atoms increases. The temperature increase has a second reason: atoms become coupled to the light field through the wings of their wavefunctions and optical pumping from the lower energy level to the higher energy light shifted sublevels is thus less and less forbidden when B increases. More and more atoms accumulate in the coupled states, which are motional coupled to the continuum states of the lower potential curves - this leads to temperature increase. In the limit of large B ($\hbar\omega_B \gg \hbar\Delta$), where the light shifts are small perturbations compared to the Zeeman splitting, the optical potentials are essentially associated with the bare ground-state Zeeman sublevels $|m_g\rangle$. These potentials are spatially modulated because of the light shifts induced by the space-dependent laser field. The optical potential, associated with the $|m_g = 0\rangle$ state, exhibits minima at points where the Zeeman sublevel coincides with the uncoupled state. The atoms accumulate at the bottom of these potentials, hence minimizing their interaction with light. Atoms with sufficient kinetic energy to escape from $|m_g = 0\rangle$ sites may climb a potential hill associated with these potentials before being optically pumped by increasing σ^- component of the lattice field in the $|m_g = \pm F\rangle$ state. The height of the potential is proportional to the light field intensity - therefore the temperature will increase with the intensity. The cooling mechanism is more efficient when B increases because the eigenstates for the potential are closer to the Zeeman sublevels. For large B , the eigenvalues are close to Zeeman sublevels and the light shift is just a space-dependent perturbation that gives the modulation to the potential curves. In this limit, the depth of the potential wells, and hence the temperature of the atoms is proportional to the light intensity and independent of the magnetic field.

To confirm this, we measured the variation of the kinetic temperature in the limit of

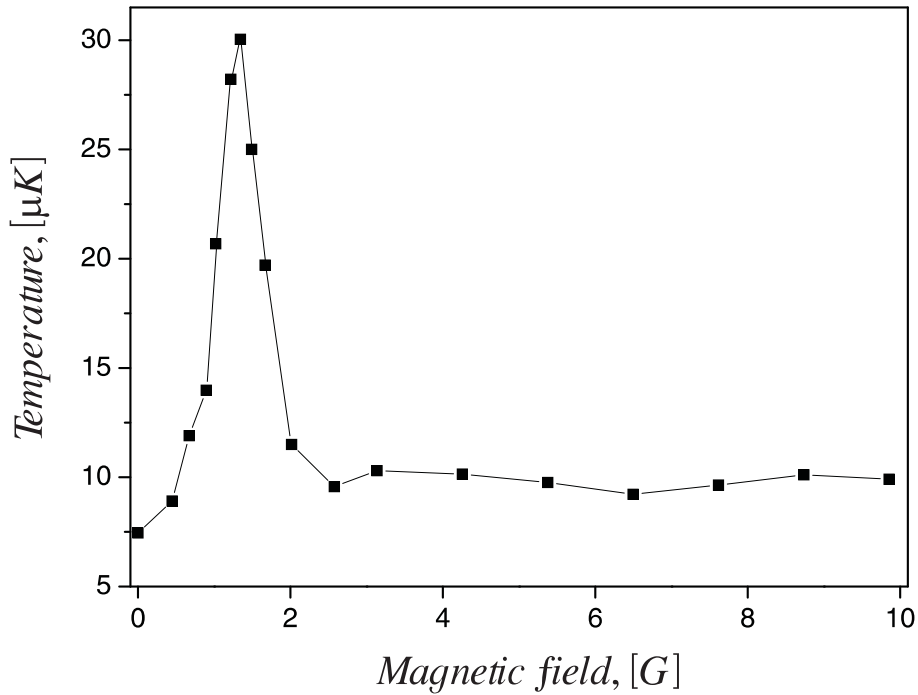


Figure 5.27: Variation of the atomic kinetic temperature in the 3D dark optical lattice with the static magnetic field B .

high magnetic field regime with the light shift in the lattice, see Fig. 5.28. We set the magnetic field value to 8 G , the typical value for most experiments, performed with our dark optical lattice. Different light shift values are adjusted by simultaneous attenuation of the intensity of the trapping and repumping light fields for the optical lattice. Atoms evolve for 15 ms in the 3D dark optical lattice followed by the temperature measurement. During the lattice phase we perform Raman spectroscopy (see Sec. 5.2.8) in order to monitor the capture efficiency of the lattice and to confirm that the phase difference has the proper value, see Sec. 5.2.5.

A near-resonant optical lattice is characterized by dissipative processes resulting in heating and cooling effects, whereby the cooling process is associated with the Sisyphus cooling (Sec. 1.3). In this well-known scheme, an atom climbs a potential hill, thus losing kinetic and gaining potential energy, and is optically pumped to a potential minimum, while the energy is carried away by spontaneously emitted photons. The heating process originates in this model, for instance, through fluctuations of momentum carried away by fluorescence photons. The steady-state temperature obtained in Sisyphus cooling scaled as the modulation depth of the optical potential ($T \sim \hbar\Delta$). This scaling law has been demonstrated in semiclassical [20] and full quantum mechanical [11, 13] treatments. Further, it was experimentally proved with the "bright" optical lattices [42], as well. All these studies show, that when the intensity gets too low the laser cooling becomes inefficient and the temperature increases abruptly. This behavior is commonly called *décrochage*. Variation of the temperature with the light shift in the 3D dark optical lattice (as shown in Fig. 5.28) shows linear dependency from the potential depth till the minimum temperature

of $\sim 6.8 T_{rec}$ is arrived at $U_{pot} = \hbar\Delta \sim 75 E_{rec}$. At this point the potential becomes too flat to provide a confinement inside the potential minimum (the last bound vibrational state leaves the potential well). The cooling process loses its efficiency and the temperature of the atoms increases.

Decreasing the light shift leads, on the one hand, to lower temperatures of the trapped atomic sample, and, on the other hand, to a decrease in the capture efficiency, i.e. to a loss of trapped atoms. One way to obtain a cold ensemble without drastically reducing the number of the trapped atoms, is to adiabatically cool the optical lattice, originally optimized for the maximum capture efficiency.

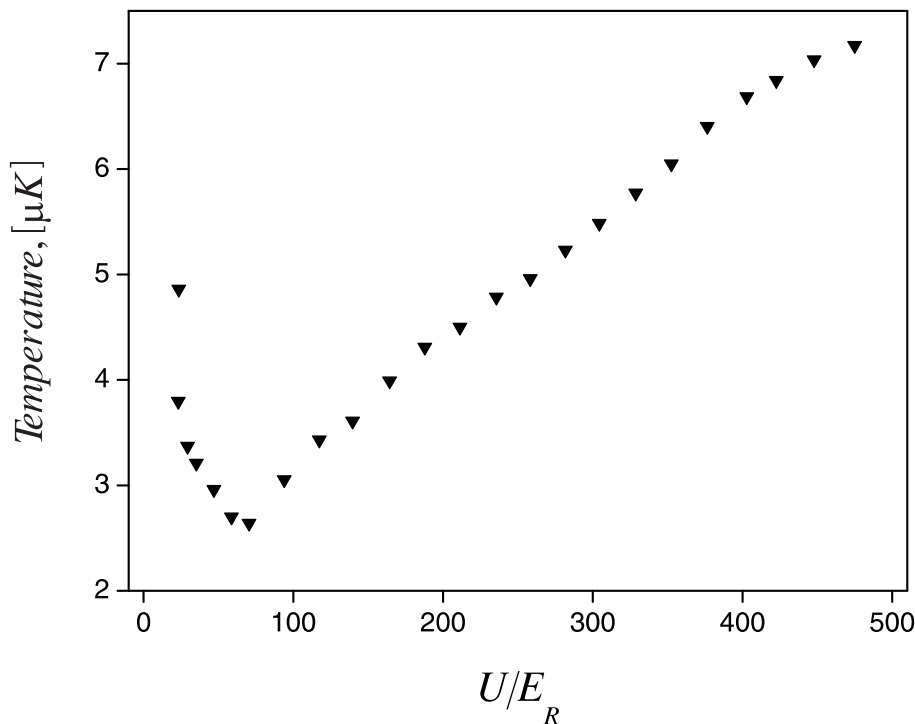


Figure 5.28: Variation of the atomic temperature in the 3D dark optical lattice in the high-magnetic-field regime with the typical light shift $U = \hbar\Delta$.

5.3.4 Adiabatic Cooling

Adiabatic expansion of the atomic center of mass distribution has been used in a number of experiments [14, 44] to reduce the temperature of the trapped ensemble. To satisfy the condition of adiabaticity, one must have $|\dot{\omega}|/\omega = \varepsilon\omega$, where $\varepsilon \ll 1$ and ω is the oscillation frequency in the optical potential. An obvious way to accomplish adiabatic expansion is to decrease the lattice light intensity. From the fact that $\omega = 2\sqrt{\Delta\omega_{rec}}$ and $\Delta = \Gamma^2/(8I_{sat}\delta) \cdot I$, it is easy to obtain the time dependence for the lattice light intensity which satisfy the adiabaticity condition:

$$I(t) = \frac{I_{max}}{(1 + \gamma t)^2} \quad (5.32)$$

In the simple model, atoms are assumed to be localized near the bottom of potential wells and the atomic c.m. motion is approximated by a thermally excited 3D harmonic oscillator. The thermal excitation of each degree of freedom is described by a Boltzmann factor $f_B^i = \exp(-\hbar\omega_i/k_B T_i)$ with T_i denoting the temperature of that degree of freedom. If the harmonic oscillator frequency decays adiabatically, the Boltzmann factor remains constant, so the oscillator temperature behaves as $T_i(t) = T_i(0) \omega_i(t)/\omega_i(0)$, approaching zero for $t \rightarrow \infty$. In the real experiment the temperature does not go to zero, because the true periodic optical potential cannot be represented by a single harmonic oscillator. The harmonic oscillator approximation breaks down when the width of the c.m. distribution becomes comparable to the spacing between optical potential wells. At this point the heating cannot be assumed negligible during the expansion and the final temperature has a nonzero value. A more realistic calculation of the final temperature expected for adiabatic expansion in a periodic potential is performed in [44] and is based on a band theory.

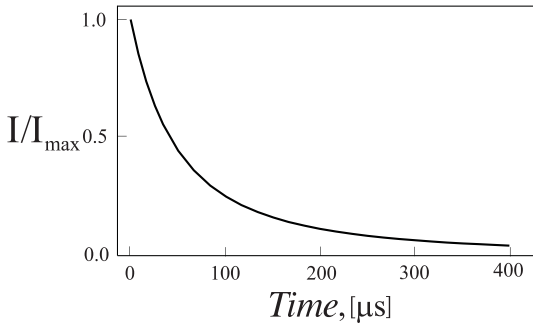


Figure 5.29: Reduction of the lattice light intensity. With the reduction rate $\gamma = 10^4 \text{ s}^{-1}$ and $t = 400 \mu\text{s}$, the optimum settings for the adiabatical cooling are reached.

We load the 3D dark optical lattice with atoms by superimposing a magneto-optical trap on the lattice volume. The MOT initially captures atoms from the pre-cooled atomic beam (see Sec. 4.4), producing a dense ($\approx 8 \cdot 10^{10} \text{ at/cm}^3$) sample of cold ($\approx 70 \mu\text{K}$) atoms in a volume of $\approx 2.57 \text{ cm}^3$. The MOT light field is then extinguished, MOT magnetic field is switched over to the lattice magnetic field and the lattice light field is turned on. The atoms equilibrate in dark lattice for 15 ms, leading to the atomic temperature of about $8.5 \mu\text{K}$, after which the adiabatic expansion is accomplished by decrease in the lattice light intensity according to Eq. 5.32 with a typical decrease rate of 10^4 s^{-1} , see Fig. 5.29. With this experimentally obtained value of the decrease rate, the adiabaticity parameter $\varepsilon \sim 0.16$ satisfy

the demand of negligible heating during the expansion. The expansion proceeds in $400 \mu\text{s}$, and is terminated when atoms are released from the lattice by rapid ($< 1 \mu\text{s}$) extinction of the lattice light. The vertical and horizontal temperature of now free atoms is measured with the improved time-of-flight method, see Sec. 5.2.9. We are able to improve the temperature in 3D dark optical lattice by a factor of ~ 3 and reach a final temperature of $2.8 \mu\text{K}$.

Chapter 6

Density Enhancement

This chapter presents our results with regard to increasing the density in a three-dimensional dark optical lattice (3D DOL). This is accomplished by successive cooling cycles in the 3D DOL and oscillation cycles in a one-dimensional far-detuned optical lattice (1D FORL). In Secs. 6.1 and 6.2 we summarize the physics of far-detuned optical lattices. In Sec. 6.3, the performance of our implementation of a 1D FORL is described. The density enhancement procedure is finally presented in Sec. 6.4.

6.1 Optical Dipole Potential

Let us briefly summarize the basic concepts of atom trapping in optical dipole potentials that result from the interaction with far-detuned light. A simple classical oscillator model can be used to derive the basic equations for the dipole potential for two-level atoms, which will be extended to multilevel atoms later on. For an atom in the light field, the electric field \vec{E} induces an atomic dipole moment \vec{p} that oscillates at the driving frequency ω . The amplitude of the dipole moment is related to the electric field by:

$$\vec{p} = \alpha \vec{E} \quad (6.1)$$

where α is the complex polarizability of an atom and depends on the driving frequency ω . The interaction potential of the induced dipole moment \vec{p} in the driving field \vec{E} is given by

$$U_{dip} = -\frac{1}{2} \langle \vec{p} \cdot \vec{E} \rangle = -\frac{1}{2\epsilon_0 c} \Re(\alpha) I \quad (6.2)$$

The field intensity is $I = 2\epsilon_0 c |\vec{E}|^2$ and the factor 1/2 results from the fact that the dipole moment is induced. The dipole force writes as

$$\vec{F}_{dip}(r) = -\nabla U_{dip}(r) = \frac{1}{2\epsilon_0 c} \Re(\alpha) \nabla I(r) \quad (6.3)$$

The dipole force is conservative and proportional to the intensity gradient of the driving field.

Considering the light as a stream of photons $\hbar\omega$, the absorption can be interpreted in terms of photon scattering in cycles of absorption and subsequent spontaneous reemission

processes. The scattering rate is given by

$$\Gamma_{scatt}(r) = \frac{P_{abs}}{\hbar\omega} = \frac{\langle \dot{\vec{p}} \cdot \vec{E} \rangle}{\hbar\omega} = -\frac{1}{\hbar\epsilon_0 c} \Im(\alpha) I(r) \quad (6.4)$$

These equations are valid for any polarizable particle in an oscillating electric field. For an atomic polarizability we consider an atom in Lorenz's model of classic oscillator. In this model an electron is considered to be bound elastically to the core with an oscillation eigenfrequency ω_0 , which corresponds to the optical transition frequency. The dipole radiation of the oscillating electron results in damping. From the equation of motion for the driven oscillation of the electron one can calculate the polarizability as:

$$\alpha = \frac{e^2}{m_e} \frac{1}{\omega_0^2 - \omega^2 - i\omega\Gamma_\omega} \quad (6.5)$$

with e elementary charge, m_e mass of electron and Γ_ω being the classical damping rate due to the radiative energy loss:

$$\Gamma_\omega = \frac{e^2\omega^2}{6\pi\epsilon_0 m_e c^3} \quad (6.6)$$

by introducing the on-resonance damping rate $\Gamma = \Gamma_\omega(\omega_0/\omega)^2$ we can write Eq.6.5 as

$$\alpha = 6\pi\epsilon_0 c^3 \frac{\Gamma/\omega_0^2}{\omega_0^2 - \omega^2 - i(\omega^3/\omega_0^2)\Gamma} \quad (6.7)$$

Neglecting saturation effects, the semiclassical calculation yields exactly the same result as a the classical one. The damping rate Γ , which corresponds to the spontaneous decay rate of the excited state, is determined by the dipole matrix element between ground and excited state:

$$\Gamma = \frac{\omega_0^3}{3\pi\epsilon_0 \hbar c^3} |\langle e|\mu\rangle g|^2 \quad (6.8)$$

For the D-lines of the alkali atoms, the classical formula of Eg.6.6 provides a good approximation to the spontaneous decay rate with a deviation of few percent. Note that Eq.6.5 is only valid in the absence of saturation effects. In the case of a FORT the saturation is very low and one can use the Eq.6.5 as an approximation for the quantum-mechanical oscillator.

In the case of large detunings and negligible saturation one can easily derive the expressions for the dipole potential and the scattering rate, see Ref. [31]:

$$U_{dip}(r) = -\frac{3\pi c^2}{2\omega_0^3} \left(\frac{\Gamma}{\omega_0 - \omega} + \frac{\Gamma}{\omega_0 + \omega} \right) I(r) \quad (6.9)$$

$$\Gamma_{scatt}(r) = \frac{3\pi c^2}{2\hbar\omega_0^3} \left(\frac{\omega}{\omega_0} \right)^3 \left(\frac{\Gamma}{\omega_0 - \omega} + \frac{\Gamma}{\omega_0 + \omega} \right)^2 I(r) \quad (6.10)$$

The above expressions are valid for any driving frequency ω , and show two resonances at $\omega = \omega_0$ and $\omega = -\omega_0$. For the case that the laser frequency is tuned relatively close

to resonance $\delta = \omega - \omega_0 \ll \omega_0$ one can apply the rotating-wave approximation and with $\omega/\omega_0 \approx 1$, the expressions 6.9 simplify to:

$$U_{dip}(r) = -\frac{3\pi c^2}{2\omega_0^3} \frac{\Gamma}{\delta} I(r) \quad (6.11)$$

$$\Gamma_{scatt}(r) = \frac{3\pi c^2}{2\hbar\omega_0^3} \left(\frac{\Gamma}{\delta}\right)^2 I(r) \quad (6.12)$$

These equations indicate that all dipole traps can be divided in two classes, red-detuned traps, where the laser is tuned below atomic resonance ($\delta < 0$) and blue-detuned traps with the laser tuned above resonance ($\delta > 0$). For red-detuned traps the dipole potential is negative and the interaction thus attracts atoms into the maximum of the light field. For blue-detuned traps the dipole potential is positive and the interaction pushes atoms out of

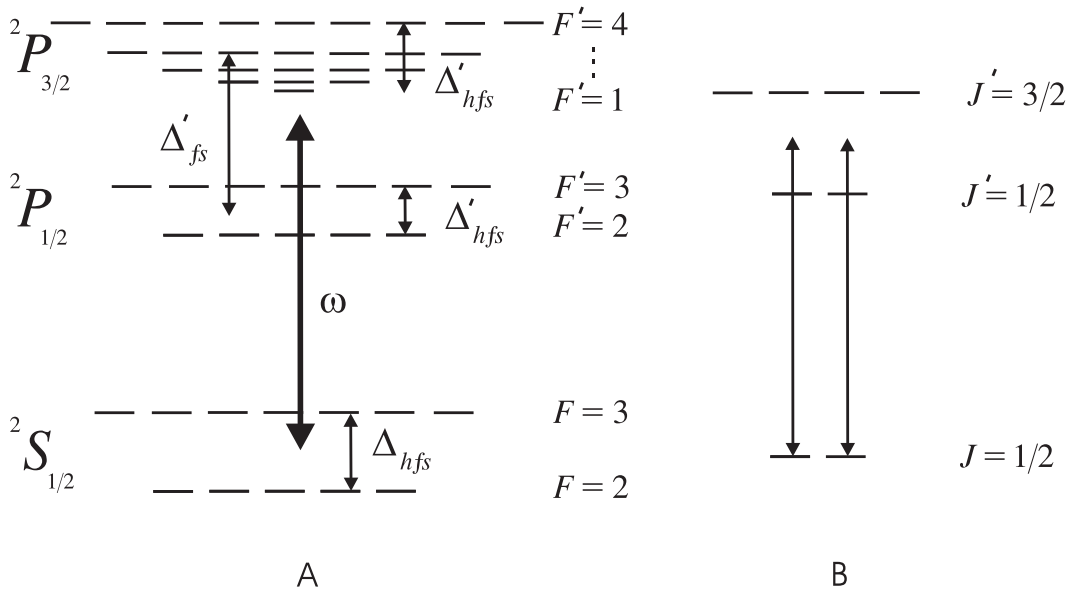


Figure 6.1: A. Level scheme of ^{85}Rb atom with full substructure. B. Reduced level scheme for large detunings in the range $\Delta'_{fs} \geq \Delta \gg \Delta_{hfs}, \Delta'_{hfs}$.

the field to the minima of the intensity. According to Eqs. 6.11, the dipole potential scales as Γ/δ , while the scattering rate scales with Γ/δ^2 . Thus, for optical dipole traps large detunings and high intensities are desirable to keep the scattering rate as low as possible. This is of interest, since spontaneous scattering events lead to heating of the atomic sample.

For a multilevel atom (as in the case of alkali atoms) the energy structure is more complicated as in the case of two-level atom, see Fig. 6.1 A. This complicated substructure should be taken in account in the calculations.

For alkali atoms, Rb for example, spin-orbital coupling in the excited state leads to the well-known D-line doublet $2S_{1/2} \rightarrow 2P_{1/2}, 2P_{3/2}$ with splitting Δ'_{fs} . The coupling to the nuclear spin adds hyperfine structure in both ground and excited states with splittings Δ_{hfs} and Δ'_{hfs} . These scale according to $\Delta'_{fs} \gg \Delta_{hfs} \gg \Delta'_{hfs}$, see Fig. 6.1 A.

In our case, all optical detunings are large compared with the hyperfine splitting of the excited state Δ'_{hfs} and the ground state Δ_{hfs} but smaller than the fine structure splitting

Δ_{fs} of the D_1 and D_2 lines (see Fig. 6.1). In this case of resolved fine structure and unresolved hyperfine structure (see Fig. 6.1 B), one may calculate the energy shift considering the atom in the spin-orbit coupling and neglecting coupling to the nuclear spin. For linear polarization and detunings $\Delta_{1,F}$ and $\Delta_{2,F}$ of the laser light from the center of the D_1 and D_2 lines, both electronic ground levels are shifted by the same amount and stay degenerate after coupling to the nuclear spin. The exact quantum-mechanical treatment of the interaction Hamiltonian for this situation results in the following expression for the dipole potential [31]:

$$U_{dip}(r) = \frac{\pi c^2 \Gamma}{2\omega_0^3} \left(\frac{2}{\Delta_{2,F}} + \frac{1}{\Delta_{1,F}} \right) I(r) \quad (6.13)$$

and for the scattering rate:

$$\Gamma_{scatt}(r) = \frac{\pi c^2 \Gamma^2}{2\hbar\omega_0^3} \left(\frac{2}{\Delta_{2,F}^2} + \frac{1}{\Delta_{1,F}^2} \right) I(r) \quad (6.14)$$

6.2 Standing Wave Red Detuned FORT

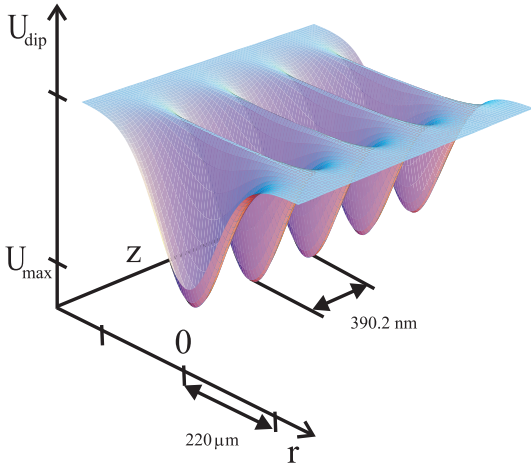


Figure 6.2: *Three-dimensional view of the standing-wave dipole potential. Axial periodicity of the potential is $\lambda/2=390.2$ nm, the extension in radial direction is much larger, some hundreds of μm .*

The intensity distribution in the standing wave formed by retro-reflecting a Gaussian laser beam has the form:

$$I(r) = \frac{4P}{\pi w^2(z)} \exp \left[\frac{-2r^2}{w^2(z)} \right] \cos^2 \left(\frac{2\pi z}{\lambda} \right) \quad (6.15)$$

where P is the power of the incident laser beam and r denotes the radial coordinate. The $1/e^2$ radius $w(z)$ depends on the axial coordinate z via $w(z) = w_0 \sqrt{1 + (\frac{z}{z_R})^2}$ with the minimum radius w_0 , called beam waist, and $z_R = \pi w_0^2 / \lambda$ denoting the Rayleigh length. In the axial direction the intensity shows the standing wave pattern, i.e., it is spatially modulated with a period of $\lambda/2$. In the radial plane the intensity distribution is caused by the Gaussian form of the laser beam. The trap depth U_0 and the scattering rate Γ_0 for atoms in the trap center ($r = z = 0$) is given by:

$$U_0 = \frac{2Pc^2\Gamma}{w_0^2\omega_0^3} \left(\frac{2}{\Delta_{2,F}} + \frac{1}{\Delta_{1,F}} \right) \quad (6.16)$$

$$\Gamma_0 = \frac{2Pc^2\Gamma^2}{\hbar w_0^2\omega_0^3} \left(\frac{2}{\Delta_{2,F}^2} + \frac{1}{\Delta_{1,F}^2} \right) \quad (6.17)$$

In the Fig. 6.2, the three-dimensional view of the red-detuned FORT potential for our experimental parameters is shown. Atoms are trapped in the antinodes¹ of the standing

¹The FORT is red-detuned from the atomic resonance ($\omega - \omega_0 < 0$)

wave, resulting in a one-dimensional lattice of "pancake-shaped" sub-traps. The name "pancake" will become obvious if one notes the different scales of the spatial axes in Fig. 6.2. The pancake-shaped microtraps are arranged in a 1D lattice structure and we will thus talk of a 1D far-off resonant optical lattice (FORL) in the following. If the standing wave is oriented along the vertical axes, the axial confinement in the trap greatly exceeds the gravitational force.

For a trapped atom, oscillating on the bottom of potential, the potential shape can be approximated as a harmonic one. From the equation of motion for a harmonically trapped particle $m\ddot{x} + kx = 0$, one can derive the oscillation frequency $\omega = \sqrt{k/m}$ for the axial and radial directions:

$$\omega_{radial} = \sqrt{\frac{4 U_0}{m w^2}} \quad (6.18)$$

$$\omega_{axial} = k \sqrt{\frac{2 U_0}{m}} \quad (6.19)$$

with $k = 2\pi/\lambda$ being the wavevector and U_0 the trap depth.

Assuming a Boltzmann distribution for the atomic population in the trap potential, we obtain a Gaussian distribution for atoms in all three dimensions. The Gaussian width σ_i of the sample in direction i is connected with the temperature of the atoms and the trap frequency by:

$$\sigma_i = \sqrt{\frac{k_B T}{m \omega_i}} \quad (6.20)$$

6.3 Characterization of the FORL

In this section we discuss our experimental realization of a far-detuned standing wave dipole trap. We describe the temporal evolution of the atomic sample in the FORL and show temperature and radial vibrational frequency measurements.

6.3.1 Experimental Realization

Three-dimensional confinement in a standing wave is only accomplished with red-detuned trapping light. To efficiently load the dipole trap and to obtain a high number of atoms, the trap potential should be deeper than the temperature of the atomic sample in the MOT (typically about $100 \mu K$). The available optical power of $180 mW$ and the need of a reasonable volume of the trap ($250 \mu m$) determines the maximum detuning of $181 GHz$ from the atomic resonance of the ^{85}Rb D2-line. With this experimental settings we can calculate the resulting potential depth of $U_0 = 173 \mu K$ with corresponding axial and radial frequencies of $\nu_{ax} = 236 kHz$ and $\nu_{ax} = 166 Hz$, see Tab. D.1.

The optimal loading conditions requires a good overlap of the MOT cloud and the dipole trap. In our set-up, we first perform the magnetic field compensation procedure (see Sec. 2.2), align the power and polarization of MOT beams to compensate the radiation pressure inside the MOT and finally optimize the position of the FORL by monitoring the number of trapped atoms with a CCD camera. A picture of the atomic cloud trapped in

the FORL is shown in Fig. 6.6. It is irradiated by a resonant beam with an exposure time of $500 \mu s$, $40 ms$ after shutting off the MOT. The pictures, obtained with the CCD camera are used to quantify the fluorescence and the number of trapped atoms.

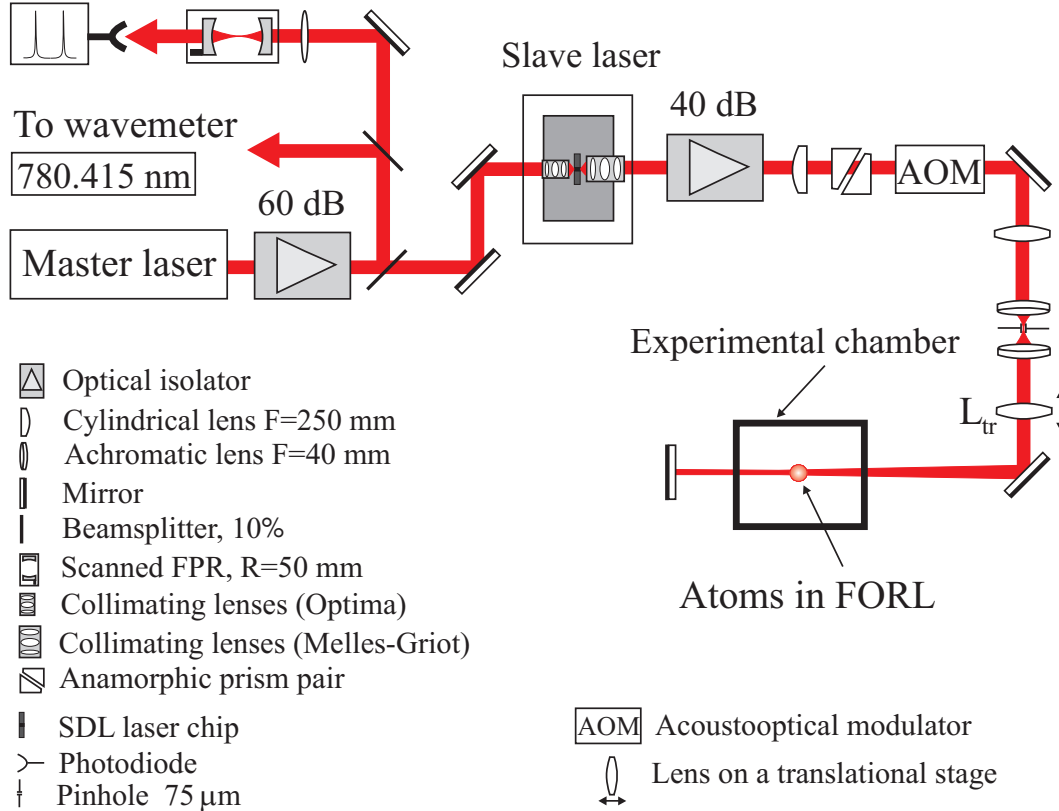


Figure 6.3: Scheme of the optical setup for our FORL.

The following part of this subsection describes the optical setup for our FORL, which is depicted in Fig. 6.3. A tapered amplifier diode laser based system (see Sec. 3.2) with the single-mode output power of 180 mW was used as a light source for the FORL. The output of the grating-stabilized master laser (see Sec. 3.1.1) is controlled with a confocal Fabry-Perot interferometer to assure that the laser is running single-mode (this is essential for the performance of the FORL because otherwise intensity fluctuations may cause undesired parametric heating [65]). The output wavelength (detuning of the FORL is typically 0,4nm) is controlled with a self-made Michelson-interferometer based "wavemeter". Leaving the tapered amplifier, the laser beam passes through an optical isolator, is collimated, deflected by an AOM, mode-filtered and finally send into the experimental chamber. An optical isolator is necessary since the tapered amplifier is very sensitive to back-reflected light (see Sec. 3.2.1) and we use a standing wave configuration for our FORL. An AOM is needed since we have to modulate the trap depth of the FORL.

Originally, this AOM was positioned between master and slave lasers, but it was noticed that the tapered amplifier chip is very sensitive (see also notes in Sec. 3.2.1) concerning the optical injection. So for the operational reliability we had to place the AOM after the amplifier. Unfortunately, deflecting a laser beam on the acoustic wave disturbs the

wavefront of the light beam. Since for the performance of the FORL a good quality Gaussian beam is necessary, we filtered the laser beam with a spatial filter. The FORL is built in the vertical direction in order to support atoms against gravity. The lens L_{tr} (Fig. 6.3) with $F=300$ mm is positioned such that the beam waist of the focused laser beam is positioned on the back-reflection mirror. This lens is mounted on a translational stage and used for a fine adjustment of the beam waist position in order to compensate the intensity losses on the windows of the vacuum chamber.

6.3.2 Lifetime Measurements

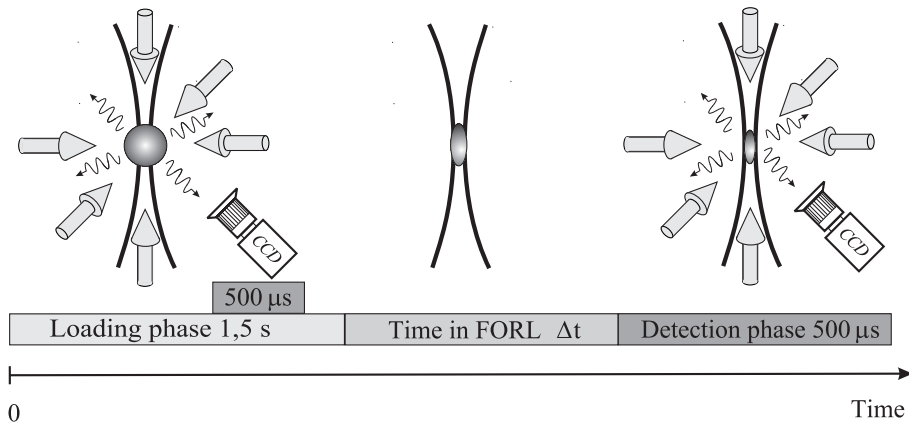


Figure 6.4: *Experimental sequence for measurement of the FORL lifetime. The sequence consist of three phases: loading phase, free-developing phase and detection phase. For the detection a resonant light is switched on. To normalize the measured number of atoms we used a signal from MOT, collected during the loading phase.*

For measuring the lifetime of the FORL we used the following sequence depicted in Fig. 6.4. The FORL is loaded directly from the MOT for 1,5 seconds. The MOT repumper beam is switched off shortly (2 ms) before the cooling laser for the MOT is extinguished. This procedure prepares all atoms in the $F = 2$ ground state. After MOT extinction, the atoms remain trapped by the dipole potential and after a variable time Δt , a picture of the atomic cloud is taking by switching on the light of MOT for $500\mu s$. During this short exposure time, the fluorescence from atoms which remained in the FORL is collected by the CCD camera. From the signal of the CCD camera, the number of atoms remaining in the FORL after a time Δt is calculated. The time interval Δt is increased until the number of atoms, remaining in the FORL can be no longer detected by the CCD camera. The number of atoms observed after a delay time Δt is normalized to the number of atoms initially prepared by the MOT and an average over 8 measurements is produced for each data point.

The temporal evolution of FORL population is shown in Fig. 6.5. At trapping times exceeding $70 ms$, an exponential decay of the trap population occurs due to collisions with background atoms. For trapping times below $70 ms$, the decay is faster than exponential

due to additional collisions between cold atoms only occurring at sufficiently high densities. The trap decay is described with Eq. 6.21², taking in account both loss processes:

$$N(t) = N_0 \cdot \frac{(1 - \xi)e^{-\Gamma t}}{1 - \xi e^{-\Gamma t}} \quad (6.21)$$

with $N(t)$ being the time-dependent number of atoms in the trap, N_0 the maximum atom number in the beginning of the measurement, Γ the decay rate due to the hot background gas, and $\xi \in [0, 1]$ a parameter comparing the rate for cold collisions with Γ .

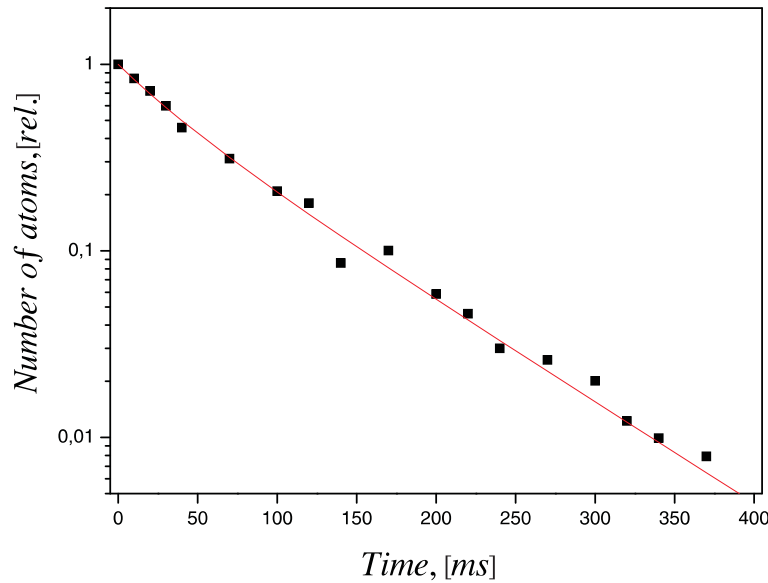


Figure 6.5: Decay of the dipole trap, created with the diode laser system. The scale of y-axes is logarithmical. The fit (solid line) results from the model of non-exponential decay, see Eq. 6.21, with $1/\Gamma = 80$ ms decay time and $\xi = 0.36$. The trap depth was $173 \mu\text{K}$ and the detuning $\delta = 181.7 \text{ GHz}$.

The parameter Γ is a measure for the vacuum conditions inside the experimental chamber. With the typical values for the pressure in our experimental chamber on the order of $5 \cdot 10^{-9} \text{ mbar}$, we expect decay times of about 0.6 s ³, whereas in the experiment we find $\tau = 1/\Gamma$ to be equal to 80.39 ms . We believe, that the reason for this large discrepancy in the values for τ , results from the limited spectral quality of the laser light used for the dipole trap. Namely, the fluorescence spectrum of the SDL chip, used as an amplifier, is some nanometers broad. For optimal amplification, the center of this spectrum is shifted by changing the temperature of the chip in the vicinity of the amplified wavelength. The detuning of the dipole trap from the atomic resonance was set to 0.37 nm , so there existed a non-vanishing component of light at the resonant wavelength. The spectral density of the fluorescence of the diode chip varied and sometimes we could see a weak fluorescence

²see Appendix C.8 for the derivation

³As a rule of thumb, the lifetime of a dipole trap is $\approx 1 \text{ s}$ at a pressure of the $3 \cdot 10^{-9} \text{ mbar}$ in the vacuum chamber. The expected lifetime a MOT at the same pressure is a factor of three larger because of the larger cross sections for collisional loss at lower trap depth [31].

from the FORL (at a detuning of 0.37 nm, the fluorescence due to the off-resonant excitation is not detectable with our CCD system). These observations support the assumption that the observed heating in our dipole trap is due to a small part of the laser light being resonant with the atomic transition.



Figure 6.6: Fluorescence of the atoms trapped in the FORL.

Despite of the fact that our trap lifetime is limited due to residual resonant excitation, we briefly wish to mention other possible trap loss mechanisms: cold-body collisions, hyperfine changing collisions and photoassociation.

Cold two-body collision losses can be caused by several processes: Trap losses due to collisions involving atoms in an electronically excited state, losses due to the hyperfine changing collisions, and losses due to photoassociation. We assume that the main loss mechanism in our dipole trap is caused by the collisions of atoms in an electronically excited state, because of the non-vanishing on-resonant part in the trap light.

Hyperfine changing collisions [58] can also lead to losses in a dipole trap. This loss process arises if one of the colliding atoms is in the upper hyperfine state. The energy difference in this case is equal to 3.1 GHz , which is much higher than the trap depth (typically some MHz). In our experiment, the atoms are initially prepared in the $F = 2$ state. However, due to spontaneous scattering events, they can be optically pumped into the upper $F = 3$ state. To exclude the hyperfine changing collisions, we applied an additional weak depumping laser resonant with the $F = 3 \rightarrow F' = 3$ transition, yielding a low population of the upper hyperfine state. Despite of the depumping beam, the lifetime of the trap does not change which indicates that hyperfine changing collisions are not responsible for the trap losses.

A third two-body loss mechanism is connected with photoassociation [70], when atoms build a stable molecule which leaves the trap. Two colliding atoms in the ground state can create a molecule in the excited state by absorbing a photon from the trap light. This process has a resonance behavior because it depends on the narrow lines of the molecular potentials. The photoassociation spectrum of *Rb* was studied in detail in [52].

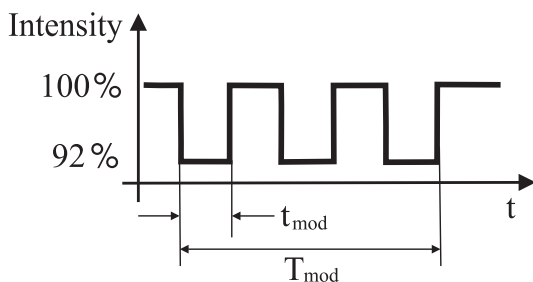


Figure 6.7: Modulation of the trapping laser intensity for the measurement of the vibrational frequency in the dipole trap. Laser intensity is modulated over a time interval $T_{\text{mod}} = 30\text{ ms}$ with a variable period of $2t_{\text{mod}}$.

Technical noise and intensity fluctuations of the trapping light are further possible reasons for heating in a dipole trap, see [65, 27]. Technical noise can influence the stability of the trap position. The reason for the position noise can be the beam-direction instability of a laser or instability of optical mountings (arising from acoustic noise or mechanical jitter) used in the optical setup. Intensity fluctuations with twice the trap frequency can lead to strong heating losses from the trap, so-called parametrical heating. The influence of the intensity and beam-pointing stabilities on the heating rate of the trap is studied in [65] in detail.

A typical picture of atoms trapped in our FORL is shown in Fig. 6.6. The sample shown in this picture has $\sigma_r \approx 100 \mu\text{m}$ in radial and $\sigma_z \approx 900 \mu\text{m}$ in axial direction.

In the table D.1 in App D we have combined the parameters of our dipole trap. The values are calculated according to Eqs. 6.18, 6.15, 6.13, 6.14:

6.3.3 Measurement of the Radial Vibrational Frequency of the FORL

To verify the calculated value for the radial vibrational frequency of the FORL, we measured this parameter in the experiment. We measure the trap filling factor as a function of the trap depth modulation frequency. For this purpose we modulated the intensity of the FORL laser beam using an AOM. We decreased the trapping laser intensity by 8% for a variable time t_{mod} and checked the number of atoms remaining in the trap after a modulation time T_{mod} , for details see Fig. 6.7. The experimental sequence for this measurement is depicted in Fig. 6.8.

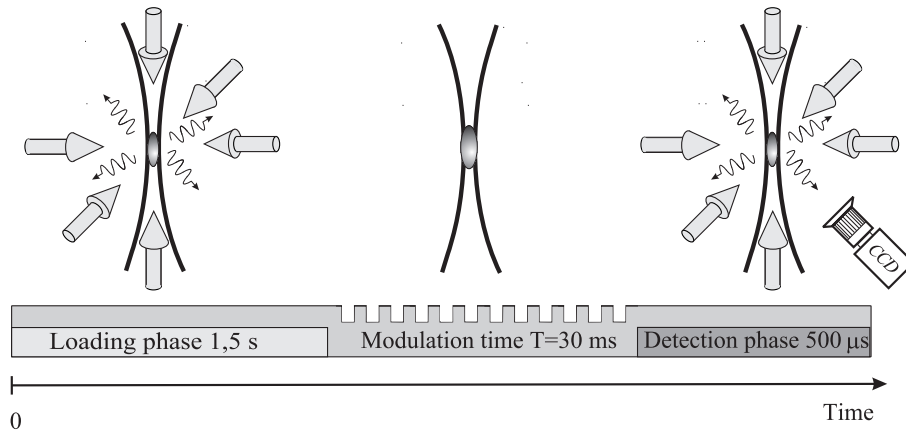


Figure 6.8: *Measuring scheme for the observation of the radial vibration frequency of atoms in the FORL. After a loading phase of 1.5 s, laser intensity is modulated for $T_{mod} = 30 \text{ ms}$ following by the detection phase.*

One expects a behavior typical for a parametric resonance, i.e., the heating rate for the atoms in the trap and, hence, the losses from the trap are maximal when the frequency of the intensity variation equals twice the frequency of the atomic oscillations in the unperturbed trap. The result of our measurement is presented on the Fig. 6.9. The number of trapped atoms is reduced by a factor more than 5 for a modulation period of 3.4 milliseconds, which well corresponds to twice the frequency of radial oscillations in the trap $2\omega_{rad}$. According to the calculation, this value should be 3.22 ms, which shows a good agreement between calculated and measured parameters.

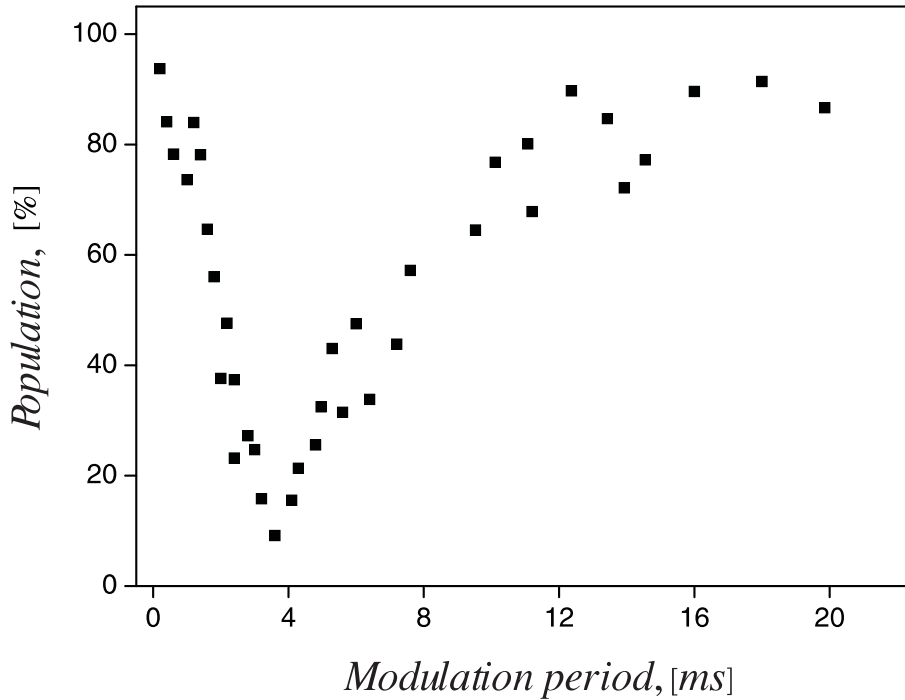


Figure 6.9: Results of the measurement of the radial vibrational frequency in the FORL. The population in the unperturbed trap is set to 100%. A pronounced minimum at the modulation period of 3.4 ms corresponds to the parametrical heating by twice the trap frequency.

6.4 Parametric Density Enhancement

Optical lattices are typically loaded from a magneto-optical trap (MOT), where densities above several 10^{11} at/cm^3 are unattainable due to radiative repulsion and light-assisted collisions [59, 45]. This limits the filling fraction in an optical lattice to below 5%. Several experimental approaches have been taken to overcome this density limit [22, 36]. In these experiments, a 3D far-detuned optical lattice was used for confinement and the MOT molasses light for cooling. An adiabatic compression sequence was implemented to increase the atomic density inside the far-detuned optical lattice with the result that peak densities up to $6 \cdot 10^{11} \text{ at/cm}^3$ were achieved [22].

In this thesis, we investigate another experimental scheme for density enhancement in an optical lattice. We implement a 3D dark optical lattice, which provides efficient cooling and trapping of atoms with the advantage of permitting a significantly reduced elastic photon scattering rate (see Sec. 5.3). The density enhancement is based on adiabatic compression of atoms inside the additional optical potential of a 1D FORL. We superimposed the 1D FORL light field with the three-dimensional dark optical lattice as shown in Fig. 6.10. The 1D FORL trap is made from a vertically oriented, linearly polarized, retroreflected beam (see Secs. 6.2, 6.3.1). The following three-step scheme (see Fig. 6.11) was implemented to obtain a density enhancement in the DOL:

- in the first step, atoms are confined in a superposition of the vertically oriented 1D FORL (red curve in Fig. 6.11) and the 3D dark optical lattice (blue curve in Fig.

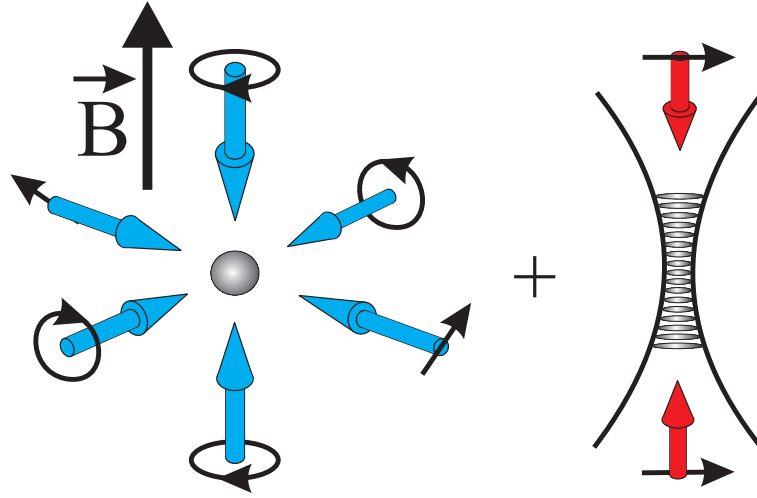


Figure 6.10: Configuration of the light fields for the experiment to increase the density in the FORL. Left: a configuration of the 3D dark optical lattice, as described in 5.3.1, right: a standing wave dipole trap (FORL) configuration, see Sec. 6.2.

6.11), which cools the trapped atoms to a temperature on the order of $10 \mu K$ (see Fig. 6.11, Step 1).

- in the second step, the dark optical lattice is switched off adiabatically⁴, the exact switching procedure is depicted in Fig. 6.13. The atoms are now subjected to a dipole potential only and, therefore oscillate in the "pancake-shaped" microtraps at each site of the FORL. Due to the difference in the steepness of the radial and axial potentials, the oscillation frequencies in these directions are also very different, see Tab.D.1. In the low-confinement (radial) direction the oscillation frequency is measured to be 155 Hz. In the time $T_k = 1/4 \cdot T_0 = 1/4\nu = 1.6 ms$ (see Fig. 6.12) atoms perform a quarter of periodic oscillation, that means they will collect in the potential minimum for a short time interval (see Fig. 6.11, Step 2)⁵.
- in the third step, the 3D DOL is reactivated when the atoms arrive at the potential minimum of the 1D FORL in order to freeze their oscillatory motion and trap the atoms in the DOL wells at $10 \mu K$ temperature again (see Fig. 6.11, Step 3).

The experimental sequence of this scheme is shown in Fig. 6.14. We start the experimental cycle by trapping 10^9 Rb atoms at 10^{11} atoms cm^{-3} in a MOT. After turning off the MOT, atoms are trapped by the 1D FORT. In 30 ms the trapped atoms equilibrate and the untrapped atoms are removed by gravity⁶. A cylindrically symmetric sample of atoms is thereby prepared. Next, we switched on the three-dimensional dark optical lattice, and

⁴The adiabaticity is needed to additionally cool the atoms, see Sec. 5.3.4

⁵This statement uses the assumption that potential shape is harmonic one. Therefore, all atoms have the same oscillation frequency. Substantively, potential of a FORL has an $exp(r^2)$ -form and can be approximated by a harmonic potential only in the vicinity of the potential minimum.

⁶This time is needed to let the non-trapped atoms to escape from the interaction region, otherwise they will disturb the detection process.

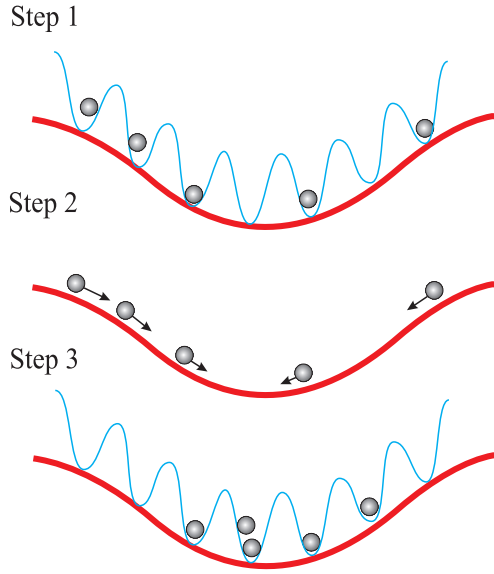


Figure 6.11: Scheme for the density enhancement in the FORL via parametrical modulation of the three-dimensional dark optical lattice.

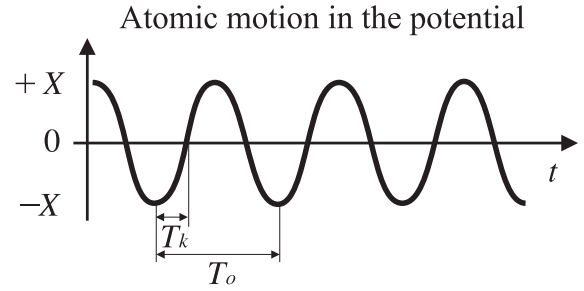


Figure 6.12: Harmonic oscillation of an atom in the FORL potential.

the atoms are localized and cooled down to a temperature of $\sim 10 \mu K$. Subsequently, the optical potential of the dark optical lattice is reduced adiabatically 1000-fold in $400 \mu s$, providing further cooling down to $\sim 3 \mu K$ (see Sec. 5.3.4), and finally the 3D DOL is completely extinguished. The atoms are now confined in about 2500 pancake-shaped microtraps with $250 \mu m$ radius and 150 nm thickness at a temperature of $3 \mu K$. The pancake dipole force resulting from the Gaussian transverse profile of the 1D FORT leads to a collapse of the atomic distribution towards the trap centers. In harmonic approximation, the atoms will

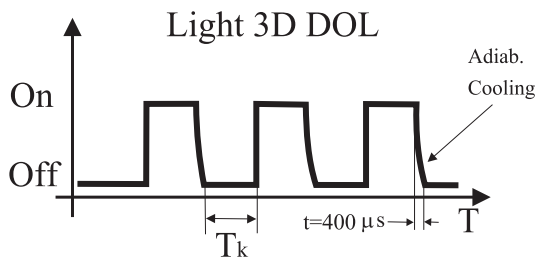


Figure 6.13: Light modulation of the dark optical lattice for the density enhancement procedure.

accumulate at the potential minima after one-quarter of oscillation period in the radial potential of the FORL. The time to peak compression is 1.6 ms , then the 3D DOL is switched again to cool the collapsed atoms. We modulate the potential of the dark optical lattice according to the previously described procedure 10 ms long (striped area of 3D DOL in Fig. 6.14). At the end of the modulation phase we adiabatically turned off the dark optical lattice and release the compressed atoms into the FORL potential. Finally, we detect the atoms in the FORL by recording their resonant fluorescence. The atomic density is determined from the fluorescence measurement and is compared with the density which is achieved without the modulation of the dark optical lattice potential.

To show that the expected density enhancement occurs at the predicted fraction of $1/4$

of the oscillation time in the radial potential of the FORL, we vary the evolution time T_k that atoms spend inside the 1D FORL⁷, see Fig. 6.14, and measure the corresponding density increase. Figure 6.15 plots the relative peak density increase as a function of the evolution time in the 1D FORL. The time when the maximum compression is reached is 1.55 ms , which corresponds well with the calculated oscillation time of $T_0/4 = 1.61 \text{ ms}$ (see Tab. D.1) and the experimentally obtained value of the radial oscillation time $T_0/4 = 1.7 \text{ ms}$ (see Sec. 6.3.3). We achieve a peak enhancement factor of four. The corresponding peak density is calculated from the fluorescence signal to be $1.2 \cdot 10^{12} \text{ at/cm}^3$ and the phase-space density is $1/140$.

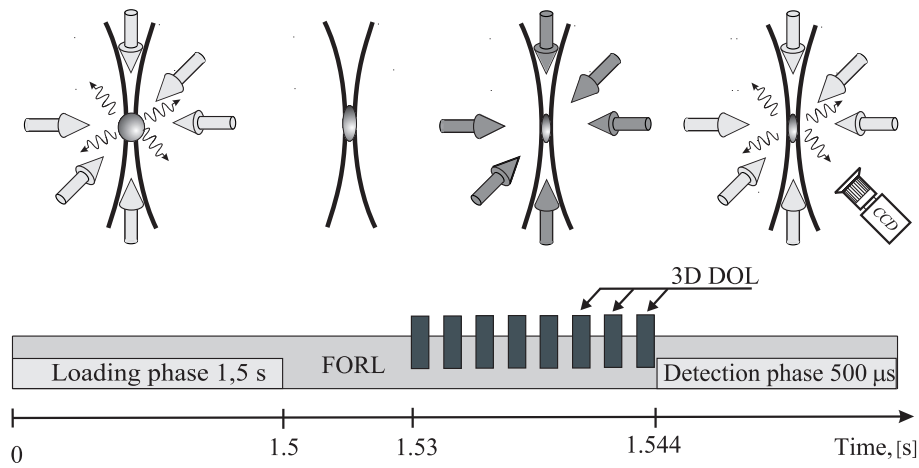


Figure 6.14: *Measuring scheme for the density enhancement in the FORL via parametrical modulation of the three-dimensional dark optical lattice.*

The dependence of the enhancement factor on the evolution time in the FORL potential is relatively broad as can be seen in Fig. 6.15. The reason is that the dipole potential has a Gaussian form and its approximation with the harmonic potential is only correct in the vicinity of the potential minimum. In our experiment, the atoms are distributed at positions inside the potential where this approximation is not valid. This leads to anharmonicities in the evolution phase inside the FORL. Due to this fact, in the compression phase, atoms starting at different positions arrive at the potential minimum not exactly at the time T_K .

We expected a higher efficiency of our scheme than the experimentally observed four-fold density enhancement. The reason for the observed limitation of the enhancement factor is the technical limitation of the 1D FORL. As already mentioned, the trap lifetime $\tau = 80 \text{ ms}$ is greatly reduced due to the on-resonant component in the trapping light. The typical duration of the enhancement procedure is about 50 ms , so that at the end of the enhancement cycle approximately half of the atomic population is lost. The improvement can be reached by using another laser source for the FORL, which does not provide any resonant components in its emission spectrum, for example a Ti-Sa laser. After eliminating

⁷If T_k is shorter than $400 \mu\text{s}$, the time during the 3D DOL is "on" was set to $400 \mu\text{s}$ in order to provide cooling for the atoms.

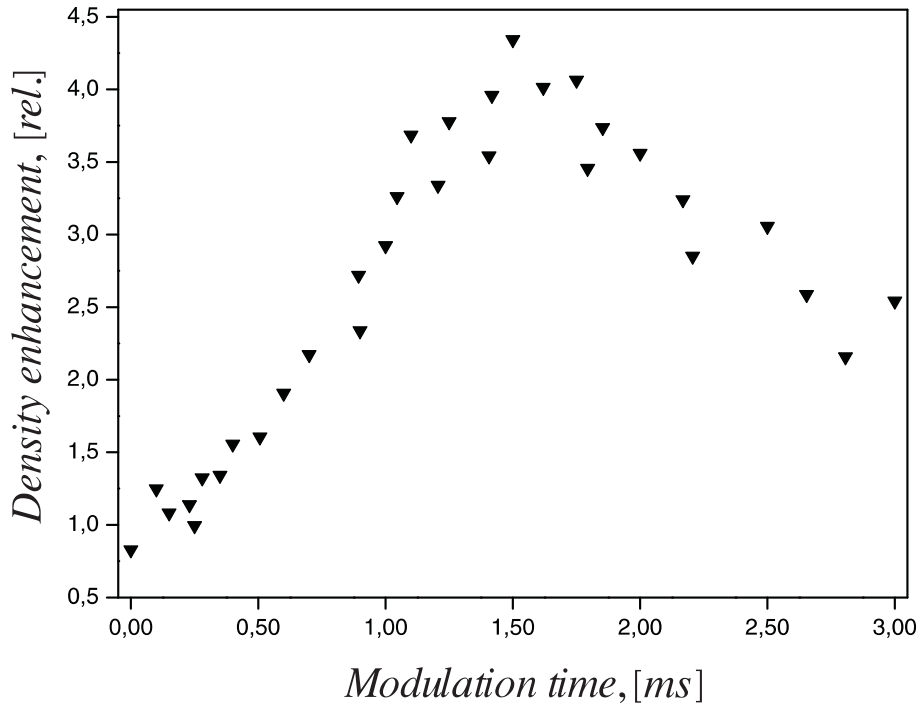


Figure 6.15: *Experimental results of the density enhancement. An enhancement factor of 4 is achieved at the modulation time $T_k \sim 1.6$ ms.*

this experimental problem we should achieve an overall enhancement of more than one order of magnitude, the corresponding peak density would be on the order of $2.4 \cdot 10^{12} \text{ at/cm}^3$. The achieved phase-space density of $1/140$ could be further improved by implementation of Raman sideband cooling inside the 1D FORL [35] and subsequent adiabatic cooling of the atoms down to the recoil limit by slowly reducing the FORL intensity. In order to approach a phase space density $\rho \approx 1$ at a density of $n = 2.4 \cdot 10^{12} \text{ at/cm}^3$ the temperature needs to be reduced from $10 \mu\text{K}$ to about half of a μK .

Appendix A

Notation and Definitions

Parameter	Definition	Description
ω_0	$\omega_0 = \omega_f - \omega_i$	angular frequency of the atomic transition
ω_L		laser frequency
Γ	$\Gamma = 1/\tau$	natural width of the atomic transition
δ	$\delta = \omega_l - \omega_a$	detuning between laser frequency and atomic transition
ω_1	$\omega_1 = -edE_0/\hbar$	Rabi frequency
s_0	$s_0 = 2(\omega_1/\Gamma)^2$	on-resonance saturation parameter
s	$s = s_0/(1 + (2\delta/\Gamma)^2)$ $= \omega_1^2/2(\delta^2 + (\Gamma/2)^2)$	off-resonance saturation parameter
Δ	$\Delta = \omega_1^2/(4\delta)$	light shift
ω_{rec}	$\omega_{rec} = k^2/2M$	recoil frequency
ω_{vib}	$\omega_{vib} = 2\text{sqr}t{\Delta\omega_{rec}}$	vibrational frequency
Π_{exc}	$\Pi_{exc} = s/(2(1 + s))$	excitation probability
Γ'	$\Gamma' = \Pi_{exc}\Gamma$	power-broadened linewidth
T	$T = M\langle v^2 \rangle/k_B$	temperature
T_{dop}	$T_{dop} = \hbar\Gamma/2k_B$	Doppler temperature (Doppler limit)
T_{rec}	$T_{rec} = \hbar^2k^2/Mk_B$	recoil temperature (recoil limit)
η	$\eta = E_{rec}/\hbar\omega_{vib}$	Lamb-Dicke factor

Table A.1: *Definitions.*

Appendix B

Rb Atom Data

Rubidium¹ was discovered by the German chemists Robert Bunsen and Gustav Kirchoff in 1861 in Heidelberg while carrying out a spectral analyze of samples of the mineral lepidolite ($KLi_2Al(Al, Si)_3O_{10}(F, OH)_2$). The sample produced a set of deep red spectral lines they had never seen before. Bunsen was eventually able to isolate samples of rubidium metal. Today, most rubidium is obtained as a byproduct of refining lithium.

atomic number	37
atomic weight	85,4678 <i>a.m.u.</i>
number of isotopes (including nuclear isomers)	30
isotopes mass range	71 → 101
estimated crustal abundance	$9,0 \cdot 10^{-1} mg/kg$
estimated oceanic abundance	$1,2 \cdot 10^{-1} mg/kg$
melting point	312,2K
boiling point	961K
thermal conductivity	58,2W/(m · K)@300K
thermal expansion coefficient	$90 \cdot 10^{-6} K^{-1}$
density	1532kg/m ³ @293K
electrical resistance	$12,5 \cdot 10^{-8} \Omega m @ 298K$

Table B.1: *Physical properties of Rb. The data is from [25].*

Rubidium is a glittering silver-white colored metal which is burning in the air and actively reacting with water. Rubidium and its compounds are mostly used for scientific investigations and have little commercial significance. In industrial applications Rubidium is used in vacuum tubes as a getter, a material that combines with and removes trace gases from vacuum tubes. It is also used in the manufacture of photocells and in special glasses. Rubidium forms no known minerals in which it is the predominant metallic constituent. It occurs mainly as a replacement for potassium, especially in minerals formed late in the crystallization of pegmatites. Some of the common rubidium compounds are: rubidium

¹from the Latin word *rubidius* - deepest red, the element was named due to the color of its fundamental spectral line

chloride (RbCl), rubidium monoxide (Rb_2O) and rubidium copper sulfate ($Rb_2SO_4 \cdot CuSO_4 \cdot 6H_2O$). A compound of rubidium, silver and iodine, $RbAg_4I_5$, has interesting electrical characteristics and might be useful in thin film batteries.

The natural mixture of Rubidium consists of two isotopes : ^{85}Rb and ^{87}Rb , see tableB.2.

Isotope	^{85}Rb	^{87}Rb
Abundance,%	72,17	27,83
Nuclear spin I	5/2	3/2
Decay time, $T_{1/2}$	stable	$4,9 \cdot 10^{10} years$
gyromagnetic ratio	$2,5828 \cdot 10^7 rad/(T \cdot s)$	$8,7532 \cdot 10^7 rad/(T \cdot s)$

Table B.2: *Rb isotopes data, taking from [25]*

The atomic element for investigations performed in this thesis is ^{85}Rb . All experiments were carry out with the natural mixture of these two isotopes. The choice of ^{85}Rb was made because of the signal amplitude in experimental data and spectroscopy for laser stabilization. Both isotopes have similar electronic structure. The electronic structure of ^{85}Rb and the transitions used in our experiments are shown in Fig. 5.14. Table B.3 shows the essential data concerning laser cooling parameter of this isotope.

Data	Value
ground state term	$5S_{1/2}$
ionization energy	$4,177eV$
$\lambda_{air}(5^2S_{1/2} \longrightarrow 5^2P_{3/2}), nm$	780,027
$\lambda_{air}(5^2S_{1/2} \longrightarrow 5^2P_{1/2}), nm$	794,760
Saturation intensity $I_s(5^2P_{3/2}), (mW/cm^2)$	1,64
Saturation intensity $I_s(5^2P_{1/2}), (mW/cm^2)$	1,4
$\tau(5^2P_{3/2}), ns$	26,63
$\gamma/2\pi(5^2P_{3/2}), MHz$	5,98
$\gamma/2\pi(5^2P_{1/2}), MHz$	5,4
$\omega_{rec}/2\pi, kHz$	3,86
Capture temperature T_c, mK	222,12
Doppler temperature $T_d, \mu K$	143,41
Recoil temperature $T_r, \mu K$	0,37

Table B.3: *Essential laser cooling parameters of ^{85}Rb*

In the Table B.4 the temperature dependance of the rubidium vapor pressure is listed. The data was used for adjustment of the oven temperature and atomic flux calculations. The intermediate values can be obtained using the formulas.

T(°C)	679,4	514,9	387,9	297,5	229,5	176,4	133,8	98,7	69,3	44,3	23,1
p_{vap} (torr)	760	100	10	1	10^{-1}	10^{-2}	10^{-3}	10^{-4}	10^{-5}	10^{-6}	10^{-7}

Table B.4: Atomic vapor pressure vs. temperature. Data was taken from [46].

B.1 Landè factors

Interaction of an external magnetic field and an atom disturb the energy levels of the atom and leads to rescission of degeneracy of the magnetic sublevels. The interaction term in the Hamiltonian due to the Zeeman effect is $H_B = -\vec{\mu} \cdot \vec{B}$. The energy shift is $\Delta E = g_F \mu_B m_F B$. With $\mu_B = -e\hbar/2mc$ Bohr magneton, m_F magnetic sublevel, B external magnetic field strength and g_F Landè factor. The Landè factor consists of

$$g_F = g_J \left\{ \frac{F(F+1) + J(J+1) - I(I-1)}{2F(F+1)} \right\} \quad (\text{B.1})$$

with $F = I \oplus J$. With $J = L \oplus S$ and $g_l = g_s/2 = 1$ the g_J factor is

$$\begin{aligned} g_J &= g_l \left\{ \frac{J(J+1) + L(L+1) - S(S-1)}{2J(J+1)} \right\} + g_s \left\{ \frac{J(J+1) + S(S-1) - L(L+1)}{2J(J+1)} \right\} = \\ &= 1 + \frac{J(J+1) + S(S-1) - L(L+1)}{2J(J+1)} \end{aligned} \quad (\text{B.2})$$

Landè g-factors for ^{85}Rb levels of interest are listed in the tableB.5

F	$5P_{3/2}$ g_F	$5P_{1/2}$ g_F	$5S_{1/2}$ g_F
4	1/2		
3	7/18	1/9	1/3
2	1/9	-1/9	-1/3
1	-1		

Table B.5: Landè g- factors of ^{85}Rb

Appendix C

Nonlinear Trap Losses

Measurements show that at high trap densities, in the beginning of the decay process the trap losses are not linear, changing over in the linear regime. These additional losses are generated by two-body collision processes and scaled linear with the square of the trap density and can be included as an extension into the linear loss model:

$$\dot{N}(t) = R - \Gamma N(t) - \beta \int n^2(r) d^3r \quad (\text{C.1})$$

Since a modified exponential decay is expected, one looked for the solution for the trap decay (R=0, no loading processes) in the form:

$$N(t) = N_0 e^{-\Gamma t} \Phi(t) \quad (\text{C.2})$$

Inserting C.2 into the C.1 yields $\dot{\Phi}(t) = \Phi^2(t) \cdot f(t)$ with $f(t) = -\beta N_0 e^{-\Gamma t}$, where $n(r) = n(t)e^{-(r/a)^2}$, $n(t=0) = n_0$ and $N(t) = \int n^2(r) d^3r$ were considered. Now we define:

$$g(t) \equiv \exp\left(-\int_{t_0}^t f(s)\Phi(s)ds\right) \quad (\text{C.3})$$

this function has the property $g''/g' = f'/f$. With $g' = \alpha_0 e^{-\Gamma t}$ and $g = \alpha_2 + \alpha_1 e^{-\Gamma t}$ one gets:

$$\Phi(t) = \frac{1}{\alpha_3 e^{-\Gamma t}} \left(\alpha_4 - \frac{\alpha_0 e^{-\Gamma t}}{\alpha_1 e^{-\Gamma t} + \alpha_2} \right) \quad (\text{C.4})$$

For $t \rightarrow \infty$, Φ has to be final, so $\alpha_4=0$ and we can reform Eg. C.4 as $\Phi = (A e^{-\Gamma t} + B)^{-1}$ with $A = \alpha_1 \alpha_3 / \alpha_0 = -\beta N_0 / \Gamma$. Considering $N(0) = N_0$ and therefore $\Phi(0) = 1$ we get $B = 1 + \beta N_0 / \Gamma$ and for N :

$$N(t) = N_0 \frac{e^{-\Gamma t}}{1 + \frac{\beta N_0}{\Gamma} - \frac{\beta N_0}{\Gamma} e^{-\Gamma t}} \quad (\text{C.5})$$

with $N_0 = n_0(\sqrt{\pi}a)^3$ being the steady state population and

$$n_0 = \sqrt{\frac{2\Gamma^2}{\beta^2} + \frac{8R}{\beta}(\sqrt{2\pi}a)^3} - \frac{\sqrt{8}\Gamma}{2\beta} \quad (\text{C.6})$$

being the corresponding steady state peak density in the ensemble. Introducing the ratio of the quadratic losses to the total losses $\xi \in [0, 1]$:

$$\xi = \frac{\beta n_0}{\beta n_0 + \sqrt{8}\Gamma} = \frac{\gamma - \Gamma}{\gamma + \Gamma} \quad (\text{C.7})$$

with $\gamma = \Gamma + 2\beta N_0 = \sqrt{(\Gamma/2)^2 + R\beta} = \Gamma(1 + \xi/1 - \xi)$ we can write the solution for trap decay C.5 as

$$\frac{N(t)}{N_0} = \frac{(1 - \xi)e^{-\Gamma t}}{1 - \xi e^{-\Gamma t}} \quad (\text{C.8})$$

During the loading process, the inelastic collisions play only a role at high trap densities, but never at the beginning of the loading, when the density is relatively moderate, thus $\dot{N}(0) = R$, and for the trap loading we get

$$\frac{N(t)}{N_0} = \frac{1 - \xi e^{-\gamma t}}{1 + \xi e^{-\gamma t}} \quad (\text{C.9})$$

Appendix D

Calculation of the peak-density in the FORL

The atomic density inside a standing-wave dipole trap is not constant. It varies from a microtrap to microtrap and is maximal in the focus of the forming laser beam. Inside each microtrap, the density reaches its maximum value in the middle of a microtrap and decreases to its periphery. The Gauss distribution describes the density distribution along the beam axis z :

$$\frac{N(z)}{N} = \frac{1}{\sigma_F \sqrt{2\pi}} \exp\left(-\frac{z^2}{2\sigma_F^2}\right) \quad (\text{D.1})$$

with σ_F being the width of the intensity distribution along z -axis and N the total number of trapped atoms. Taking in account that in a standing-wave trap, atoms are confined in the antinodes, whose displacement is $\lambda/2$ from each other, we replace the continuous variable z with the quantized one $i \cdot \lambda/2$. The distribution takes the form:

$$\frac{N_i}{N} = \frac{1}{2\sigma_F \sqrt{2\pi}} \exp\left(-\frac{1}{2} \left(\frac{i\lambda}{2\sigma_F}\right)^2\right) \quad (\text{D.2})$$

Inside a single microtrap, the density is also distributed according to the Gauss formula. Under assumption that in the x and y directions, the density is equally distributed with the width σ_r , we get the total distribution inside a single microtrap:

$$n_i(r, z) = \frac{N_i(r, z)}{N_i} = \frac{1}{\sqrt{8\pi}\sigma_z\sigma_r^2} e^{-\left(\frac{z}{2\sigma_z}\right)^2} e^{-\left(\frac{r}{\sigma_r}\right)^2} \quad (\text{D.3})$$

where $n_i(r, z)$ is the density inside a single microtrap with the total number of trapped atoms N_i , σ_r and σ_z are the width in radial and axial directions. The width σ_r and σ_z are given through

$$\sigma_r = \frac{w_0}{2} \sqrt{\frac{k_B T}{U_0}} \quad (\text{D.4})$$

$$\sigma_z = \frac{1}{\omega_z} \sqrt{\frac{k_B T}{M}} \quad (\text{D.5})$$

where w_0 is the waist of the forming laser beam, U_0 is the maximum trap depth, M the mass of Rb-atom and $\omega_z = 2\pi/\lambda \cdot \sqrt{U_0/M}$ the oscillation frequency along the axial direction.

The time evolution of the number of atoms in a single microtrap is described by the equation

$$\dot{N}_i = -\Gamma N_i - \beta \int n_i^2(r, z) dv \quad (\text{D.6})$$

where the decay due to the linear collisions (background gas collisions) is considered with the rate Γ . Decay rate β takes in account the density dependent two-body collision rate. Inserting Eq. refGaussFortAll into the Eq. D.6 and integrating over i we get:

$$\dot{N} = -\Gamma N - \beta \frac{\lambda}{32 \pi^2 \sigma_F \sigma_z \sigma_r^2} N^2 \quad (\text{D.7})$$

The solution for this differential equation is given by Eq. C.8 from the Appendix C. Thereby, parameters Γ , ξ , β and the maximal number of atoms in the trap N are connected together as follows:

$$\beta \frac{32 \pi^2 \sigma_F \sigma_z \sigma_r^2}{\lambda} N = \Gamma \frac{\xi}{1 - \xi} \quad (\text{D.8})$$

Using Eq. C.7, we can express β as:

$$\beta = \frac{\sqrt{8} \Gamma}{n_{max}} \frac{\xi}{1 - \xi} \quad (\text{D.9})$$

Comparing the Eqs. D.8 and D.9 we get for the maximum density n_{max} the following expression:

$$n_{max} = \frac{N \lambda}{\sqrt{8} \pi^2 \sigma_F \sigma_z \sigma_r^2} \quad (\text{D.10})$$

Using the Eq. D.4 we get the maximum density in the dipole trap, which is reached in the center of the most populated microtrap:

$$n_{max} = \frac{N \sqrt[3/2]{\frac{U_0}{k_B T}}}{\pi \sigma_F \omega_0^2} \quad (\text{D.11})$$

Parameter	Value	Units
Detuning δ	181.7	GHz
Waist w_0	249	μm
Trap depth U_0/k_B	173	μK
Temperature	70	μK
Heating rate	22.32	$\mu K/s$
$\eta = U_0/kT$	2.47	
Number of atoms N_0	5×10^6	
Density ρ_0	3×10^{11}	at/ cm^3
Lifetime τ	80	ms
Axial vibr. frequency ν_{ax} (calculated)	236	kHz
Radial vibr. frequency ν_{rad}	147.06	Hz
Radial vibr. frequency ν_{rad} (measured)	155.28	Hz
Time of compression t_{comp}	1.61	ms
Time of compression t_{comp} (measured)	1.7	ms

Table D.1: *Essential parameters of standing wave far-off-resonance dipole trap for ^{85}Rb*

Appendix E

Materials and Devices

E.1 Materials

Rubidium Ampoule 7440-17-7, Alfa GmbH/Karlsruhe

- natural isotope mixture 1 g

Micro Channel Plate (MCP), Type J5022-11/Hamamatsu GmbH/Hersching

- External size: 24,8 mm
- Effective size: 20 mm
- Channel diameter: 10 μm
- Thickness: 0,4 mm
- Open area ratio: 57
- Material: lead sulfate glass

Gaskets, Helicoflex[®], Garlock

- HN100-15027 M for 40 mm windows
- HN100-150443 M for 100 mm windows
- Material : Alu/Nimonic 90 (H)

Anamorphic Prism Pairs, Type PS871-B, Thorlabs GmbH/Karlsfeld

- unmounted, AR-coating 650-1050 nm.

Retardation wave plates (zero-order air spaced), LENS-Optics GmbH/Allershausen

- Air spaced $\lambda/2$, $\lambda/4$ retardation wave plates, Type: W2Z25 and W4Z25
- mounted, clear aperture 25mm, design wavelength 780nm
- all plates AR-coated (total reflection <0.15%)

E.2 Devices

Optical Table Newport RP RelianceTM, Newport/Darmstadt

- Sealed Hole Table Top, nonmagnetic steel

Ion Pump Star Cell VacIon Plus 20, Varian GmbH/Torino

- triode sputter-ion vacuum pump
- flange: DN 40 CF
- pumping speed (N_2): 20 l/s
- lifetime @ 10^{-6} mbar: 80000 h
- max. starting pressure: $1 \cdot 10^{-3}$ mbar
- final pressure: $< 10^{-11}$ mbar
- maximum backing temperature: 350 °C (for ferrite magnet)
- power supply: MiniVac controller (5000 V DC, 15 mA)/ Varian

Ion Pump PE 11 STD, Perkin Elmer

- diode sputter-ion vacuum pump
- flange: DN 40 CF
- pumping speed (N_2): 11 l/s
- maximum backing temperature: 150°C with magnet, 450 °C without magnet
- repaired pump by Duniway Corp. through Tectra GmbH/Frankfurt a.M.
- power supply: Ionpack 200 controller/ Perkin Elmer

Turbomolecular Pump Turbovac[®] 50, Leybold GmbH/Köln

- flanges: high vacuum side DN 40 CF, prevacuum DN 16 KF
- pumping speed (N_2): 29 l/s
- 72000 rpm, 2 min startup time
- max. starting foreline pressure: 1 mbar
- final pressure: $< 8 \cdot 10^{-9}$ mbar
- electronic frequency converter: TURBOTRONIC NT 10/Leybold

Foreline Pump Trivac[©] D 1,2E, Leybold GmbH/Köln

- flange: DN 16 KF
- pumping speed: $1.8 \text{ m}^3/h$
- 72000 rpm, 2 min startup time
- final pressure: $< 2 \cdot 10^{-3} \text{ mbar}$

Display and Control Unit Combivac IT 23, Leybold GmbH/Köln

- display range with TTR 211S transmitter: $5 \cdot 10^{-4}$ to 1000 mbar
- display range with Ionisation Vacuum Gauge ITR 100 transmitter: $2 \cdot 10^{-10}$ to $1 \cdot 10^{-1}$ mbar
- measurement range of TTR 211S transmitter: $5 \cdot 10^{-4}$ to 0.1 mbar
- measurement principle: thermal conductivity according to Pirani, tungsten filament

THERMOVAC TTR 211S Transmitter, Leybold GmbH/Köln

- flange: DN 16 KF
- measurement principle: thermal conductivity according to Pirani, tungsten filament
- measurement range of : $5 \cdot 10^{-4}$ to $1 \cdot 10^3$ mbar
- measurement uncertainty: $\pm 20\%$ in the range $5 \cdot 10^{-4}$ to $1 \cdot 10^3$ mbar

ITR 100 Transmitter, Leybold GmbH/Köln

- flange: DN 40 CF
- sensor type: wide range Bayard Alpert ionization vacuum gauge
- cathode: Yttrium oxide coated iridium dual cathode, protected by current limiting and overpressure emission cut-off
- measurement range of TTR 211S transmitter: $5 \cdot 10^{-4}$ to 0,1 mbar
- response threshold: $1 \cdot 10^{-10}$ mbar
- reproductivity: $\pm 10\%$ to the meas. value in the range $1 \cdot 10^{-7}$ to $1 \cdot 10^{-2}$ mbar

Temperature regulator TEMPAT[©], Messner Emtronic/Dettenhausen

- two point regulator, sensor break protected
- temperature range: 0-400 °C

- switchable power 2000W, 10 A
- sensor type: PT 100

Vacuum Leak Detector Ultratest UL 200, Leybold /Köln

- flange: DN 16 KF
- pumping speed (He): 1 l/s
- lower detection limit $5 \cdot 10^{-11}$ mbar
- upper detection limit $1 \cdot 10^{-1}$ mbar
- sensor type: PT 100

Photodiode Power Meter LaserMate-Q, Coherent /Dieburg

- silicon sensor VIS, wavelength range 400-1064 nm, power range 10 μ W to 50 mW, accuracy $\pm 3.5\%$ of reading, ± 2 LSD, max. 1.0 W/cm², sensor diam. 7.9 mm
- display response time <0.2 ms, offset of reading to zero

Thermal Power Meter MeterMate D10MM, Thorlabs GmbH/Karlsfeld

- wavelength range: 0.3-10.6 μ m
- accuracy $\pm 5\%$ of full scale, 10 mW resolution
- output "x100": 100 mV/W, 2x1000!: 1V/W
- sensor area 2.57 cm², aperture \emptyset 18.1 mm
- max. power 10 W, max. power density 200 W/cm²

Digital Oscilloscope LeCroy 9314C, LeCroy/USA

- -3 dB bandwidth: DC to 400 MHz @ 50 Ω , DC to 230 MHz @ 1M Ω
- four channels and digitisers, 50k acq.memory/channel
- output "x100": 100 mV/W, 2x1000!: 1V/W
- max. sampling rate 100 MS/s on each channel
- sensitivity 2 mV/div to 5 V/div, DC accuracy $\pm 2\%$ full scale
- 1 ns/div to 1000 s/div, clock accuracy $\leq \pm 0.002\%$

Signal Analyzer Advantest R4131D

- 10 kHz to 3.5 GHz, input 50 Ω
- labs. max. ratings +20 dBm and ± 25 VDC

Diode Laser for 780 nm Type HL7851G, Hitachi/Japan

- nominal output power 50 mW, negative polarity
- typical values: $I_{th}=40$ mA, $I_s=60$ μ A, $\nu=0.6$ mW/mA, $\lambda=782$ nm(@20°C) (for Rb D2 line), $\lambda=789$ nm (@20°C) (for Rb D1 line), $\Theta_{vert}=21^\circ$, $\Theta_{hor}=9^\circ$

Tapered Diode Laser for 780 nm Type SDL8630E,AMS Optotech/München, SDL/USA

- nominal output power 500 mW, negative polarity
- intra-cavity facet 4 μ m aperture AR coated (R=0.1%), output facet 130 μ m aperture
- serial number: TD 420, $I_{th}=0.52$ A, $I_{op}=1.55$ A, tuning range 781-791 nm, $\nu=0.4$ W/A, $\lambda=786$ nm(@21°C)

Diffraction Grating Type 263232 9051 324, Carl Zeiss Jena GmbH /Germany

- BK-7 substrate: 15x10x6 mm^3
- 1800 lines/mm, holographic sinus grating, reflecting coating: aluminium, reflecting efficiency in the first diffraction order: ca.25%

CCD camera, PixelFly, PCO Computer Optics GmbH/Kelheim

- b/w sensor Sony; Resolution: VGA, 640 x 480 pixel
- Pixel Size: 9.9x9.9 μm^2
- Dynamic Range: 12 bit
- Quantum Efficiency @ $\lambda=780nm$: 12%
- Expose Time: 10 μs \div 10s
- Readout Noise: 17 e^-
- Binning: vertical:1,2,4 ; horiz.: 1,2
- Optical Input: C-Mount
- Lenses: Pentax[©] Cosmicar 50mm/1.4

Fast Real-Time Automation System, ADWin-Gold, Jäger GmbH/ Lorsch

- CPU: SHARK-DSP 32 bit floating point, 512 kB DSP-RAM/ Analog Devices

- 16MB DRAM
- 16 analogue inputs: 2x16-bit $10\mu\text{s}$ ADCs and 2x12-bit $0.8\mu\text{s}$ ADCs
- 8 analogue outputs: 16-bits DACs $10/3\mu\text{s}$ ($<2\text{V}/20\text{V}$)
- 32 digital inputs/outputs, TTL/CMOS
- 1 trigger/event input, TTL/CMOS

Appendix F

Technical Data and Schemes

T(°C)	0	10	20	30	40	50	60	70	80	90	100
$\Delta U(\text{mV})$	0	0,40	0,80	1,21	1,63	2,05	2,48	2,91	3,35	3,80	4,25

Table F.1: *Thermoelectric voltages in mV according to DIN 43710 for Cu-Konst. thermocoupler (E.Braun). Comparative temperature is 0° C. In the experiments this temperature was set to 20° C, so one has to add to each position in the table the value 0,8 mV.*

Bibliography

- [1] C.S. Adams and E. Riis, *Laser cooling and trapping of neutral atoms*, Prog.Quant.Electr. **21** (1997), no. 1, 1–79.
- [2] A.M. Akulshin, S. Barreiro, and A. Lezama, *Electromagnetically induced absorption and transparency due to resonant two-field excitation of quasidegenerate levels in Rb vapor*, Phys.Rev.A. **57** (1998), no. 4, 2996–3002.
- [3] S.V. Andreev, V.I. Balykin, V.S. Letokhov, and V.G. Minogin, *Radiative slowing and reduction of the energy spread of a beam of sodium atoms to 1.5 k in an oppositely directed laser beam*, JETP.Lett. **34** (1981), 442–445.
- [4] E. Arimondo, *Progress in Optics*, p. 257, Elsevier, Amsterdam, 1996.
- [5] E. Arimondo and G. Orriols, *Nonabsorbing atomic coherence by coherent two-photon transitions in a tree-level optical pumping*, Lett.Nuovo Cimento **17** (1976), 333–338.
- [6] A. Aspect, E. Arimondo, R. Kaiser, N. Vansteenkiste, and C. Cohen-Tannoudji, *Laser cooling below the one-photon recoil energy by velocity-selective coherent population trapping*, Phys.Rev.Lett. **61** (1988), 826–829.
- [7] G. Azeita, A. Gozzini, L. Moi, and G. Orriols, *An experimental method for the observation of R.F. transitions and laser beat resonances in oriented Na vapour*, Nuovo Cimento B **36** (1976), 5–20.
- [8] G. Bendelli, S. Komori, and Y. Suematsu, *A new structure for high-power TW-SLA (travelling wave semiconductor laser amplifier)*, IEEE Photonics Technol.Lett. **3** (1991), no. 1, 42.
- [9] Eric D. Black, *An introduction to Pound-Drever-Hall laser frequency stabilization*, Am.J.Phys. **69** (2001), no. 1, 79–87.
- [10] D. Boiron, A. Michaud, P. Lemonde, Y. Castin, C. Salomon, S. Weyers, K. Szymaniec, L. Cagnat, and A. Clairon, *Laser cooling of cesium atoms in gray optical molasses down to 1,1 μ k*, Phys.Rev.A **53** (1996), no. 6, R3734–R3737.
- [11] Y. Castin, K. Berg-Sorensen, J. Dalibard, and K. Molmer, *Two-dimensional Sisyphus cooling*, Phys.Rev.A **50** (1994), no. 6, 5092–5115.

- [12] Y. Castin and J. Dalibard, *Quantization of atomic motion in optical molasses*, J.Europhys.Lett. **14** (1991), 761–765.
- [13] Y. Castin and K. Molmer, *Monte Carlo wave-function analysis of 3d optical molasses*, Phys.Rev.Lett. **74** (1995), no. 19, 3772–3775.
- [14] J. Chen, J.G. Story, J.J. Tollett, and R. Hulet, *Adiabatic cooling of atoms by an intense standing wave*, Phys.Rev.Lett. **69** (1992), no. 9, 1344–1347.
- [15] S. Chu, L. Hollberg, J. Bjorkholm, A. Cable, and A. Ashkin, *Three-dimensional viscous confinement and cooling of atoms by resonance radiation pressure*, Phys.Rev.Lett. **55** (1985), 48–51.
- [16] A. Corney, *Atomic and Laser Spectroscopy*, Oxford, Oxford University Press, 1977.
- [17] J.-Y. Courtois, *Thèse de Doctorat de l'école polytechnique*, Ph.D. thesis, Ecole Polytechnique, Palaiseau, 1993.
- [18] J.Y. Courtois and G. Grynberg, *Probe transmission in one-dimensional optical molasses: Theory for linearly cross-polarized cooling beams*, Phys.Rev.A **46** (1992), 7060–7078.
- [19] J.Y. Courtois and G. Grynberg, *Stimulated Rayleigh resonances and recoil effects*, Adv.At.Mol.Opt.Phys. **36** (1996), 88–140.
- [20] J. Dalibard and C. Cohen-Tannodji, *Laser cooling below the doppler limit by polarisation gradients: simple theoretical models*, J.Opt.Soc.Am.B **6** (1989), 2023–2045.
- [21] Wolfgang Demtröder, *Laserspektroskopie*, 3 ed., Springer, 1993.
- [22] Marshall T. DePue, Colin. McCormick, G.Lukmann Winoto, P.Steven. Oliver, and David. Weiss, *Unity occupation of sites in a 3D optical lattice*, Phys.Rev.Lett. **82** (1999), no. 11, 2262–2265.
- [23] R.H. Dicke, *The effect of collisins upon the Doppler width of spectral lines*, Phys.Rev. **89** (1953), no. 2, 472–475.
- [24] R.W.P. Drever, *Laser Phase and Frequency Stabilization using an Optical Resonator*, Appl.Phys.B: Photophys.Laser Chem.. **31** (1983), 97–105.
- [25] John Emsley, *The elements*, second ed., Clarendon press, 1991.
- [26] W. Ertmer, R. Blatt, J.L. Hall, and M. Zhu, *Laser manipulation of an atomic beam velocities: Demonstration of stopped atoms and velocity reversal*, Phys.Rev.Lett. **54** (1985), no. 10, 996–999.
- [27] C.W. Gardiner, J. Ye, H.C. Nagerl, and H.J. Kimble, *Evaluation of Heating Effects on Atoms Trapped in an Optical Trap*, Phys.Rev.A **61** (2000), 045801–1–045801–3.

- [28] M. Gatzke, G. Birkl, P.S. Jessen, A. Kastberg, S.L. Rolson, and W.D. Phillips, *Temperature and localization of atoms in three-dimensional optical lattices*, Phys.Rev.A **55** (1997), R3987–R3990.
- [29] S. Gensemer, V. Sanches-Villicana, K. Tan, T. Grove, and P. Gould, *Trap-loss collisions of ^{85}Rb and ^{87}Rb : Dependence on the trap parameters*, Phys.Rev.A **56** (1997), no. 5, 4055–4063.
- [30] J.P. Gordon and A. Ashkin, *Motion of atoms in a radiation trap*, Phys.Rev.A. **21** (1980), 1606–1617.
- [31] Rudolf Grimm, Mattias Weidemüller, and Yuri B. Ovchinnikov, *Optical Dipole Traps for Neutral Atoms*, Adv. at Mol. and Opt. Phys. **42** (2000), 1–39.
- [32] G. Grynberg and J.-Y. Courtois, *Proposal for a magneto-optical lattice for trapping atoms in nearly-dark states*, Europhys.Lett. **27** (1994), no. 1, 41–46.
- [33] G. Grynberg, B. Lounis, P. Verkerk, J.Y. Courtois, and C. Salomon, *Quantized motion of cold cesium atoms in two- and three-dimensional optical potentials*, Phys.Rev.Lett. **70** (1993), 2249–2252.
- [34] G. Grynberg and C. Triche, *Coherent and collective interactions of particles and radiation beams, proceedings of the International School of Physics "Enrico Fermi" 1995, course CXXXI*, ch. Atoms in optical lattices, pp. 243–284, North Holland, Amsterdam, 1996.
- [35] S.E. Hamann, D.L. Haycock, G. Klose, P.H. Pax, I.H. Deutsch, and P.S. Jessen, *Resolved-sideband raman cooling to the ground state of an optical lattice*, Phys.Rev.Lett. **80** (1998), no. 19, 4149–4152.
- [36] Dian-Jiun Han, Steffen Wolf, Steffen Oliver, Colin McCormick, Marshall T. DePue, and David. Weiss, *3D raman sideband cooling of cesium atoms at high density*, Phys.Rev.Lett. **85** (2000), no. 4, 724–727.
- [37] T.W. Hänsch and A.L. Schawlow, *Cooling of gases by laser radiation*, Opt.Comm. **13** (1975), 68–69.
- [38] A. Hemmerich, A. Görlitz, and T.W. Hänsch, *Ultracold atoms and Bose-Einstein Condensation, featuring papers from EQEC'96*, ch. Dark Optical Lattices, pp. 91–97, OSA, USA, 1996.
- [39] A. Hemmerich and T.W. Hänsch, *Two-dimensional atomic crystal bound by light*, Phys.Rev.Lett. **70** (1993), 410–413.
- [40] A. Hemmerich, M. Weidemüller, T. Esslinger, and T.W. Hänsch, *Collective atomic dynamics in a magneto-optical trap*, Europhys.Lett. **21** (1993), 445–449.
- [41] A. Hemmerich, M. Weidemüller, C. Zimmermann, T. Esslinger, and T.W. Hänsch, *Trapping atoms in a dark optical lattice*, Phys.Rev.Lett. **75** (1995), 37–40.

- [42] J. Jersblatt, H. Ellmann, and A. Kastberg, *Experimental investigation of the limit of Sisyphus cooling*, Phys.Rev.A **62** (2000), no. 5, 051401–1–051401–4.
- [43] P. Jessen, C. Gerz, P.D. Lett, W.D. Phillips, S.L. Rolson, Spreeuw R.J.C., and C.I. Westbrook, *Observation of quantized motion of rb atoms in an optical field*, Phys.Rev.Lett. **69** (1992), no. 1, 49–53.
- [44] A. Kastberg, W.D. Phillips, S.L. Rolson, and R.J.C. Spreeuw, *Adiabatic cooling of Cesium to 700 nK in an optical lattice*, Phys.Rev.Lett. **74** (1995), no. 9, 1542–1545.
- [45] W. Ketterle, B.D. Kendal, M.A. Joffe, A. Martin, and D.E. Pritchard, *High densities of cold atoms in a dark spontaneous-force optical trap*, Phys.Rev.Lett. **70** (1993), no. 15, 2253–2256.
- [46] Landolt-Börnstein, *Eigenschaften der Materie in ihren Aggregatzuständen, 2.Teil: Gleichgewichte ausser Schmelzgleichgewichten*, Clarendon Press, 1960.
- [47] R. Lang and K. Kobayashi, *External optical feedback effects on semiconductor injection laser properties*, IEEE J.Quantum Electron. **16** (1980), 347–355.
- [48] P.D. Lett, R.N. Watts, C.I. Westbrook, W.D. Phillips, P.L. Gould, and H.J. Metcalf, *Observation of atoms laser cooled below the Doppler limit*, Phys.Rev.Lett. **61** (1988), 169–172.
- [49] A. Lezama, S. Barreiro, and A.M. Akulshin, *Electromagnetically induced absorption*, Phys.Rev.A. **59** (1999), no. 6, 4732–4735.
- [50] D.R. Meacher, D. Boiron, H. Metcalf, C. Solomon, and G. Grynberg, *Method for velocimetry of cold atoms*, Phys.Rev.A **50** (1994), R1992–R1995.
- [51] H. Metcalf and P. van der Straten, *Laser cooling and trapping*, ch. 3, p. 32, Springer Verlag, 1999.
- [52] J.D. Miller, R.A. Cline, and D.J. Heinzen, *Photoassociation spectrum of ultracold sodium atoms*, Phys.Rev.Lett. **71** (1993), no. 14, 2204–2207.
- [53] C. Monroe, W. Swann, H. Robinson, and C. Wieman, *Very cold trapped atoms in a vapor cell*, Phys.Rev.Lett. **65** (1990), no. 13, 1571–1574.
- [54] B. Nagorny, *Dynamik kalter Atome in der Stehwelldipolfalle eines Ringresonators hoher Güte*, Ph.D. thesis, Institut für Laser-Physik, Universität Hamburg, Hamburg, 2003.
- [55] K.I. Petsas, J.-Y. Courtois, and G. Grynberg, *Temperature and magnetism of gray optical lattices*, Phys.Rev.A **53** (1996), no. 4, 2533–2538.
- [56] W.D. Phillips and H. Metcalf, *Laser deceleration of an atomic beam*, Phys.Rev.Lett. **48** (1982), no. 9, 596–599.

- [57] R. V. Pound, *Electronic Frequency Stabilization of Microwave Oscillators*, Rev.Sci.Instrum. **17** (1946), 490–505.
- [58] M. Prentiss, A. Cable, J.E. Bjorkholm, S. Chu, E.L. Raab, and D.E. Pritchard, *Atomic-density-dependent losses in an optical trap*, Phys.Rev.Lett. **13** (1988), no. 6, 452–455.
- [59] E.L. Raab, M. Prentis, A. Cable, S. Chu, and David.E. Pritchard, *Trapping of neutral sodium atoms with radiation pressure*, Phys.Rev.Lett. **59** (1987), no. 23, 2631–2634.
- [60] N.F. Ramsey, *Molecular Beams*, Clarendon Press, 1956.
- [61] Nils Rehbein, *Hochleistungs-Diodenlaser für die Quantenoptik auf der Basis von Injection-Locking bei 780 nm Wellenlänge*, Master's thesis, Institut für Laser-Physik, Universität Hamburg, 2001.
- [62] F. Renzoni, J.Opt.B.: Quantum Semiclass.Opt. **3** (2001), S7–S14.
- [63] L. Ricci, M. Weidemüller, T. Esslinger, A. Hemmerich, C. Zimmermann, V. Vuletic, W König, and T.W. Hänsch, *A compact grating-stabilized diode laser system for atomic physics*, Phys.Rev.A **117** (1995), 541–549.
- [64] C. Salomon, J. Dalibard, W.D. Phillips, A. Clairon, and S. Guellati, *Laser cooling of caesium atoms below 3 μ k*, Europhys.Lett. **12** (1990), 683–687.
- [65] T.A. Savard, K.M. O'Hara, and J.E. Thomas, *Laser noise induced heating in far-off-resonant optical traps*, Phys.Rev.A **56** (1997), R1095–R1098.
- [66] T. Sesko, D. Walker and C. Wieman, *Behavior of neutral atoms in a spontaneous force trap*, J.Opt.Soc.Am.B **8** (1991), 946–958.
- [67] B. Sheehy, S.Q. Shang, P. van der Staaten, S. Hatamian, and H. Metcalf, *Magnetic-field-induced laser cooling below the doppler limit*, Phys.Rev.Lett **64** (1990), 858–861.
- [68] I. Svartchuck, K. Dieckmann, M. Zielonkowski, and J.T.M. Walraven, *Broad area diode-laser system for a rubidium Bose-Einstein condensation experiment*, Appl.Phys.B **71** (2000), 475–480.
- [69] R. Taieb, P. Marte, R. Dum, and P. Zoller, *Spectrum of resonance fluorescence and cooling dynamics in quantized one-dimensional molasses: Effects of laser configuration*, Phys.Rev.A **47** (1993), 4986–4993.
- [70] H.R. Thorsheim, J. Weiner, and P.S. Julienne, *Laser-induced photoassociation of ultracold sodium atoms*, Phys.Rev.Lett. **58** (1987), no. 23, 2420–2423.
- [71] C.G. Townsend, N.H. Edwards, C.J. Cooper, K.P. Zetie, and C.J. Foot, *Phase space density in the magneto-optical trap*, Phys.Rev.A **52** (1995), no. 2, 1423–1440.

- [72] C. Triché, D. Boiron, S. Guibal, D.R. Meacher, P. Verkerk, and G. Grynberg, *Cesium atoms in grey optical lattices. study of temperature and capture efficiency.*, Opt.Comm. **126** (1996), 49–54.
- [73] M Vallet, M. Pinard, and G. Grynberg, *Two-wave mixing with cross-polarized beams in sodium: a quantitative investigation*, Opt.Comm. **87** (1992), 340–350.
- [74] D. Verkehrk, P.and Meacher, A.B. Coates, , J.Y. Courtois, S. Guibal, B. Lounis, C. Salomon, and G. Grynberg, *Designing optical lattices: an investigation with Cesium atoms*, Europhys.Lett. **26** (1994), 171–174.
- [75] P. Verkerk, B. Lounis, C. Salomon, C. Cohen-Tannoudji, J-Y. Cortois, and G. Grynberg, *Dynamics and spytial order of caesium atoms in a periodic optical potential*, Phys.Rev.Lett. **68** (1992), no. 26, 3861–3864.
- [76] V.S.Lethohov, *Narrowing of the Doppler width in a standing light wave*, JETP Letters **7** (1968), 272–275.
- [77] M. Weidemüller, *Lichtgebundene Atome: Phasenkonjugation, Bragg-Streuung und dunkle optische Gitter*, Ph.D. thesis, Ludwig-Maximilian Universität München, München, 1995.
- [78] Carl.E. Weiman and Leo. Hollberg, *Using diode lasers for atomic physics*, Rev.Sci.Instrum. **62** (1991), no. 1, 1–20.
- [79] J. Weiner, V. Bagnato, S. Zilio, and P. Julienne, *Experiments and theory in cold and ultracold collisions*, Rev.Mod.Phys. **71** (1997), no. 1, 1–85.
- [80] D. Weiss, E. Riis, Y. Chevy, P. Ungar, and S. Chu, *Optical molasses and multilevel atoms: experiment*, J.Opt.Soc.Am.B **6** (1989), 2072–2083.
- [81] M.T. Widmer, M.R. Doery, M.J. Bellanca, W.F. Buell, T.H. Bergemann, and H.J. Metcalf, *High velocity dark states in velocity-selective coherent population trapping*, Phys.Rev.A **53** (1996), 946–949.

Acknowledgement

During the realization of this project I was collaborating and getting help from many colleagues and friends, whom I would like to say thanks:

First, I would like to thank my supervisor Prof. Andreas Hemmerich who gave me the opportunity to work on the interesting topic of optical lattices. His profound knowledge about the physics of ultracold atoms and how to play with them was invaluable for the success of my work. His great experimental experience and active participation in the experiments in the lab, make a significant contribution to the project, as well as his extraordinary way of supervision.

With Jan Grünert I became not only a good neighbor for the office and lab, but a very good friend. I enjoyed the time spend with him in the helpful discussions concerning physical and technical problems as well as during the adventures outside the institute. His enthusiasm and optimism help me many times to overcome difficult phases of my work.

Thilo Elsässer and Boris Nagorny - the colleagues from the other "Rb-laboratory" I want to thank for the fruitful discussions on the trap physics. Dirk Hansen and Thilo Elsässer kindly agreed to proof-read my thesis and due to their advices I could significantly improved it.

All other former and current members of our research group: Gunnar Quehl, Adrien Schoof, Stephan Ritter, Nils Rehbein, Janis Mohr, Ciprian Căciu, Julian Klinner, and Malik Lindholdt I want to thank for the pleasant work environment.

On the beginning of my work I found an empty optical table and empty cupboards and shelves in the fresh renovated lab. In such situation, the success of the project is strongly depending on the good technical support. A lot of thanks to the people from the mechanical workshop for their reliable work. Rainer Knut made a lot of efforts to improve the construction and performance of the vacuum chamber. Monica Dengler, Horst Möller, Reinhold Kilian, and Frank Jonas realized in metal a lot of sophisticated constructions which I draw on paper.

For all problems with electronics I could count on the help and advice from Horst Biedermann, Rainhold Mielck and the rest of the electronic team.

Egon Paeth produced specially tailored dielectric coating which are indispensable for the experiment.

Finally, I thank my parents, my sister, who supported me with care, sympathy and education my whole life. Them and all my friends I want to thank for they never gave up hope that I will succeed one sunny day.